DELFT UNIVERSITY OF TECHNOLOGY

FACULTY OF 3ME

MASTER THESIS

Data-driven inverse design of growth-based Voronoi meta-materials

Author:
Sikko van 't Sant

September 26, 2022

Thesis committee
Dr. M.H.F. Sluiter
Dr. S. Kumar
Dr. J. Jovanova (MTT)
P. Thakolkaran

Graduation date
23-09-2022

Contents

Abstract

Metamaterials derive their properties from microstructure rather than from bulk material properties. This opens property spaces that are difficult, or impossible, to access with traditional methods. However, exploring this vast design space remains challenging because classical techniques can be computationally inefficient.
Recent years has seen many successful applications of data-driven methods to this problem. Data-driven models can be used to bypass expensive Finite Element (FE) simulations and experiments by exploiting large datasets. This requires the parameterization of microstructures such that they can be mapped to properties. The forward problem, in which properties of are determined from design parameters, is typically well-posed, which allows straightforward application of machine learning methods. The inverse problem, in which design parameters are identified to match specific properties, is ill-posed because multiple sets of design parameters can produce similar properties.
The Voronoi growth method induced by star-shape metrics provides a way to explore a large geometrical design space using simple parameterization. It is used to generate 2D unit cells of void and material pixels with non-trivial topologies. The growth process enforces connected geometry while also allowing for smooth transition between different designs. Using homogenization techniques, we generate a large dataset of design parameters and stiffness properties. Machine learning techniques are first used to model the forward problem. By combining the trained forward model with the inverse model, the inverse problem is rendered well-posed. Both the forward and (deterministic) inverse model show excellent agreement between target and predicted values. The method is generalized beyond the design space by targeting properties of non-growth based structures. We investigate methods to create a stochastic inverse model, that can produce multiple designs to match target properties. Verification is done by comparing tensile tests of 3D printed samples to FE simulations.

1 Introduction to metamaterials

The word "metamaterial" is derived from the Greek "meta" which roughly translates to "beyond" in English. The name implies a new type of material that goes beyond what we would normally expect to find in nature. This can be an accurate description in cases where exotic properties are realised, like materials with negative Poisson's ratio [1]. But in several applications metamaterials are used to emulate or replicate natural structures, one example being bone implants [2]. Either way, the shared characteristic amongst all these approaches is that metamaterials are designed in such a way that their properties are derived from periodic or non-periodic microstructures and constituent material properties. Hence, another (perhaps more descriptive) name for metamaterials is architected materials [3]. This class of materials offers the possibility to make more optimized large scale designs by fine tuning material properties to anticipated load cases. However, development of the field of metamaterials did not start with mechanics but with electromagnetism [4, 5]. The name "metamaterials" was introduced only about twenty years ago[4] but the origins of the field can be traced back much further in time. Some consider Jagadish Chandra Bose's work on artificial chiral media from 1898 to be the first work done in this field[6, 7]. Others suggest a more recent date of 1967, when Veselago[8] discussed the possibility of materials with both negative permittivity and negative refractive index[4, 5, 9]. Regardless, it was not until 2000 that Smith et al.[10] fabricated a functional metamaterial, with properties as theorised by Veselago, and managed to develop a method to quantify these properties. This work inspired many other researchers and marked the beginning of a new era of research in metamaterials. Initially, development was focused mainly on electromagnetic properties[4, 11] but interest soon spread to acoustics [12, 13] and later to mechanical properties[14, 15, 16].

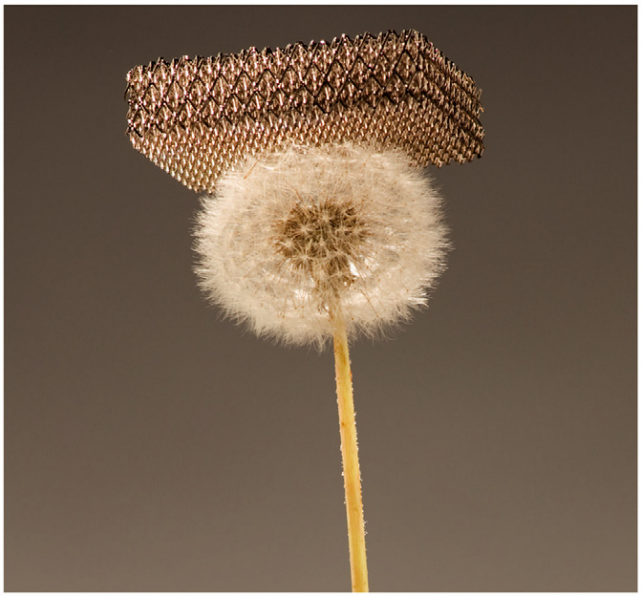

Figure 1.1: An example from 2011 of an ultralight metamaterial based on a hollow nickel periodic microstructure[16], image adapted from ref.[15].

1.1 History of metamaterials

The propagation of light through a medium can be described by the Maxwell equations[17]. They are derived from the observation that light is a combination of electric and magnetic waves that interact with each other. The set of equations that completely describe the propagation of light waves are rather complicated and it is not necessary to dive into their details for the treatment of optical metamaterials. However, it is important to understand that from the Maxwell equations, two fundamental constants are derived that determine how light travels and interacts with different materials.[8] These are the permittivity ϵ and magnetic permeability μ and they determine how light travels through various materials and what happens at the interface where two different materials meet. To gain more insight in this we can consider the refractive index of a material, which is calculated according to [8, 18]

$$n^2 = \epsilon\mu. \tag{1.1}$$

Among other things, the refractive index determines how a light beam interacts with different media. Another way of thinking about the refractive index is by considering it to be the "optical density" of a material. In this approach,

the refractive index is a measure for how much light is slowed down by travelling through a medium compared to traveling through a vacuum [18]. The refractive index then relates the speed of light in vacuum (c) to the speed of light in a medium (v) according to:

$$n = \frac{c}{v}. \tag{1.2}$$

The difference in refractive index determines the angle of refraction at the interface of two different homogeneous materials according to Snell's law [19]

$$\frac{n_i}{n_r} = \frac{sin\theta_i}{sin\theta_r}. \tag{1.3}$$

Where n_i, n_r and θ_i, θ_r represent the index and angle of refraction for incident (i) and refracted (r) beam. This is demonstrated schematically in figure 1.2a. Optical materials generally have positive ϵ and μ and from 1.2 it follows that this leads to refractive indices that are also positive. Under this assumption, the difference in refractive index is a measure for how much an incident light is bend towards the interface normal. A high difference in refractive index means the bending of the beam will be larger. In 1976 Veselago [8] demonstrated that it would theoretically be possible to have materials with negative ϵ and μ. It was demonstrated that this would result in reverse behaviour of electromagnetic properties like refraction and Doppler shift. In theory, it would be possible to have materials with a negative index of refraction. This would lead to materials in which an incident beam would "reflect" from the incident normal plane instead of bending towards or away from it, as demonstrated in figure 1.2b. Please note that the use here of the term "reflect" does not imply a physical reflection like in a mirror, it only refers to a geometrical interpretation of the path of the beam.

(a) Positive n_i and n_r.

(b) Positive n_i and negative n_r.

Figure 1.2: Schematic representation of the index of refraction and relevant angles at an interface for light travelling from point P to point Q through O, image adapted from ref.[19].

Moreover, Veselago showed that a flat sample of such a material would exhibit similar behaviour as a curved lens, as can be seen from the figure from his original paper, reproduced in figure 1.3.

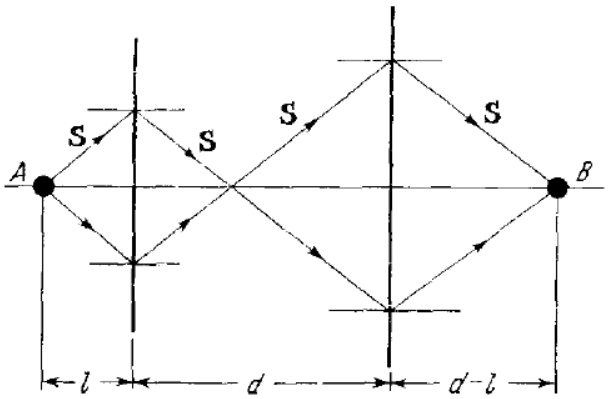

Figure 1.3: Image from Veselango's original paper demonstrating how a flat sample (with thickness d) of material with negative index of refraction can act as a lense for light traveling from A to B, image adapted from ref.[8].

The 1967 paper also introduced the terms right-handed and left-handed substances to differentiate between the two types of materials. To understand this, we need to consider the physics behind the Maxwell equations. Without going into too much detail, lets consider a monochromatic light wave that consists of an oscillating electric field interacting with a perpendicular magnetic field, as depicted in figure 1.4a. If the direction in which both fields oscillate is known, the propagation direction of the wave can be determined from the right-hand rule. By pointing the thumb in the direction of the electric field (E) and the index finger to the magnetic field (B) the direction of propagation is found in the direction of the middle finger, as demonstrated in figure 1.4 [8, 20, 21]. Veselago demonstrated that this is universally true for a monochromatic beam in materials with positive ϵ and μ. Additionally, this paper demonstrated that the left-handed rule (the same approach but using the left hand) would apply to materials with negative ϵ and μ, and that this would lead to the behaviour as demonstrated in figure 1.2b. These terms are still in use today and authors often refer to optical metamaterials as left-handed materials.

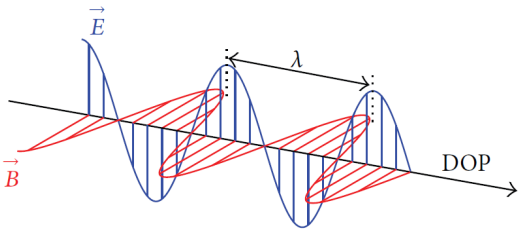

(a) Schematic representation of a light wave demonstrating the perpendicular magnetic (B) and electric (E) fields, figure adapted from [22].

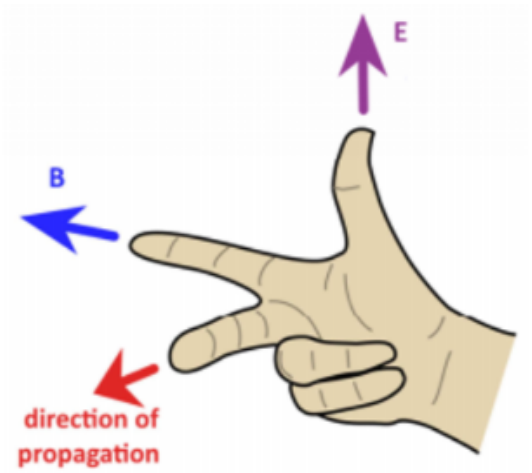

(b) Using the right-hand rule to determine the direction of propagation of a monochromatic light wave in materials with positive ϵ and μ, image adapted from ref.[20].

Figure 1.4: The right-hand rule for electromagnetic waves.

In nature no materials have yet been found that exhibit both negative permeability and permittivity, therefor novel approaches must be taken to achieve these exotic properties. This is achieved by not relying on macroscale material properties to govern optical response, instead microscale designs are used to manipulate macroscale behaviour. For this approach to work, it is important to keep het microscale dimensions within a range that corresponds to the desired wavelength. In 1999, Pendry et al.[23] introduced the following design parameter for optical metamaterials:

$$a << \lambda = 2\pi c_0 \omega^{-1} \tag{1.4}$$

where a represents the characteristic unit cell length, λ the wavelength, c_0 the speed of light in vacuum, and ω the frequency. They key concept of this approach is that the microsctructures are small relative to the wavelength and can be considered homogeneous on a macroscale level. This work was followed up in 2000 by Smith et al.[24] with a paper that proposed a unit cell design based on a copper split rings to achieve a material with both negative permeability and permittivity. The rings interact with an incident magnetic field and can either enhance or oppose the them, depending on the frequency. The ring dimensions can be adjusted to tune to specific frequencies. The design and experimental results of a ring with specified dimensions is shown in figure 1.5.

It was demonstrated that these structures would indeed have negative ϵ and μ but their values were not quantified. Later that year, Smith et al.[10] published another paper in which they successfully applied a Finite Element (FE) approach to calculate those values. With these results, theory about the behaviour of left handed materials and a method for quantifying the key parameters were available. This provided scientists with tools to engineer for specific values of ϵ and μ which paved the way for the development of novel applications. The theory was further expanded upon in 2008 by Landy et al.[25] in a paper that demonstrated how to design materials with near perfect absorption at a specific frequency. To achieve this, the magnetic and electric resonance should be manipulated independently to achieve high absorption of both parts of the electromagnetic beam. Additionally, the impedance of the material should match that of the environment to reduce reflectivity. Figure 1.6 shows numerical results of a design based on this approach and it shows near perfect reflectance and absorbance at 11.6 GHz.

Both 1.5 and 1.6 show that high absorption only occurs over a narrow frequency range and this is a direct result of the geometry dependent properties of the unit cells. To improve operating bandwidth, attempts have been made to

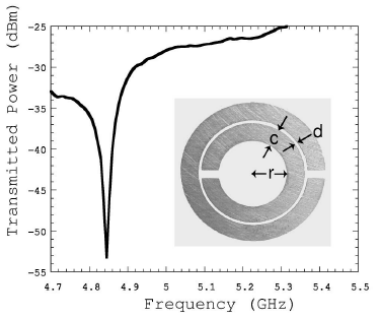

Figure 1.5: A single unit cell and experimental resonance curve of the structure as proposed by Smith et al. in 2000, with $c = 0.8mm$, $d = 0.2mm$ and $r = 1.5mm$, image adapted from ref.[24]

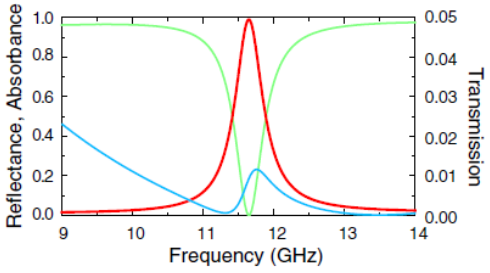

Figure 1.6: Simulated frequency response of a cell designed according to principles proposed by Landy et al.. The green line shows reflection, red shows absorption and blue shows transmission, image adapted from [25].

combine geometries optimized for several frequencies into a single flat unit cell design [26]. This has led to designs with multiple absorption peaks [27]. However, the number of frequencies that can be included in a single design is limited because of the direct relationship between geometry and function. An alternative approach has been to stack layers with different peak absorption on top of each other and this has produced materials with a broad absorption range [28]. An example of such an approach is depicted in 1.7 where the design (a) and simulated results (b) are shown. The simulations show that the broad operating bandwidth is a result of multiple overlapping peaks, rather than the broadening of a single peak. Although stacking layers could provide an avenue for large broadband, high absorption materials, it does introduce challenges for manufacturing and possible recycling. Additionally, thicker layers also add weight to structures and for aerospace applications that might prove to be problematic. Another challenge that scientists face are the directional dependency of the designs [26]. Most of the designs that have been discussed perform well only under specific angles of incident light beams. Although improvements have been made by creating more symmetric unit cells, it remains a topic of ongoing research[29].

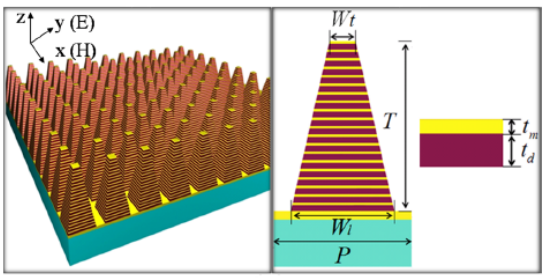

(a) Design of a single the unit cell (right) and grid (left).

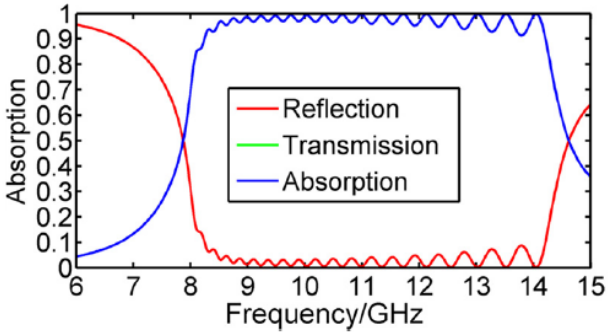

(b) Simulated reflection and absorption behaviour of the design shown in (a).

Figure 1.7: Design and FE simulation results for a pyramidal unit cell design by Ding et al., images adapted from [28].

1.2 Theory of mechanical metamaterials

1.2.1 Elasticity tensor

Mechanical metamaterials generally refers to designs that aim to achieve specific mechanical properties, like specific Young's moduli or Poisson's ratios[30]. As with any other type of metamaterial, this is achieved by manipulating their microstructure. In any material, the linear elastic stress strain response can be described by a symmetric fourth order elasticity tensor, according to[31, 32]

$$\boldsymbol{\sigma} = \mathbb{C}\boldsymbol{\epsilon}. \tag{1.5}$$

Where $\boldsymbol{\sigma}$ and $\boldsymbol{\epsilon}$ represent the 3x3 stress and strain tensors, respectively, and $\mathbb{C}$ represents the elasticity tensor. The components of the stress and strain tensors are schematically shown in figure 1.8.

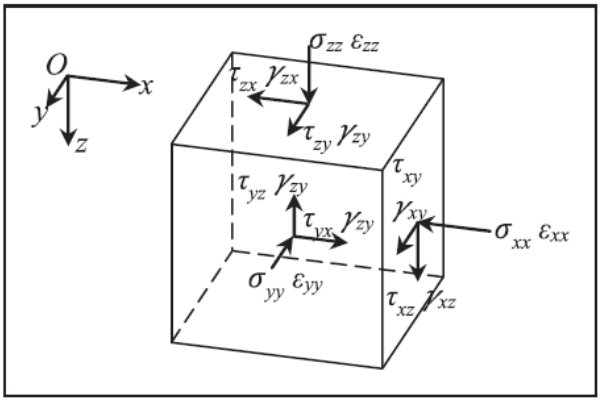

Figure 1.8: Schematic representation of the nine components of the stress and stain tensors, image adapted from ref.[32].

If the material is isotropic, stress and strain are related by just two independent constants, Young's modulus (E) and Poisson's ratio (v). For more complicated cases the elasticity tensor will have more independent components. However, due to symmetry constraints the maximum number of independent components is 21 and the elasticity tensor has to be positive definite[31]. In natural materials, it is typically defined by geometry and material properties and as such provides a very limited design space. However, in 1995 Milton and Cherkaev[33] demonstrated that in principle any $\mathbb{C}$ can be achieved that satisfies the symmetry constraints, as long as the laws of thermodynamics are obeyed. Although it was noted that fabrication of these materials could be problematic, it did open up the possibility of theoretically designing materials with mechanical properties not normally found in nature. An overview of the various methods through which this can be achieved is provided in table 1.1. These methods will be discussed in more detail in Chapter 3.

Table 1.1: Overview of different methods that can be used for the design of metamaterials[31].

Method	**Principle**
Truss based	Fundamental building blocks are rigid elements and flexible hinges.
Origami and Kirigami based	Properties come from introducing folds and/or cuts to sheet material.
Foam based	Fundamental building blocks are geometric designs in flexible material.

1.2.2 Theoretical limits

In order to explore the design space offered by metamaterials, attempts have been made to define the theoretical limits of material properties, like the elastic modulus. One of the earliest works on this topic was published in 1889 by W. Voigt [34]. In this paper, the behaviour of a composite material was analysed under the assumption that the strain across the material is uniform when loaded. Ignoring Poisson effects, this lead to an expression of the elastic modulus (E) for a composite made of materials A and B of

$$E_{Voigt} = \phi_A E_A + \phi_B E_B, \tag{1.6}$$

where E_A and E_B are the elastic moduli, and ϕ_A and ϕ_B the volume fractions, of phase A and B[35]. In an alternative approach, proposed in a paper by A. Reuss from 1929 [36], stress (instead of strain) was considered to

be uniform across a composite material. By also ignoring Poisson effects, an expression was found that lead to a lower estimate of the effective elastic modulus according to

$$\frac{1}{E_{Reuss}} = \frac{\phi_A}{E_A} + \frac{\phi_B}{E_B}. \tag{1.7}$$

The two approaches give different estimations of the effective modulus and in 1952 R. Hill [37] demonstrated that the actual effective modulus of a composite material will always have a value that lies between the two estimates. The upper bound is then given by the Voigt approximation and the lower bound by Reuss. The Voigt upper bound is still frequently used to check the validity of a calculated result or to determine whether a material property is feasible. These early works helped to establish domain bounds for feasible material properties although they could be far apart [38]. Therefor, the two models are sometimes combined into a hybrid formulation through a weight factor (α) according to

$$E_{RV} = \alpha E_{Voigt} + (1 - \alpha E_{Reuss}), \tag{1.8}$$

which is referred to as the Reuss-Voigt (RV) approach [39, 40]. Another often used bound was proposed by A. Hashin and S. Shtrikman in 1963 in a paper where they applied a variational approach to elastostatics for multiphase isotropic multiphase media [41]. The result was a theory that provided tighter upper and lower bounds on elastic and shear modulus of a composite material, based only on information of constituent material properties and volume fractions. These bounds are often referred to as the Hashin-Shtrikman (HS) bounds but their formulations for a multiphase material are extensive and will not be included here. However, when applied to a porous material all of the expressions above are simplified because it reduces one of the elastic moduli to 0. In a study on topology optimization by by M.P. Bendsøe and O. Sigmund, [40] the following relationships between the elastic modulus of a base material (E_s) and relative density ($\overline{\rho}$) of a porous material were found:

$$E_{Voigt} = \overline{\rho} E_s, \tag{1.9a}$$

$$E_{Reuss} = 0, \tag{1.9b}$$

$$E_{HS} = \frac{\overline{\rho} E_s}{3 - 2\overline{\rho}}, \tag{1.9c}$$

$$E_{RV} = \begin{cases} \alpha \overline{\rho} E_s & \text{if} \quad \overline{\rho} < 1 \\ E_s & \text{if} \quad \overline{\rho} = 1 \end{cases} \tag{1.9d}$$

In the formulation of 1.9d, the modulus of the porous structure is set to be equal to that of the solid in the case that $\overline{\rho} = 1$ because it implies that there is no porosity. Figure 1.9 shows a plot of the Voigt and HS upper bounds for a material with a Young's modulus of 1. Additionally, it shows an RV approximation using a value of of $\alpha = 1/3$ as it was found that this is the largest allowed value that doesn't violate the HS upper bound. The graph demonstrates the tighter upper bound that is defined by the HS method compared to the Voigt method.

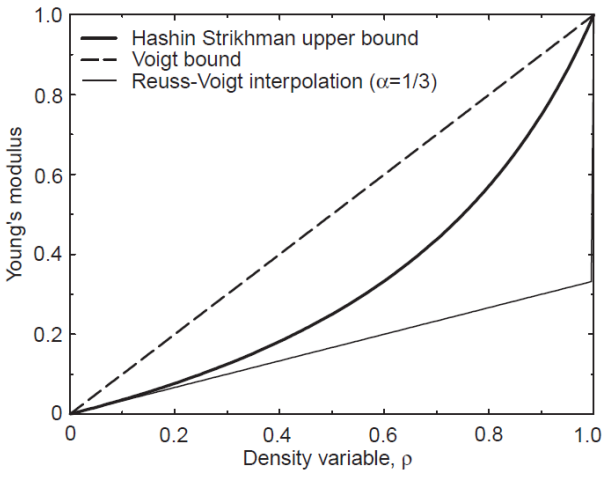

Figure 1.9: Plot of the Voigt, Hashin-Shtrikman and Reuss-Voigt upper bounds for a Young's modulus of 1 for the constituent material, image adapted from ref. [40].

1.2.3 Bending vs stretching dominated structures

Bending or stretching

Other authors took a different approach to produce models that predict properties of materials based on their architecture. This lead to the formulation of two distinct structure types: bending dominated and stretching dominated [42, 43]. The key difference between the two is their collapse mechanism. Bending dominated structures fail primarily because of macroscale strain whereas stretching dominated structures fail due to local mechanisms, like buckling. Examples of common architectures of both types are shown in figure 1.10, where (a) and (c) are stretching dominated structures and (b) a bending dominated structure.

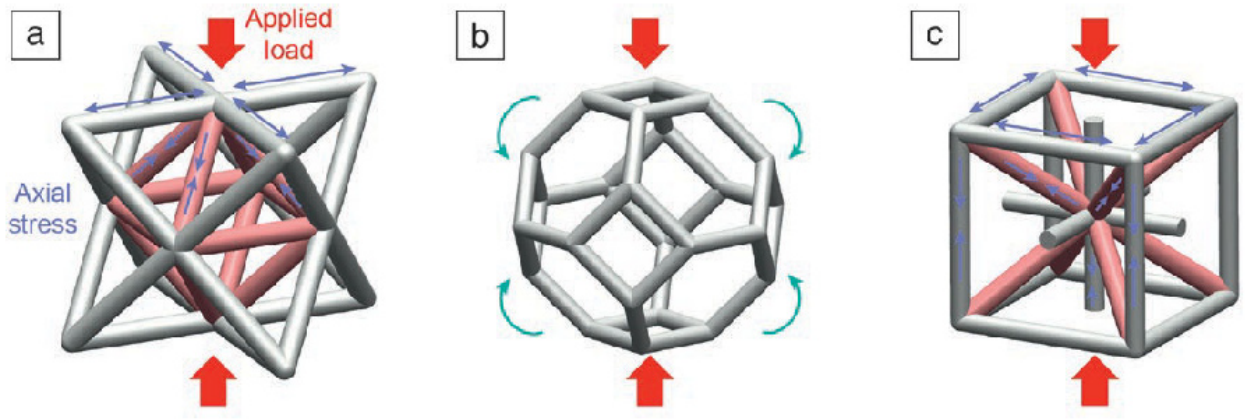

Figure 1.10: Examples of common unit cells of truss based lattices . (a) Octet-truss; (b) tetrakaidecahedron and (c) iso-truss. The red arrows indicate the applied load and the blue arrows indicate the deformation mode. Beams in red carry compressive loads and are most likely to fail first due to buckling if the constituent material is a metal. Image adapted from ref. [44].

Bending dominated structures under compressive loads tend to deform relatively easily with good recoverability. Their properties are largely determined by the strength of the joints and rotational stiffness of the struts, which makes them sensitive to fabrication errors and imperfections [45]. In stretching dominated structures, the struts carry compressive or tensile loads and strength is determined by the stiffness of the trusses. They generally have high specific properties but tend to show anisotropic behaviour [46]. Rigidity is a term often used in this context and it relates to the degree to which a structure exhibits bending or stretching dominated behaviour, with more rigid structures showing more stretching dominated behaviour [42].

Power law theory

In a paper from 2010 by Fleck et al. [47], the authors describe a theoretical framework to predict properties of metamaterials based on geometry. Following arguments from the analysis of pin-jointed frames, it was demonstrated that in theory, the structure type can be identified by considering only their nodal connectivity [48]. Subsequently, expressions for elastic modulus and yield strength were derived by applying beam theory. The relative density ($\overline{\rho}$) of a structure is defined as the ratio between the density of a solid and a structure with the same dimensions. For sufficiently small $\overline{\rho}$ (lower than 0.2) it can be calculated according to

$$\overline{\rho} = A\frac{t}{l}, \tag{1.10}$$

where t and l are the thickness and length of one truss and A a proportionality constant based on geometry. It was found that both elastic modulus (E) and yield strength (σ_y) scale with relative density ($\overline{\rho}$) through a power law according to

$$E = BE_s\overline{\rho}^{\beta}, \tag{1.11}$$

$$\sigma_y = C\sigma_{ys}\overline{\rho}^{\gamma}. \tag{1.12}$$

In these equations, B and C are proportionality constants related to geometry and E_s and σ_{ys} are the elastic modulus and yield strength of the solid material. The scaling constants β and γ are determined by whether a structure is bending or stretching dominated [49]. In bending dominated structures $\beta \approx 2$ and $\gamma \approx 1.5$ while in stretching dominated structures scaling is roughly linear with $\beta \approx 1$ and $\gamma \approx 1$.

1.2.4 Auxetic materials

One class of metamaterials that has received considerable attention is that of auxetic materials. These are materials with negative Poisson's ratio, meaning they contract laterally when compressed and expand when stretched. Even though the idea of materials with negative Poisson's ratio goes back almost two centuries[6, 7], the term "auxetic" was only introduced in 1991 by K.E. Evans [50]. Coming from the greek word "auxetos", meaning "that may be increased", it was proposed as a better alternative to "materials with negative Poisson's ratio". The Poisson's ratio ν is defined as

$$\nu = -\frac{\varepsilon_{lateral}}{\varepsilon_{load}}, \tag{1.13}$$

where $\varepsilon_{lateral}$ and ε_{load} are the strains in lateral and loading direction, respectively [51]. It is named after the Frenchman Poisson, who in 1827 proposed a universal value of ν = 1/4 following arguments based on molecular dynamics [52]. However, later research demonstrated that it is not a constant but can vary from material to material [53]. Natural materials tend to have values of ν between 0 and 0.5, see figure 1.11.

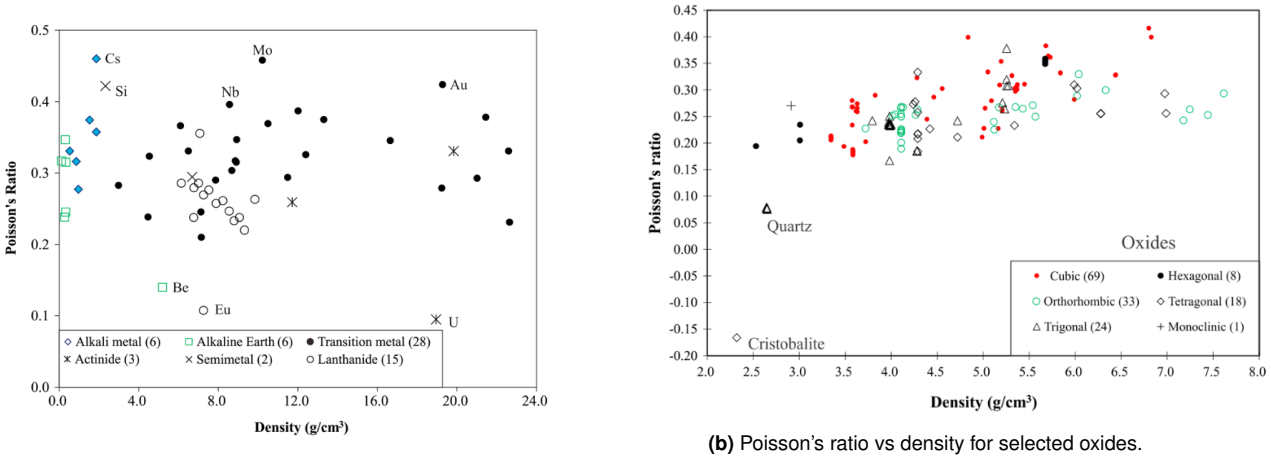

(a) Poisson's ratio vs density for selected natural elements.

(b) Poisson's ratio vs density for selected oxides.

Figure 1.11: An overview of the Poisson's ratio for various materials, nearly all of them have a ratio between 0 and 0.5, images adapted from [53].

However, in 1965 Y.C. Fung demonstrated that according to constitutive material laws, ν could theoretically take any value between -1 and 0.5 [54]. It was realised that materials with negative Poisson's ratio would exhibit unconventional material behaviour and that they would expand when stretched, as visualised in figure 1.12.

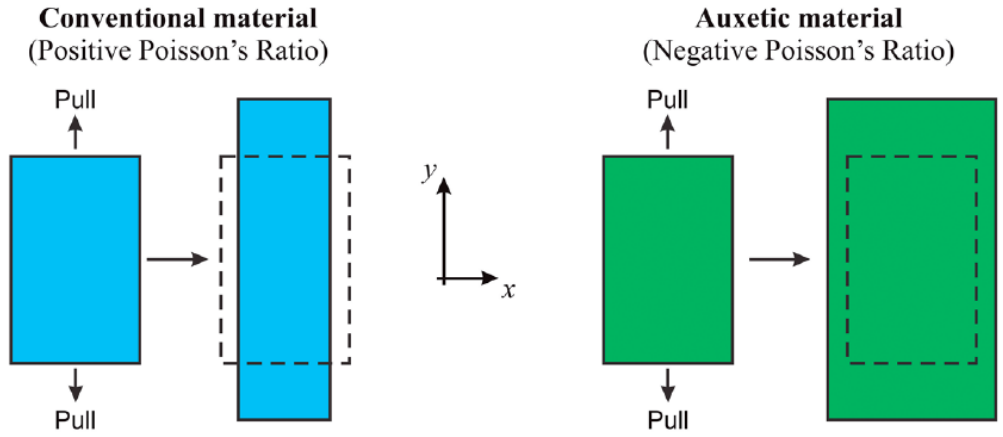

Figure 1.12: Comparison between convential material (positive Poisson's ratio) and auxetic material (negative Poisson's ratio), image adapted from ref. [53].

Additionally, some specific values for ν would correspond to special behaviour, an overview of which is provided in table 1.2. For example, under conditions of incompressibility the Poisson's ratio will be equal to 0.5 [51].

Table 1.2: An overview of specific values for ν and their physical significance for isotropic solids, adapted from ref. [51].

Poisson's ratio	Physical significance
ν = 0.5	Preservation of volume
ν = 0	Preservation of cross section
ν = -0.5	Preservation of moduli (E=G)
ν = -1	Preservation of shape

1.2.5 Heterogeneous metamaterials

Homogeneous metamaterials have a periodic microstructure of repeating unit cells. Heterogeneous materials consist of spatially varying microstructures and have been the subject of interest due to their potential for allowing more optimal designs[55]. These type of microstructures are found in many places in nature, like human tissue and bones [56, 57, 58]. The design process of heterogeneous metamaterial requires topology optimization, which means the search of the optimal distribution of material within a design domain [59]. This is schematically illustrated in figure 1.13.

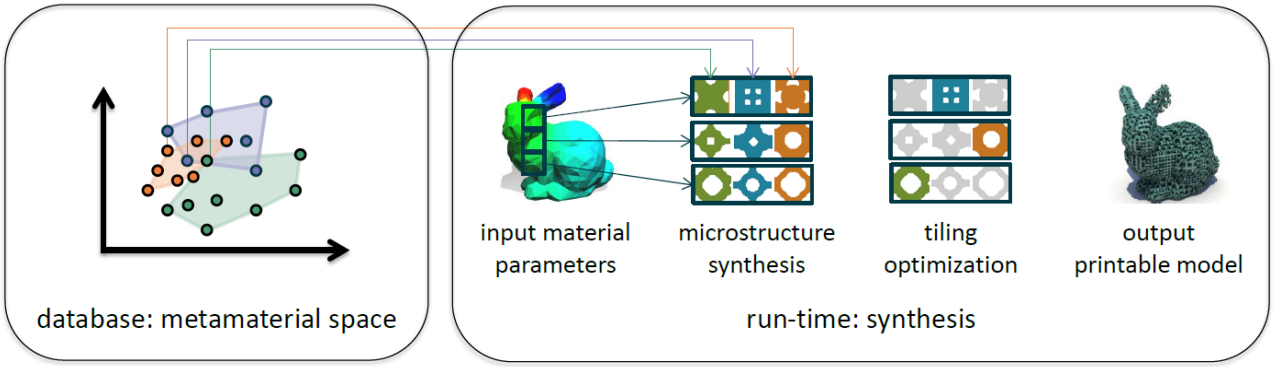

Figure 1.13: Design of a 3D printable heterogeneous model based on tiling of different microstructures using a database of metamaterial properties. Image adapted from ref. [60].

This leads to a two scale optimization problem, with simultaneous optimization of both the macroscale and microscale design [59].

SIMP and homogenization

Finding optimal local topology is usually done by dividing the domain in discrete unit cells and find their optimal material distribution. Properties of metamaterial unit cells can be highly non-linear and depend more on their design than their constituent materials, thus finding an optimal design can be challenging [55]. Another challenge is the computational cost of FE models with large scale microstructural heterogeneity [60, 61]. To solve this problem, the Solid Isotropic Materials with Penalization (SIMP) method is often used [59, 62]. In this method, the density is varied locally using a continuous variable between 0 and 1 (0 meaning void and 1 meaning solid) while penalizing any value between 0 and 1, to obtain a binary design [59]. Another popular method is that of homogenization, which requires calculating the effective properties of various unit cells. Typically, the effective macroscopic properties of a microstructure are determined and used to represent the microstructure in terms of a continuum Representative Volume Element (RVE) [61, 63]. In the case of mechanical response, this means finding an effective elasticity tensor ($\boldsymbol{IE}^*$) over a domain (Ω). This can be determined from the relationship between average stress ($\langle\sigma\rangle$) and strain ($\langle\epsilon\rangle$) according to:

$$\langle\sigma\rangle_\Omega = \boldsymbol{IE}^* : \langle\epsilon\rangle_\Omega. \tag{1.14}$$

Having determined the effective elasticity tensor, FE calculations can now make use of these homogenised properties as if the material were a continuum, as illustrated in figure 1.14.

Using homogenized RVEs means a mesh is no longer required to be fine enough to be able to adequately capture microstructural details, leading to significant performance improvement of large scale FE models. Additionally, optimization problems for heterogeneous designs can be designed to minimize the difference between effective properties and target values. This approach is commonly referred to as inverse homogenization [64, 65]. Figure 1.13

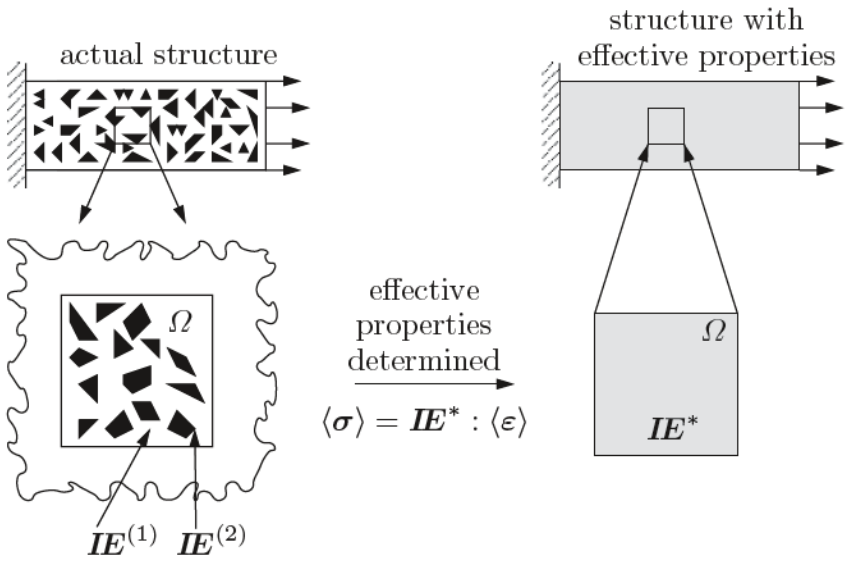

Figure 1.14: An actual structure with microscale heterogeneities is homogenised by determining effective properties of a RVE. Image adapted from ref. [63].

can be seen as an example of this method and it also demonstrates one of its major challenges: cell connectivity [60, 64, 66]. In order to make functional heterogeneous designs, it is necessary that neighbouring cells connect.

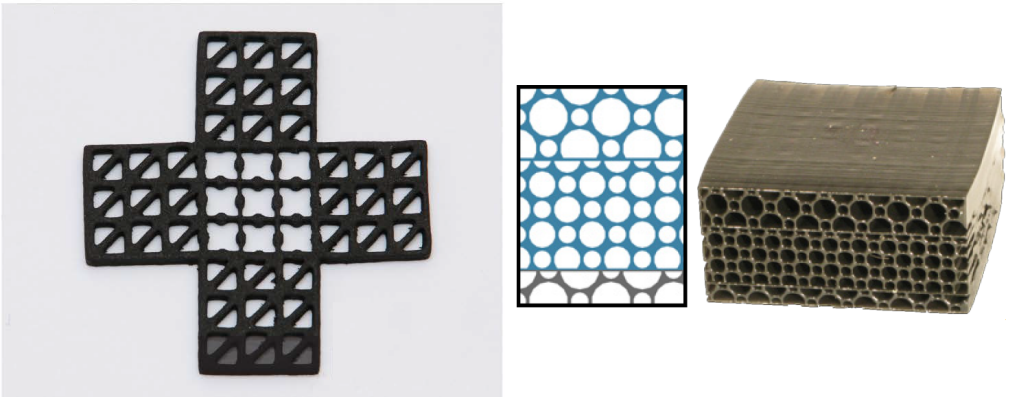

Figure 1.15: Two examples of heterogeneous structures where interconnectivity between unit cells is guaranteed by closed boundaries. Images adapted from (left) ref. [67] and (right) [68].

In the work by Schumacher et al. [60] (figure 1.13) this was achieved by building a database of many different topological families which partially overlap in property space. To obtain the final microstructure, the algorithm first determined which designs could meet the desired properties, and subsequently selected the microstructures that have the best connectivity. An alternative approach is to enforce closed boundaries on each unit cell to guarantee connectivity [67, 68, 69], two examples of which are shown in figure 1.15. A downside of these methods is that even though inter-connectivity is achieved, it does not lead to efficient load transfer from one cell to another [60].

Functionally graded materials

To address the issues mentioned in the previous paragraph, scientists have considered using Functionally Graded Materials (FGM) to produced heterogeneous metamaterials [2, 64, 66, 70, 71]. FGM have gradient properties due to gradual changes in composition or microstructure, instead of step-like changes from cell to cell, like in figure 1.15. This is similar to natural designs and it guarantees that neighbouring cells are connected and have similar topology. The concept was introduced in 1980s for heat shields in space applications [72] but in recent years it has also been applied to metamaterials [64]. To implement this numerically, additional constraints need to be applied to the optimization problem. In a 2008 paper by Zhou et al. [64], three methods were proposed to enforce

connectivity and topological similarity of neighbouring cells. Two methods, kinematic connective constraint (KC) and Pseudo load (PL) were based on optimizing local microstructures while enforcing connectivity constraints, the other method, unified formulation (UF), optimized the microstructure over the whole domain. The KC method introduces connectivity by enforcing the presence of material at matching regions in adjacent cells, see figure 1.16a. Although this did lead to connected cells, it does not guarantee an optimal outcome because of the restrictions put on the boundary domains [70]. The PL method made use of the observation that connectivity leads to stiffness across the domain. By introducing a pseudo load with kinematic boundary conditions, a stiffness criterion could be included in the optimization problem, figure 1.16b.

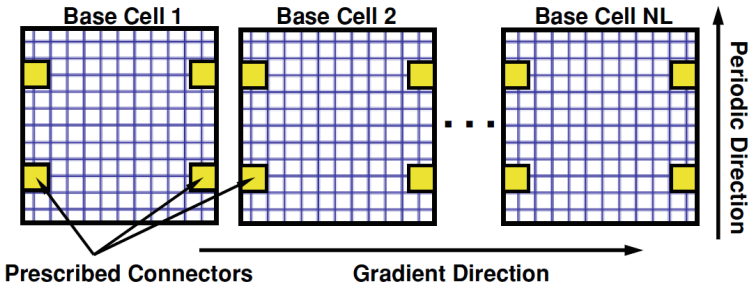

(a) Kinematic connective constraints with enforced connectors between cells.

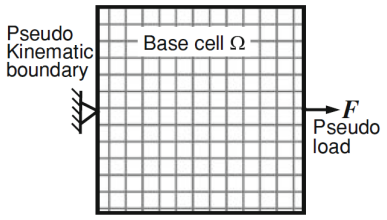

(b) Pseudo load and boundary condition used to introduce a stiffness criterion.

Figure 1.16: Schematic representation of the KC and PL methods as proposed by Zhou et al., image adapted from ref. [64].

Lastly, the UF method applied an optimization procedure over the whole domain. To ensure connectivity the authors considered the density gradient to be a useful measure because a high gradient would indicate poorly connected topology. Thus, by minimizing the norm of the density gradient, connectivity could be promoted. This method proved to be the most successful, but the large scale optimization meant the procedure was computationally more expensive than the other methods. There have been made improvements to this approach to speed up computation times in later research [73]. Other researchers have proposed methods in which optimized microstructures are first found in key areas, followed by a post-processing step in which these are connected through geometrical interpolation [71, 74]. All these methods have been demonstrated to be effective but they do not guarantee good connectivity [66]. For example, they can lead to sudden changes in geometry which result in undesirable stress concentrations, see figure 1.17a and b. Or, interpolation can lead to disconnected geometry, figure 1.17c.

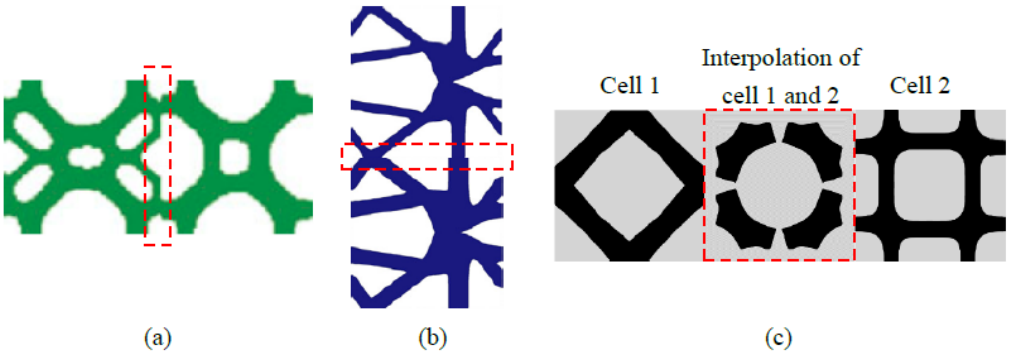

Figure 1.17: Examples of interconnectivity issues due to (a) implicit control methods [73] and (b, c) interpolation methods [71]. Images adapted from ref. [66].

Other methods that have been proposed include making use of an index of connectivity [66], or by introducing compound cells [2]. The first, illustrated in figure 1.18a, considers interface regions between adjacent cells and calculates a numerical value between 0 and 1 to indicate connectivity to be included in the objective function. The second method locally optimizes compound cells, using mechanical properties as a measure for connectivity, illustrated in figure 1.18b.

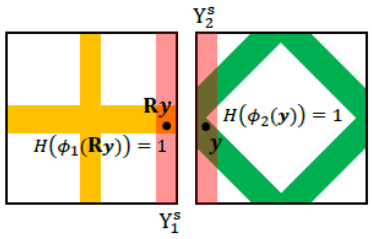

(a) Two adjacent cells with different microstructure. The red area's are used to calculate a connectivity index. Image adapted from ref. [66].

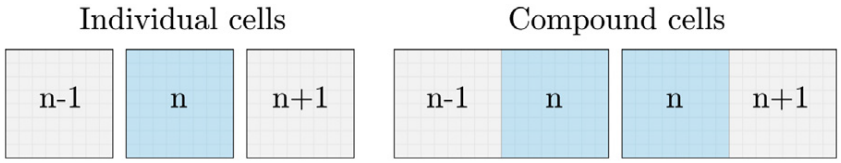

(b) Adjacent cells are grouped together in compound cells to optimize connectivity. Image adapted from ref. [2]

Figure 1.18: Two methods to improve connectivity following the work done by Zhou et al. [64].

1.3 Design principles for mechanical metamaterials

1.3.1 Truss based

This class of metamaterials consists of designs based on trusses and/or flexible hinges, like the example shown in figure 1.1. Geometry means their properties can be approximated using beam theory, which has lead to relatively simple models to predict behaviour. In this chapter the influence of topology will first be discussed followed by a discussion on fractal designs. This special class of truss based metamaterials is made from repeating microstructures at different length scales.

Influence of topology

Meza et al. [49] studied the relationship between truss based architecture and mechanical properties of architected material. Four unit cells, depicted in figure 1.19, of different topology and connectivity were experimentally tested and compared to numerical predictions.

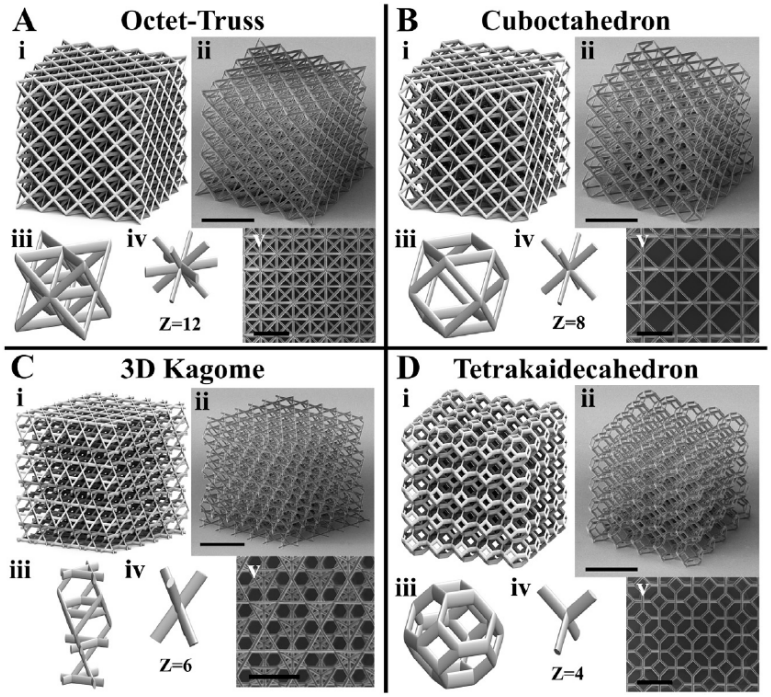

Figure 1.19: Four different topologies with varying connectivity (Z) and rigidity ((A) Rigid, (B) and (C) periodically rigid, and (D) non-rigid) that were used to investigate the influence of architecture on scaling behaviour, image adapted from [49].

The original theory about bending or stretching was derived by ignoring deformation modes like shearing and torsion, and by ignoring effects of nodal intersections. Meza et al. [49] introduced the concept of beam slenderness

$\lambda = \sqrt{AL^2/I}$, with A the cross-sectional surface, L the length and I the moment of inertia of a beam. It was argued that the original assumptions about beam behaviour are valid only when beams can be approximated as being slender ($\lambda > 20$), but break down when this approximation does not hold. The authors extended the analytical model to more accurately describe the elastic modulus for truss structures with non-slender beams. This lead to the following expressions for solid beams, depending on whether the structure is considered rigid or non-rigid,

$$E_{non-rigid} = \frac{E_s}{A_1(\frac{R}{L})^{-2} + A_2(\frac{R}{L})^{-4}}, \tag{1.15a}$$

$$E_{rigid} = \frac{E_s\left(1 + B_3(\frac{R}{L})^{-2}\right)}{B_1(\frac{R}{L})^{-2} + B_2(\frac{R}{L})^{-4}}. \tag{1.15b}$$

Where A_1, A_2, B_1, B_2 and B_3 are geometrical constants and E_s the modulus of the constituent material. Similar expressions were derived for hollow beam structures but will not be included here. These models were tested using FE simulations, and compared to experimental results and the power law theory. Figure 1.20 shows the results for the octet-truss and cuboctahedron architectures, the other two topologies exhibited similar trends.

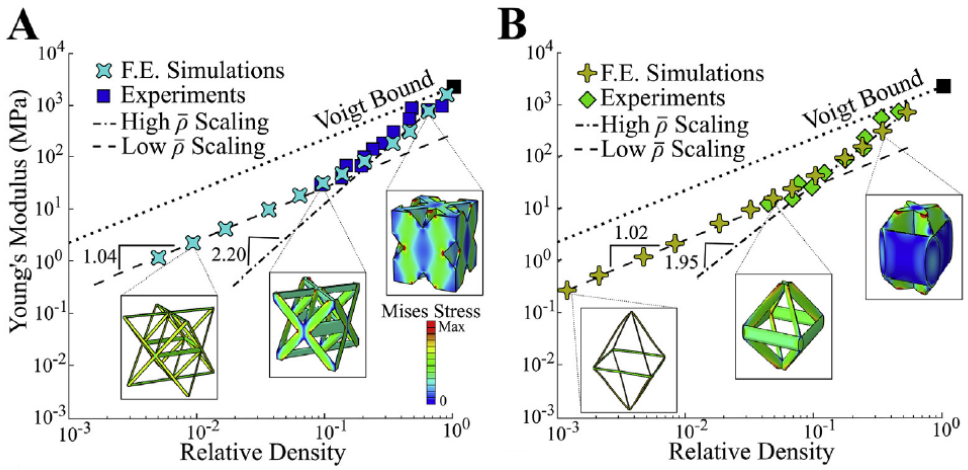

Figure 1.20: Experimental and FE results for the (A) octet-truss and (B) cuboctahedron solid beam structures, indicating high and low scaling regimes and the Voigt bound. The insets show the von Mises stress according to FE simulations. Image adapted from [49].

It was found that the original theory, here called low $\overline{\rho}$ scaling, holds well in case of low density (high slenderness) but it underpredicts stiffness at higher densities. Considering equations 1.15, this can be expected since lower density means larger R/L and therefor a larger effective modulus. Regarding the physics behind transitions, the authors conclude that it is the influence of nodal behaviour that causes the change in scaling behaviour. Increasing density means larger nodes which will contribute measurably to total stiffness. Additionally, the larger nodes lead to shorter beam lengths which effectively makes them stiffer. Both of these effects were ignored in earlier theories. The authors also investigated the behaviour of hollow beams using a similar approach. They considered two governing parameters, R/L the outer radius of the trusses relative to their length, and t/L the wall thickness over relative length. It was found that simulations consistently overestimated stiffness and that the relationship between relative density and modulus is much more complex than for solid beams, figure 1.21.

The overestimation of stiffness was mostly contributed to fabrication errors, which cause the structures to be weaker than their idealized counterparts in FE calculations. Secondly, the parameter space was a result from a highly non-linear relationship between relative density and the two parameters R/L and t/L. This lead to structures with (near) similar $\overline{\rho}$ but with vastly different topology, where one could be a membrane like and the other a near solid truss based structure. In conclusion, the authors stated that simple scaling laws cannot accurately predict the complex behaviour observed in this research.

Structural hierarchy

An important concept in truss-based architecture is that of structural hierarchy, which means that structural components of a design are themselves made up of structural components [75]. These types of structures are found

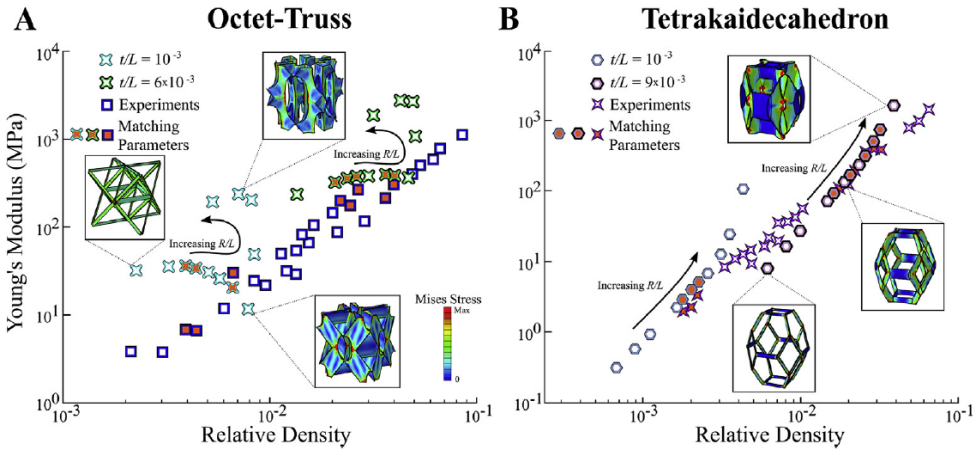

Figure 1.21: Experimental and FE results for the (A) octet-truss and (B) tetrakaidecahedron hollow beam structures for two different values of t/L. Orange coloured data points indicate structures with matching parameters. The insets show the von Mises stress according to FE simulations. Image adapted from [49].

in nature, e.g. bones, and in man-made designs, e.g. Eiffel tower, and have the potential to achieve high specific properties [45]. The hierarchical order of a design is defined as the number of levels of different scales, an example of which is shown in figure 1.22. Provided that the size difference at each level is sufficiently large, each level of hierarchy can be considered to be homogeneous at a higher level.

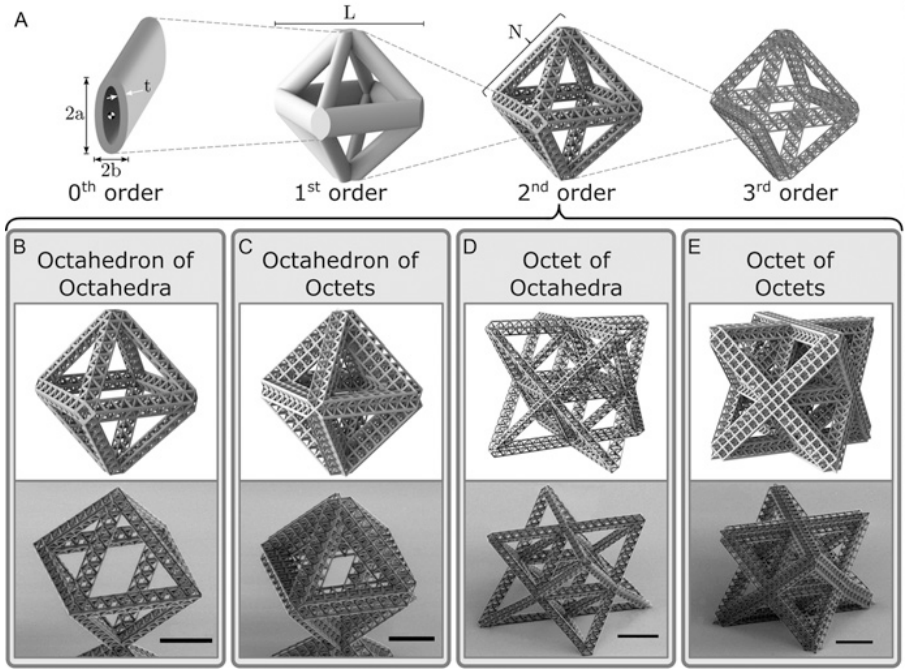

Figure 1.22: An example of a design with four orders of hierarchy, image adapted from ref. [45].

Structures like those depicted in figure 1.22, which have repeating geometry at different levels, are often referred to as fractal designs. The fundamental building blocks of such structures (the 0th order components in figure 1.22) are struts, the properties of which have been the subject of analysis since Euler's study of beam buckling [76]. It is generally accepted that it is preferable to load struts in tension instead of compression due to the possibility of buckling failure from the latter. However, due to the nature of fractal designs, it is very likely that some struts will be loaded in tension, thus buckling is likely to be a limiting factor in any design. The complexity of the designs means that a complete analysis requires complicated FE calculations. Therefor, early research focused mainly on applying the theory of strut behaviour to fractal designs [76, 77, 78, 79].

Simulations and experimental results

These early works relied largely on physical arguments and simplified models to predict properties of truss based lattices. However, in later research these theories could be compared to FE simulations and experimental results [44, 45, 46, 49, 80]. In one such work from 2015, Meza et al. [45], analyzed the structure shown in figure 1.22. Using two-photon lithography first, second and third order structures were created from a polymer material. The polymer then served as a scaffold for an 20nm aluminum oxide (Al_2O_3) layer after which the polymer could be removed to leave a hollow truss alumina structure. The three structures (polymer, polymer + alumina, and hollow alumina) are subjected to compressive loads and results are compared to FEM calculation. Figure 1.23 shows logarithmic plots of the results. For reference, the parameters of the power law model (formulas 1.11 and 1.12) for the second order structure are shown in table 1.3.

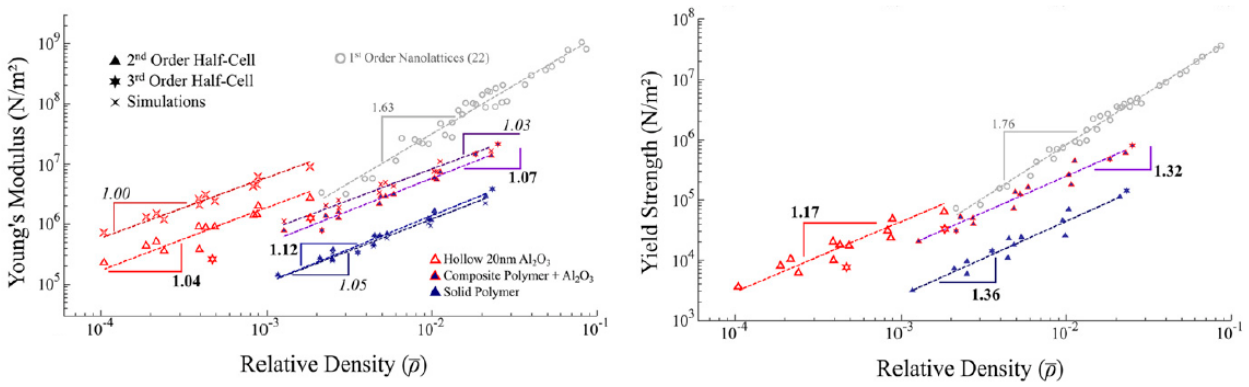

Figure 1.23: (Left) Experimental and simulated values for Young's modulus as function of relative density. (Right) Experimental values for Yield strength as function of relative density. Trend lines following the power law and the associated slopes are included. Image adapted from [45].

Table 1.3: Parameter values for the powerlaw model based on experiments (Exp.) and simulations (Sim.) on second order structures from figure 1.22, values taken from ref. [45].

Material type	E (GPa)	σ_{ys} (MPa)	B		β		C	γ
			Exp.	Sim.	Exp.	Sim.		
Polymer	2.10	62.7	0.110	0.071	1.12	1.05	0.316	1.36
Polymer + 20 nm Al_2O_3	15.8	509	0.050	0.062	1.07	1.04	0.236	1.32
20 nm Al_2O_3	165	5200	0.015	0.036	1.04	1.00	0.026	1.17

The results demonstrate that the power law provides a relatively accurate description of the observed behaviour. The scaling of Young's modulus with relative density is close to linear for higher order structures which is a value associated with stretching dominated structures. However, it should also be noted that the yield strength does not follow the predicted linear scaling. Another observation is the overestimation by the simulations of the elastic modulus. This is explained by the authors as being a result of imperfections as a result from fabrication errors. Lastly, it is interesting to note that, ignoring some discrepancies, the scaling is consistent across most of the generations which suggests that the behaviour is largely controlled by architecture.

Fractal designs

In a paper from 2007, R.S. Farr [76] compared the minimum mass required to withstand a given load for struts of increasing hierarchical order. The least hierarchical structure, labelled 'generation G=0', was a solid rod made of dimensions length (L) and radius (r_0) and made of linear elastic material with Young's modulus (Y) and Poisson's ratio (ν). A solid rod under compression will fail due to Euler buckling when

$$F \geq \pi^2 Y I_0 / L^2. \tag{1.16}$$

Where F is the applied compressive force and I_0 the area moment of inertia according to $I_0 = \pi {r_0}^4/4$. Using this expression, an expression for the minimum required mass was derived as function of the applied force. Next, a

'generation G=1' structure was introduced, which is a hollow rod with parameters length (L), inner diameter (r_1) and homogeneous wall thickness (t_1). In addition to Euler buckling, a hollow rod can also fail due to local buckling when:

$$F \geq \frac{2\pi Y {t_1}^2}{\sqrt{3(1-\nu^2)}}, \tag{1.17}$$

providing an additional constraint to the design. Following the analysis of solid and hollow rods, a composite rod design was proposed consisting of a number of rods with similar radius en wall thickness. This design is shown in figure 1.24 and is called the 'generation G=2' structure.

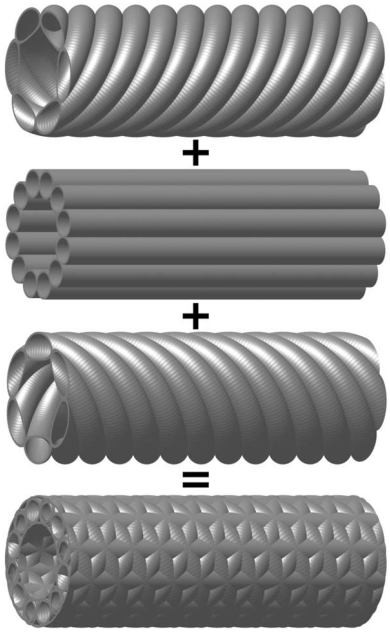

Figure 1.24: Composite design of a tube constructed from hollow rods of similar cross-sectional geometry, image adapted from ref. [76].

In the analysis of this design, the displacement field was analysed by considering each of the intersections to be welded together. However, to calculate the bending and stretching energy a "ghost approximation" was made in which the cylinders are allowed to move through each other as if they are not welded together while obeying the displacement field. As a result, the required weight would likely be overestimated. Additionally, it was assumed that buckling will occur first in the tubes that are aligned with the loading direction, hence these tubes dictate the limits of the design. Finally, a 'generation G=3' design was considered, in which the hollow tubes of generation G=2 were themselves made of composite tubes. The analysis of this structure follows the same principles as generation G=2. Using this approach, the authors derived expressions for the minimum required mass for all of the generations, given a compressive load and a fixed length of the highest hierarchy rod.

Table 1.4: Minimum required mass associated radius for a rod supporting a compressive force of F=10kN with of length L=200m and material parameters similar to steel as calculated by R.S. Farr[76]. Please note that these are theoretical calculations to demonstrate the limits of increased hierarchy.

G	M	r
0	79 tonnes	12.5 cm
1	941 kg	81 cm
2	319 kg	2.4 m
3	216 kg	4.6 m

Using a similar approach, Rayneau-Kirkhope, Farr and Mao [79] studied the behaviour of the same structure but under external pressure instead of a compressive load in one direction. Additionally, a sphere constructed using the same basic components in a football like pattern was investigated, see figure 1.25. The geometry is such that the weakest surfaces have the same properties as the composite layer (figure 1.26a) while the other surfaces are stronger.

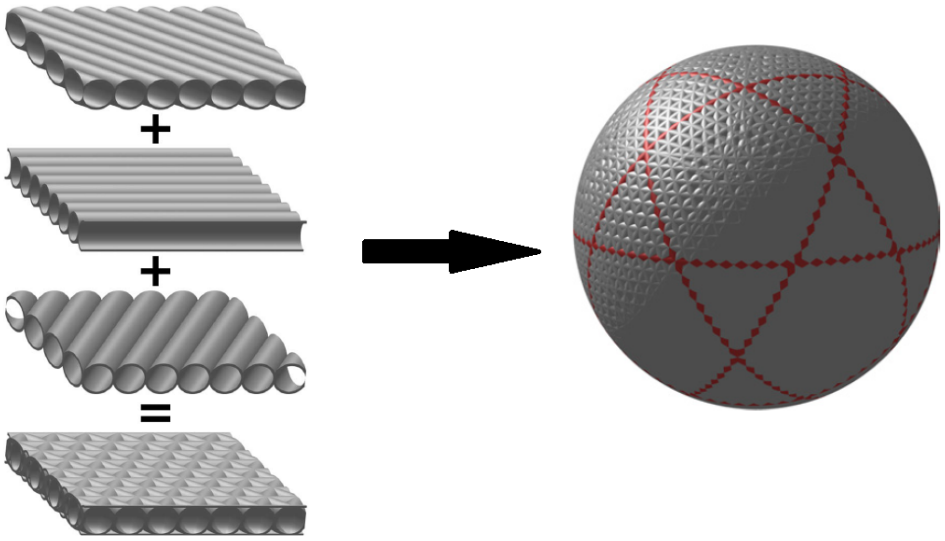

(a) Composite plate **(b)** Sphere

Figure 1.25: Hollow rods are combined to form a composite plate (a) used to produce the surface of a hollow sphere (b). The red lines indicate the interfaces between different surfaces, image adapted from ref. [78, 79].

Again, the two failure modes under consideration were global and local buckling, and a relationship between required volume and applied external pressure was found. This time generation 0 (a solid rod) was not taken into account but a generation 4 structure is included in the analysis. The authors normalised volume and pressure by calculating the ratio of required material volume to enclosed volume ($v = V_{required}/V_{enclosed}$) and the pressure relative to Young's modulus ($p = P/Y$). Using a material with steel like properties (Y=210GPa and ν=0.29), the optimal volume was calculated and results are shown in figure 1.26. The sphere required overall less weight than the rod and in both cases the optimal number of generations decreases with increasing pressure. The authors concluded that terrestrial applications would not benefit from increasing the number of generations beyond 4. Additionally, from the perspective of fabricating these materials, it is interesting to note that the benefit from adding another level hierarchy is almost negligible over a relatively wide pressure range.

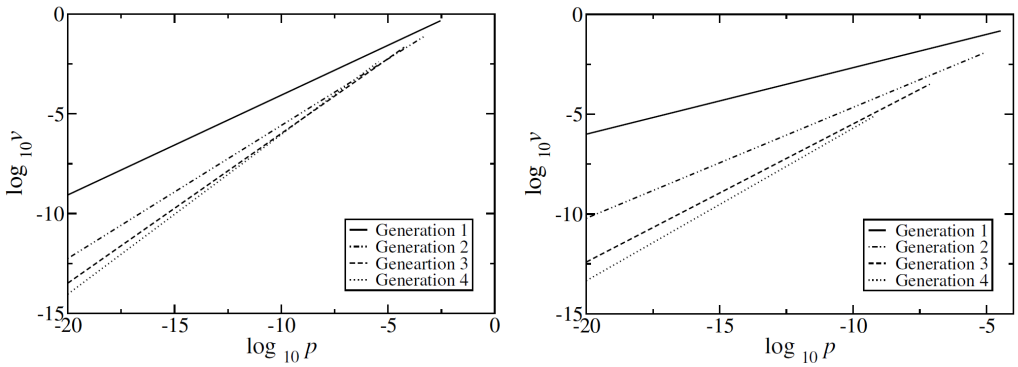

(a) Rod **(b)** Sphere

Figure 1.26: Logarithmic relation between normalised volume (v) and pressure (p) for different generations of rods and spheres, images adapted from [79].

Taking a similar approach, Farr and Mao in 2008 [78] analyzed the influence of increasing hierarchy on fractal space frames subjected to small compressive loads. The space frames were build from stacked octahedra, made from rods with a given length and variable radius, as shown in figure 1.27. Please note that figures 1.27 and 1.28 can best be visualized by holding the paper about 30 cm away and looking behind the paper until the images overlap.

The hierarchy of the structures was increased by replacing the rods by stacked octahedra. The lowest hierarchy structure was referred to as generation 1, and the most complex as generation 3. Hierarchy in tension beams was not increased as this would only increase complexity with no gain in performance. An overview of the different

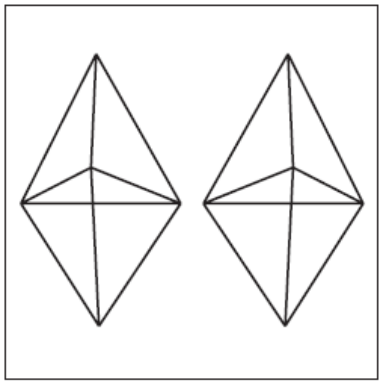

Figure 1.27: Octahedral building blocks used in the fractal space frame analysis by Farr and Mao, image adapted from ref. [78].

generations is given in fig 1.28.

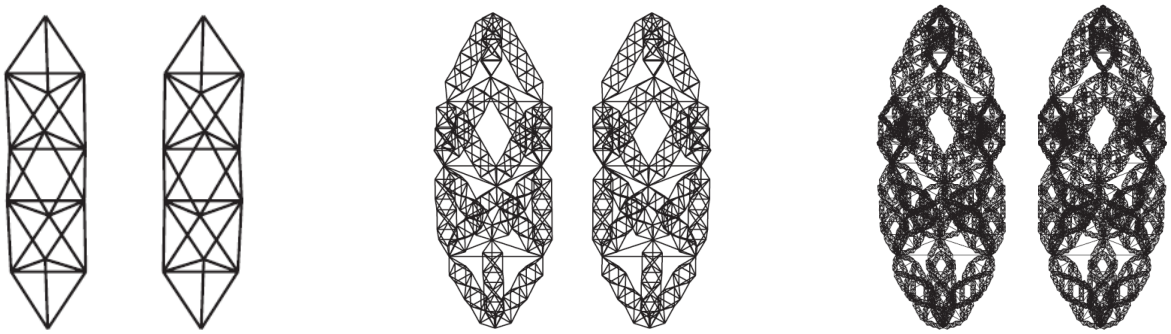

(a) Generation 1 **(b)** Generation 2 **(c)** Generation 3

Figure 1.28: The three generations of increasing hierarchy using fractal space frames, images adapted from ref. [78].

By combining expressions for global and local buckling, the authors derived algebraic expressions to determine the number of stacked octahedra and the radius of the rods at the smallest level. Based on these results, the authors used a rod similar to the one used in the previous analysis, as benchmark to demonstrate the effects of increased hierarchy. The results are summarized in table 1.5. Please note that because of the nature of the space frame designs, there is no global radius that can change independently.

Table 1.5: Minimum required mass associated radius for a fractal space frame supporting a compressive force of F=10kN with of length L=200m and material parameters similar to steel, as calculated by Farr and Mao [78].

G	M
0	79 tonnes
1	2920 kg
2	1790 kg
3	2180 kg

Using this approach, the weight loss due to increased hierarchy was lower than it was for the composite rods. This could be explained by a more limited geometrical design space of the space frames, which leaves less room for optimization. Additionally, it can be noted that for this particular example increasing hierarchy did not improve performance. The authors demonstrated that for any given compressive force there is an optimal number of generations. This research serves as another example of how increased hierarchy can lead to more optimised designs. Additionally, it demonstrated that theoretical models of relative complex models can be derived from basic principles of beam buckling.

1.3.2 Origami and Kirigami

Origami and kirigami metametarials are based on the concepts of the old Japenese papercraft, which was introduced in Japan around the 6th century A.D.[81]. The original craft involves either the folding ("ori") or cutting ("kiri") of paper ("gami" or "kami")[82]. This technique allows engineers to construct three dimensional structures from initially flat thin layered materials [82]. Conversely, it allows complex three dimensional structures to fold up into relatively compact spaces which can be beneficial for transportation to hard to reach locations. Nowadays, scientists are not limited to paper but apply this method to various materials including polymers, metals, aerogels and graphene, and at length scales as small as the nanometer scale [83]. Interest in this field has increased in recent years due to the potential to achieve exotic properties [84]. Additionally, mathematical tools have led to methods to design complex structures which are, at least partially, designed by computers [85]. Also, it has been demonstrated that any shape can in principle be approximated from a flat sheet [86].

Categories

The architectures can broadly be divided into three categories origami only, kirigami only and hybrid. Furthermore, a distinction can be made between rigid and deformable structures, based on where mechanical energy is stored. Rigid structures only contain stored mechanical energy in the folds or linkage areas while the panels stay rigid during shape changes. In deformable structures, energy is stored in the panels as well, leading to possible shape changes of the panels as well as along the folds or linkages[83]. A Venn diagram showing the different categories is shown in figure 1.29.

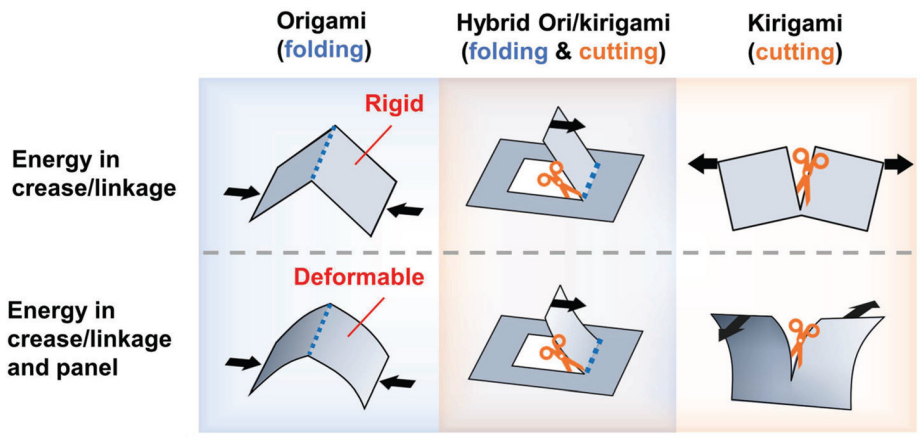

Figure 1.29: An overview of the various methods by which origami and kirigami structures can be made. Image adapted from [83].

Miura-ori

One of the earliest works on this topic was produced by K. Miura in 1969 [87] in which the post-buckling shapes of thin film cylinders were considered. It was demonstrated that these surfaces introduce unique and useful features to the surface, like increased bending rigidity. These structures are nowadays referred to as Miura-ori and have attracted interest due to their combination of versatility and relative simplicity [84, 88, 89].

Miura-ori structures are based on periodic parallelograms based in a herring-bone pattern of mountains and valley creases, see figure 1.30a. Their primary features are the following [90]:

- They are deployed homogeneous and simultaneously in orthogonal directions.
- They possess a single degree of freedom of motion.
- Deployment and retraction follow the same path.

In principle, a Miura-ori is uniquely defined by lengths a and b, angle γ, and folding angle θ, see figure 1.30b[88]. An interesting property of Miura-ori is that they have negative in-plane Poisson's ratio.

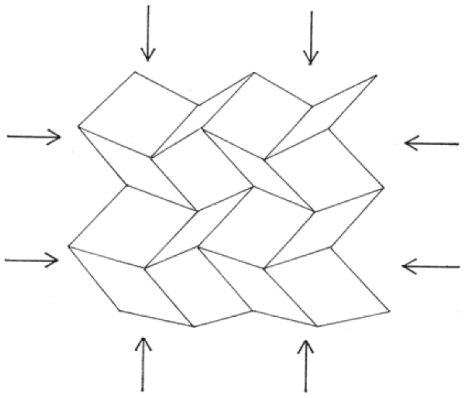

(a) Miura-ori pattern on a flat surface, image adapted from [90].

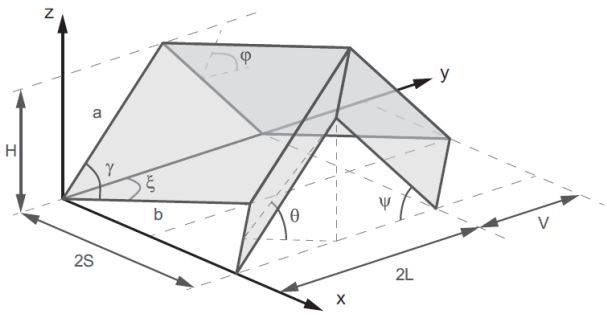

(b) An overview of relevant angles and lengths in a Miura-ori unit cell. A unit cell can be uniquely defined through a, b, γ and θ, image adapted from [88].

Figure 1.30: A Miura-ori patterned sheet (a) and a single unit cell (b).

Deployment strategies

In addition to finding methods to optimize origami and kirigami designs for specific properties, researchers have considered various strategies to deploy them[82, 85, 91, 92, 93]. The most common method of deployment is through the application of external force, but this might not always be a viable method[82]. Thus, strategies to deploy under different stimuli have been developed. Amongst others, they include temperature [93], light [92] and moisture [94]. An overview of various methods and potential applications is provided in table 1.6.

Table 1.6: An overview of strategies for deploying origami and kirigami based metamaterials [82, 92, 94, 95].

Material	Stimulus	Output
Polymeric gal	pH change	Swelling or contracting
Electro-rheological fluid	Electrical signal	Viscosity change
Smart metal alloys	Temperature	Shape
Dielectric elastomers	Voltage	Strain
Liquid crystal networks	Light	Stiffness change
Piezoeletric material	Voltage	Strain
Hydrogel	Water	Swelling

Although the materials and stimuli may differ vastly between the different approaches, their core principles are similar. By using materials with different responses to relevant stimuli, material properties can be changed locally to induce shape changes. These changes can cause local shape changes which influence the topology of the structure as a whole.

Consider for example figure 1.31, where three methodologies are presented. Figure 1.31a shows a sandwich of relatively soft orange material between stiff blue outer layers. Blue material has been removed strategically at a specific location to induce bending upon expansion of the inner layer. In the case that the orange material shrinks, the material will bend in the opposite direction. Figure 1.31b shows an orange film with local adhesion of (a different) blue material. The blue material can be induced to shrink or expand which can lead to an overall shape change of the structure. In this example the blue material shrinks and causes the substrate to bend upwards. In figure 1.31c local inhomogeneity in the substrate is displayed as the dark orange area. In the example, the inhomogeneity expands more than the rest of the substrate leading to the depicted deformation, but the opposite reaction could also be triggered if the inhomogeneity would expand less than the surrounding material. In all of the examples above, no specific materials or stimuli were assumed suggesting that these strategies can be applied to various combinations of materials. Recently, these methods have been used to induce shape changes after deployment [91] and even to create moving structures [92].

Foam based methods

Methods that have been discussed up to this point were based on stiff trusses and/or plates. Within reasonable limits, their behaviour can be approximated by relatively simple models, see section 1.3.1, but fabricating them

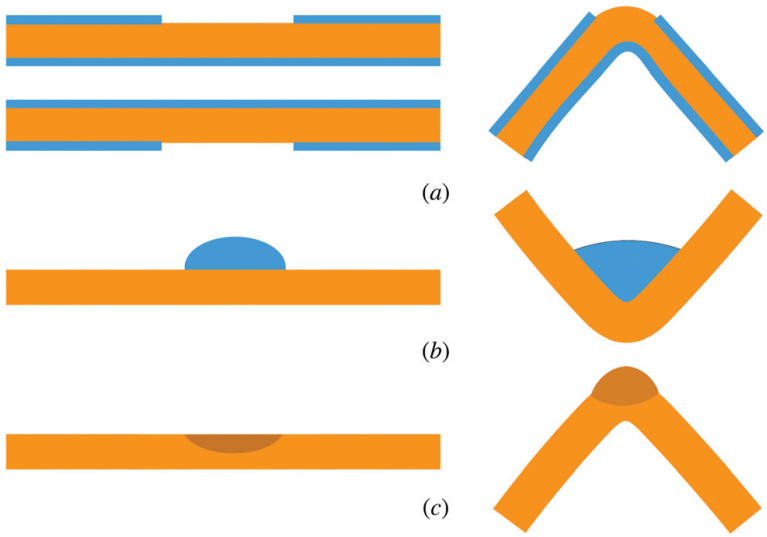

Figure 1.31: Strategies for deployment of origami and kirigami structures under external stimuli, (a) sandwich with swelling material, (b) local surface deposition and (c) material inhomogeneity, image adapted from ref. [85].

poses significant challenges [96]. Additionally, they can be highly sensitive to fabrication errors, leading to lower than predicted performance, see figures 1.23 and 1.21. By taking inspiration from nature, like the Venus flytrap [97], scientists have been developing metamaterials from soft materials, like elastomers, to create foam based metamaterials [31]. Research has been done on both 2D and 3D metamaterials and it has been demonstrated that patterned soft matter structures can produce a wide variety of properties [1, 31, 98, 99]. For 3D foams a distinction can be made between closed and open cell structures. In closed cell structures, each cell is separated by a membrane like surface while in an open cell structures the cells are connected [100]. In an early study from 2007 on 2D foams, T. Mullin et al. [99] investigated the effects of periodic circular holes in a 9.4mm thick sheet of photoelastic elastomer under uniaxial compression. By measuring nominal stress and nominal strain, it was found that the material would initially behave linearly elastic. When a critical point was reached, elastic buckling instability lead to a shape transformation, resulting in a vastly different stress-strain response, see figure 1.32.

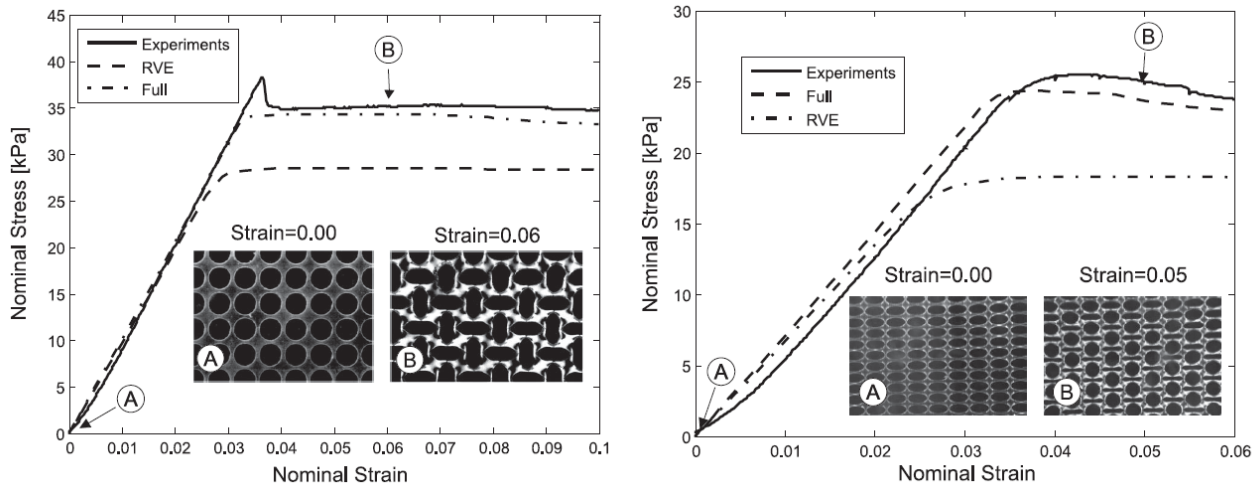

Figure 1.32: Experimental and simulation (Full and Representative Volume Elements (RVE)) results for nominal stress vs nominal strain due to compression for the patterns displayed in the insets. The peaks indicate the transition from linear elastic behaviour to buckling instability, image adapted from ref. [99].

Two important conclusions followed from this research. Firstly, this process is completely reversible, and secondly, the final properties can be engineered through pattern design. These aspects were studied in more detail in a paper from 2008 by K. Bertoldi et al. [101]. In this paper, elliptical holes in a square elastomer plate were studied and theoretical models and simulations were compared to experimental results. Non-linear behaviour was found, similar to that shown in figure 1.32, and it was confirmed that it was caused by elastic instability. Additionally, it was

demonstrated that the pattern transformation is uniform and occurs simultaneously throughout the material. Following eigenvalue analyses, it was concluded that it might be possible to trigger alternative responses if the dominating deformation mode could be suppressed.

Re-entrant, chiral and rotating polygons

Foam based materials have successfully been used to create auxetic materials. One of the first reports of such materials comes from 1987 by R. Lakes [102]. In this research, a conventional foam (with positive ν) was softened and subsequently hardened under pressure. The cells obtained this way had inward protruding ribs, an idealised version of which is shown in figure 1.33. Using this methods, negative Poisson's ratio's of -0.7 were achieved.

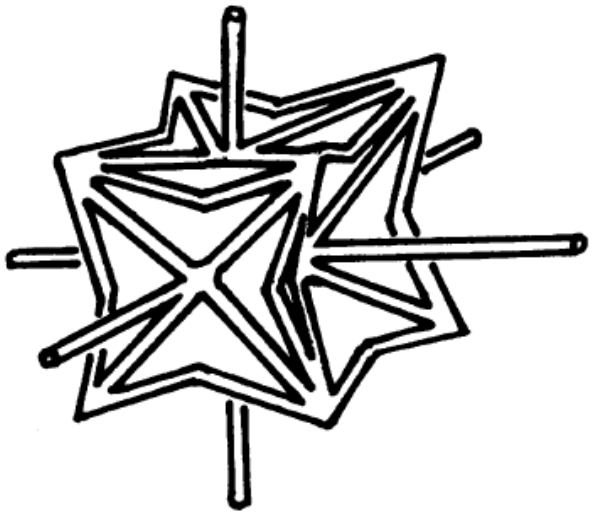

Figure 1.33: Idealised unit cell of the auxetic foams fabricated by R. Lakes in 1987, image adapted from ref. [102].

These types of auxetic structures are called "re-entrant" type and are characterized by the outward movement of the diagonal ribs under tension. Analytical models have been created to characterize their properties [103]. Two other common types of auxetic structures are "chiral type" and "rotating polygons" [104, 105, 106]. Chiral type structures are characterized by rotating parts connected by ligaments. Rotating polygons are structures of repeating polygons connected through hinges that rotate when loaded, examples of both are given in figure 1.34.

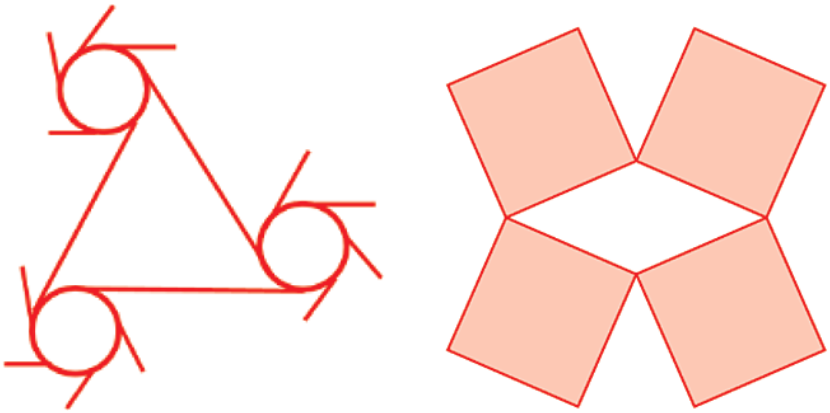

(a) A 2D chiral structure made of rotating circles and connecting ligaments that unwind when stretched.

(b) A 2D rotating polygon structure of cubes connected at the corners with hinges.

Figure 1.34: Examples of auxetic structures based on chiral type and rotating polygons, images adapted from [104].

Manipulating macroscale variables like pressure and temperature was a common method to fabricate auxetic materials in the 1990s and early 2000s [50, 107, 108, 109, 110, 111, 112]. Although scientists were able to produce reliable results, the methods were relatively crude and did not allow for precise microstructural manipulation. The

resulting materials can be classified as stochastic foams [98]. This changed with the advent of new techniques like additive manufacturing which allowed for the fabrication of much more precise microstructures and the ability to create periodic architecture, which can be classified as lattice structures [98, 113].

Instability based

Taking inspiration from the work done by R. Lakes in 1987 [102], and following the work done on sheets with circular holes [99, 101], Bertoldi et al. in 2010 [114], investigated the the auxetic behaviour of these sheets. The researchers compared experimental evidence with FE calculations and studied the effect of void size on a flat specimen with a square grid of circular holes. Two collapse mechanisms were identified: microscopic and macroscopic instability. Microscopic instability leads to simultaneous collapse throughout the sample while macroscopic instability leads to local collapse in the form of bands, schematically shown in the insets in 1.35a. By defining the volume fraction (ϕ) as the area of voids divided by the total area, it was found that the microscopic instability occurs only at ϕ>0.34, reported in figure 1.35a.

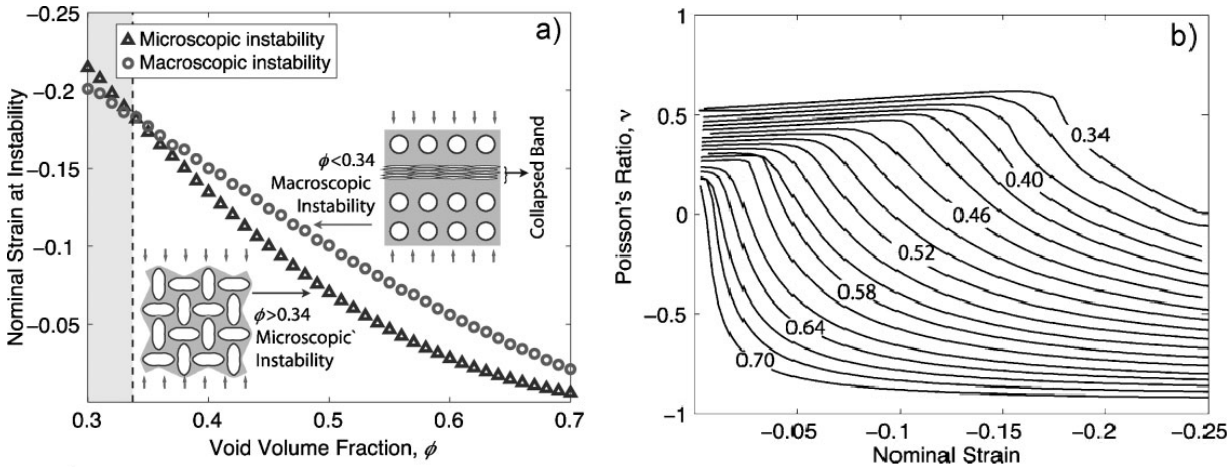

Figure 1.35: FE investigation on the effect of void fraction (ϕ) of a flat elastomeric specimen with a square grid of circular holes. a) Nominal strain at which instability occurs vs void volume fraction. The insets schematically show the different collapse mechanisms. The grey area indicates volume fractions of ϕ<0.34. b) Poisson's ratio at various void fractions against nominal strain. Images adapted from ref. [114] .

Additionally, it was reported that three properties could be increased by increasing ϕ: the critical strain at which instability occurs, the rate at which the asymptotic Poisson's value is reached and the asymptotic value itself, reported in figure 1.35b.

In a follow up study in 2012 by Overvelde et al. [96], the effect of pore shape was studied under similar conditions, shown in figure 1.36. It was found that the cross-shaped holes (shape B) produced lower asymptotic Poisson's values than circular shaped holes at similar void fractions. Shape C on the other hand, did not exhibit auxetic behaviour regardless of void fraction.

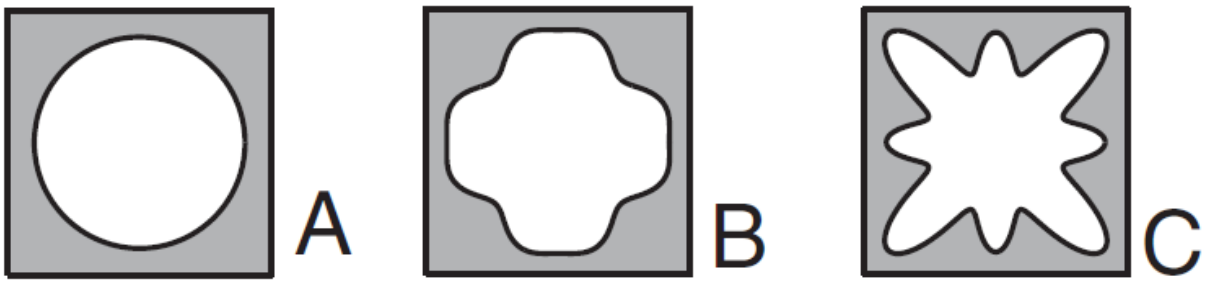

Figure 1.36: Pore shapes used to investigate their effect on auxetic behaviour, image adapted from ref. [96].

In a paper from 2018 by Mizzi et al. [115] star shaped metamaterials were used to produce tunable Poisson's ratio's between 0 and -1. Yet research on auxetic materials has not been limited to 2D structures and attempts have

been made to produce 3D auxetics as well [1, 104, 116].

Triply periodic minimal surfaces

A major challenge in designing 3D metamaterials, is finding designs with desirable properties that can fill an arbitrary volume. Babaee et al [1], used interlocking Bucklicrystals of various geometries to produce 3D metamaterials with Poisson's ratio's between 0 and -0.5 [1]. But such an approach relies on finding interlocking building blocks, which limits the design space. An alternative approach has been to use Triply Periodic Minimal Surfaces (TPMS) [98, 117, 118, 119, 120].

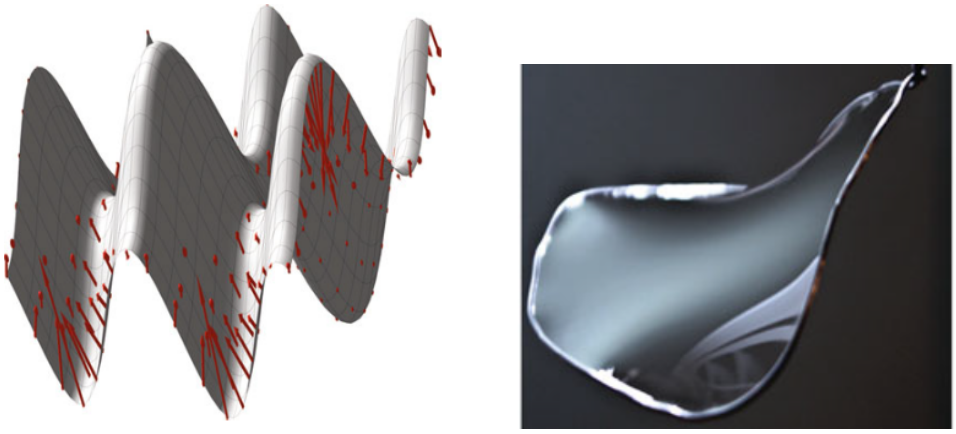

(a) Mean curvature field for the surface $z = \sin x + \cos y$.

(b) A natural minimal surface formed by a soap film.

Figure 1.37: Visualisation of (a) a minimal surface and (b) a naturally formed minimal surface, images adapted from ref. [121].

A minimal surface is one that has mean zero curvature everywhere [121, 122]. This means that there is no displacement field that can be applied to the surface that would results in a decrease in surface area. For example, consider figure 1.37a in which mean curvature is plotted using red arrows. It would be possible to minimize this surface by by a displacement in the direction of curvature, with the minimal solution being a flat surface. This is in contrast to the soap film depicted in figure 1.37b, where no displacement field can be found that would lead to a decrease in surface area. Triply periodic minimal surfaces are surfaces that meet the minimal surface requirements while also being periodic in three orthogonal directions [119]. Some of their interesting properties include [120]:

- They can extend infinitely.
- Have a symmetry group of one of the crystallographic space groups.
- No self-intersection of the surface.
- Divides space into two separated but intertwined regions.
- The two regions are continuous.

As a result of minimal surface requirement, surfaces will always be smooth which means the resulting architecture could be less sensitive to fabrication errors and stress concentrations than other methods, such as truss-based lattices. One of the first reports on TPMS topology is from 1890 by H.A. Schwarz [123], but it would not be until 1970 before research in the field was furthered by A.H. Schoen [124], with the aid of early computers.

Although the definition of TPMS is mathematically well defined, there is not a straightforward method of finding and describing every surface that meets these conditions. Nonetheless, since the 1970s at least one hundred have been found [125]. Some of these can be parameterized using relatively simple expressions of the form

$$\phi(x, y, z) = c, \tag{1.18}$$

where ϕ is a function of orthogonal directions x, y and z, and c a constant, see figure 1.38. However, not every TPMS can be described in this manner [98, 126]. Generally, TPMS can be divided into two classes: balanced and unbalanced [117]. Balanced surfaces divide the space into two equal volumes. These volumes can be each others mirror image (Gyroid, figure 1.38b), or not (Primitive, figure 1.38a). If the TPMS divides space into two unequal volumes it is considered to be unbalanced (figure 1.38c). The mathematical descriptions that have been

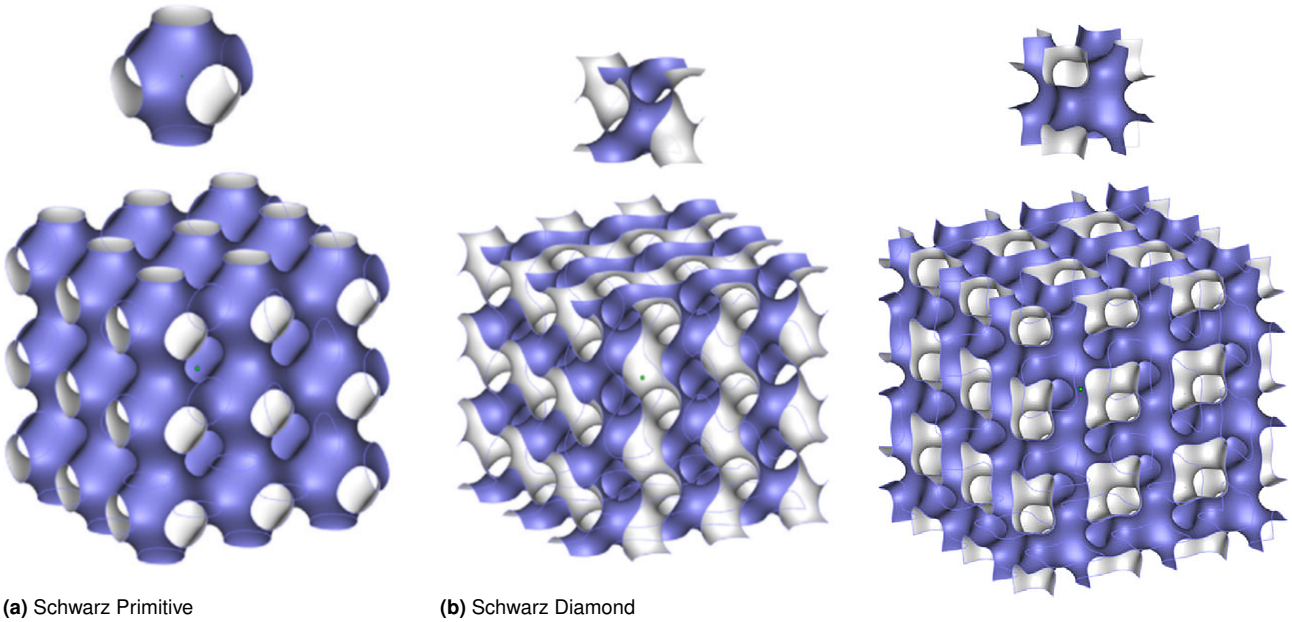

(a) Schwarz Primitive
$\cos x + \cos y + \cos z = c$

(b) Schwarz Diamond
$\cos x \cos y \cos z - \sin x \sin y \sin z = c$

(c) Schoen-IWP
$2(\cos x \cos y + \cos y \cos z + \cos z \cos x) - (\cos 2x + \cos 2y + \cos 2z) = c$

Figure 1.38: Surfaces plots of selected TPMS with their parametric expressions, where $x = 2\pi X/L_x$, $y = 2\pi Y/L_y$, $z = 2\pi Z/L_z$, and L_x, L_y, and L_z are the dimensions of the unit cells in X, Y and Z directions, images adapted from ref. [98].

discussed up to know describe mathematical surfaces of zero thickness. In order to use these topologies to produce metamaterial architecture, two strategies can be employed: minimal surface network solids or minimal surface sheet solids [127, 128, 129]. Minimal surface network solids are created by taking a TPMS and filling one of the volume domains with material while the other domain is left void. In a minimal surface sheet approach, two surfaces of similar expression in terms of 1.18, but with a different offset in the value for c relative to a level-set value. By increasing or decreasing c a surface with a constant offset relative to the level-set surface will be produced [98]. Plotting two functions with an offset of similar magnitude but opposite sign, will create two surfaces that never intersect and encapsulate a volume domain that can be used as a scaffold for metamaterial. An example of both methods for the same Schoen-IWP surface is given in figure 1.39.

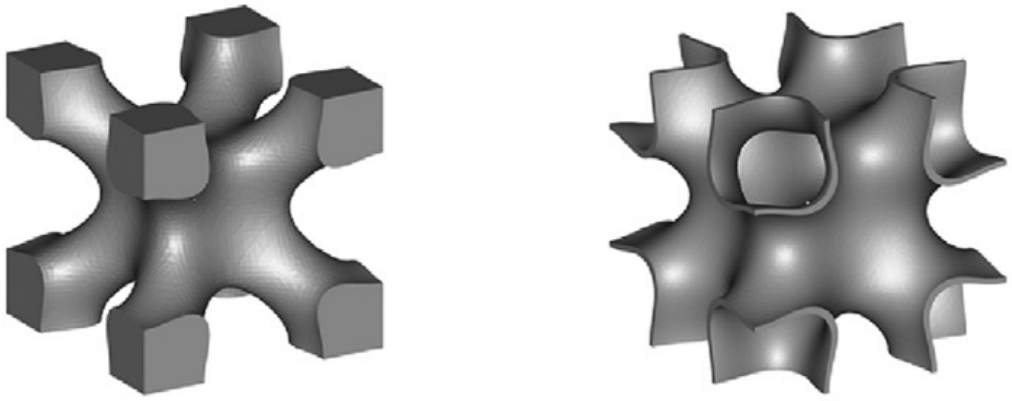

Figure 1.39: Minimal surface network solid (left) and sheet (right) based on the same Schoen-IWP surface, image adapted from ref. [127].

As might be expected, the two approaches lead to different specific properties of the resulting metamaterial. In a comparative study by Al-Ketan et al. [98] the results of several papers were considered. Specifically, the influence of volume fraction on Young's modulus and compressive strength was analysed and plotted in an Ashby graph, figure 1.40. The reported values indicate that sheet networks generally lead to higher moduli and strength. Although a comprehensive explanation for this behaviour has not yet been proposed, research has been done to investigate

these results. For example, it has been demonstrated that sheet-networks show near stretching dominated behaviour while solid-networks show bending dominated behaviour [127]. Others have compared the difference between the two approaches as the difference between hollow and solid steel rods [129]. Hollow rods are generally favourable over solid rods at equal mass as the moment of inertia will contribute to stiffness. Sheet-networks are the hollow rod equivalent to solid-networks, which can be considered to be constructed of solid rods.

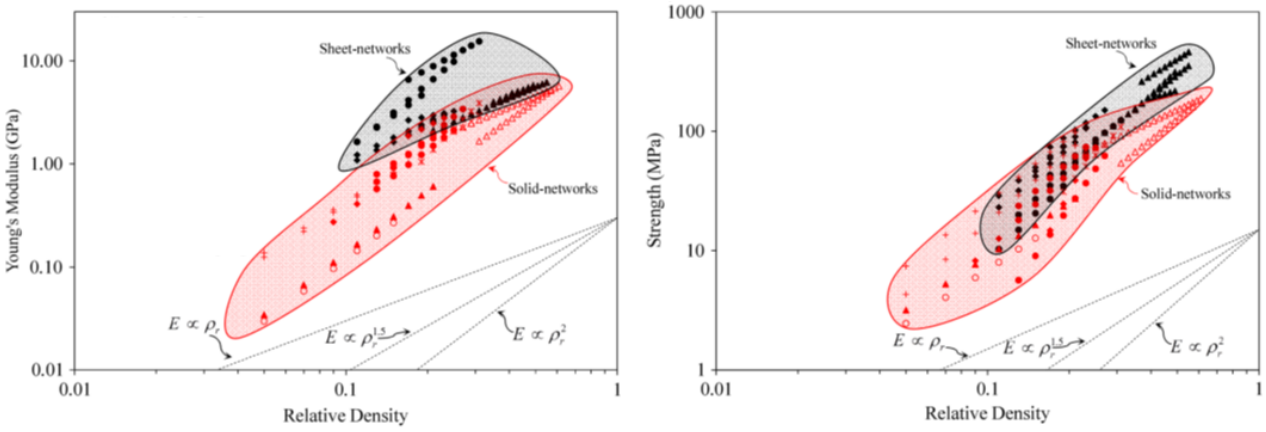

Figure 1.40: Ashbey charts of Young's modulus (left) and compressive strength (right) as function of relative density for solid- and sheet-networks. Data points are associated with various studies. Image adapted from [98].

In a study from 2017 by Han et al. [130], sheet based TPMS metamaterial performance experimentally compared to equivalent strut and rod based architectures. It was found that all specimen had lower properties than those predicted by simulations, but the differences were smaller in TPMS sheet based materials than in other samples. These findings were confirmed in a numerical analyses on the influence of imperfections on sheet buckling, by J.W. Hutchinson and J.M.T. Thompson in 2018 [131]. Finally, it should be noted that due to the possible complexity of the desired topology, manufacturing can be challenging and potentially difficult to scale up [98, 130, 131, 132].

Spinodoid

To address the challenges mentioned in the previous section, scientists have considered alternative methods to design metamaterial foams. One such method involves using spinodal, or spinodoid (spinodal-like) designs, which are based on spinodal decomposition [133]. This is a naturally occurring process of phase separation, which could lead to convenient fabrication methods through large scale self assembly [134]. Stability of a two phase system is governed by the free energy [135]. A system will try to go to the lowest energy state and in 1958 J.W. Cahn and J.E. Hilliard [136] formulated a general expression for the free energy ($f(c)$) a dual phase system with a one-dimensional compositional variation ($c(x)$) and cross-sectional area (A):

$$F(c(x)) = A \int \left(f(c) + K \left(\frac{dc}{dx} \right)^2 \right) dx, \tag{1.19}$$

where K is the gradient-energy coefficient which is a positive material related constant. This equation is commonly referred to as the Cahn-Hilliard equation and is often used in studies on spinodal decomposition. From 1.20 a one-dimensional diffusion equation can be found according to:

$$\frac{\partial c}{\partial t} = D \left(\frac{\partial^2 c}{\partial x^2} - \left(2K / \frac{\partial^2 f}{\partial c^2} \right) \frac{\partial^4 c}{\partial x^4} \right), \tag{1.20}$$

with D the diffusion coefficient. The diffusion coefficient is an important parameter to determine if a system will undergo spinal decomposition [137]. A negative value of D means that variations in concentration will be reinforced, leading to "uphill" diffusion, whereas a positive value will promote homogeneity [135]. It has been demonstrated that the sign of D is directly related to the sign of the second derivative of the Gibb's free energy (G) [138, 139].

Consider the Gibb's free energy curve in figure 1.41b for a dual phase system, where the horizontal axis shows the relative concentration of phase B (X_B), with $X_A = 1 - X_B$. When a system with $X_B = X_0{}'$ in homogeneous state α is cooled down from T_1 to T_2, the system goes to a point on $G(T_2)$ where $d^2G/dX^2 > 0$. This means that a change

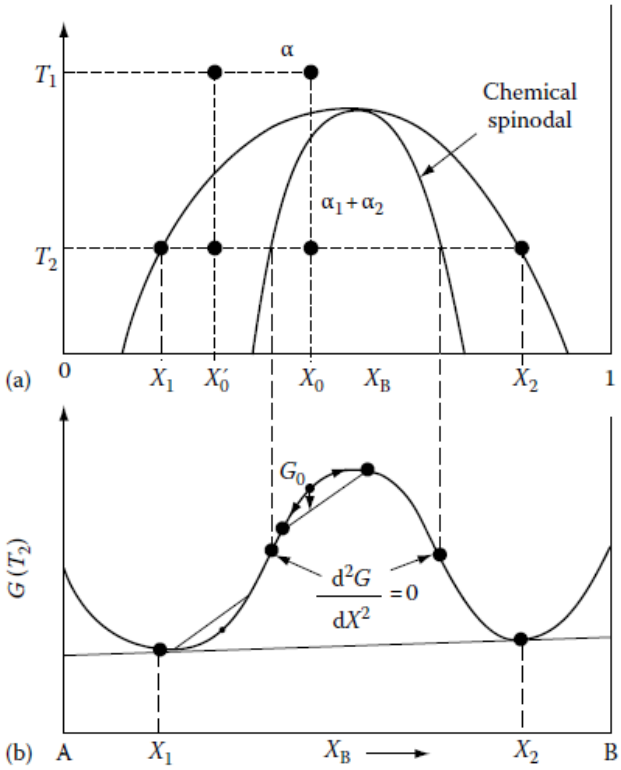

Figure 1.41: (a) Phase diagram at T_2 of a dual phase system indicating the metastable and spinodal regions and (b) the associated Gibb's free energy curve indicating the inflection point ($\frac{d^2G}{dX^2} = 0$) which marks the transition from a metastable state to spinodal decomposition. Image adapted from [135].

in composition would lead to an increase in free energy and thus small changes in composition will homogenise. However, energy would be reduced if the phases would split into two phases, α_1 and α_2, with relative concentrations X_1 and X_2. Meaning that if such phases nucleate they will subsequently grow, figure 1.42(left). However, in the absence of nuclei the mixture will remain homogeneous in a metastable state. Now consider a system in state α with $X_B = X_0$ undergoing the same temperature transformation. The system is now in a state where $\frac{d^2G}{dX^2} < 0$, meaning that any change in concentration will lower the free energy of the system. This enhances small fluctuations in composition causing phase separation over time. This is called spinodal decomposition 1.42(right).

Spinodal decomposition starts with seperation of two phases, followed by coarsening. The resulting microstructure resembles a network of the two phases of which one could be a void to create a solid network metamaterial. Alternatively, sheet networks can be created by applying a similar method as described for TPMS. The surfaces have been shown to have near uniform negative Gaussian curvature and low mean curvature [139, 140, 141]. Additionally, it is possible to vary relative composition of the different phases, and duration of the spinodal decomposition, to achieve different topologies, see figure 1.43. The evolution of spinodal morphology has been the topic of much interest [141, 142, 143, 144]. These investigations typically rely on numerical phase field models in combination with the Cahn-Hilliard expression for mixtures. In a 2019 review paper, Hsieh et al. [134] sum up the most important conclusions for spinodal decomposition with isotropic surface energies as follows:

- Spinodal morphologies have isotropic properties.
- Characteristic feature size increases with evolution time.
- The dominant feature size is a function of time only and independent of relative density.

The characteristic feature size is a parameter that represents the main feature dimensions and is used to quantify topology evolution. Even though the dominant feature size is independent of relative density, the evolution speed is not, as can be seen in figure 1.44 [141]. However, not all spinodal mixtures develop isotropically, in many cases the surface energy is anisotropic, lead to anisotropic microstructures[65, 145]. This process had already been observed to happen in crystal faceting in 1901 [146]. Fifty years later, C. Herring [147] showed that this was caused by a non-convex surface energy in the direction of the surface normal. Subsequently, N. Cabrera in 1964 [148], demonstrated that this crystallographic process was similar to anisoptropic spinodal decomposition. The interest in anisotropic

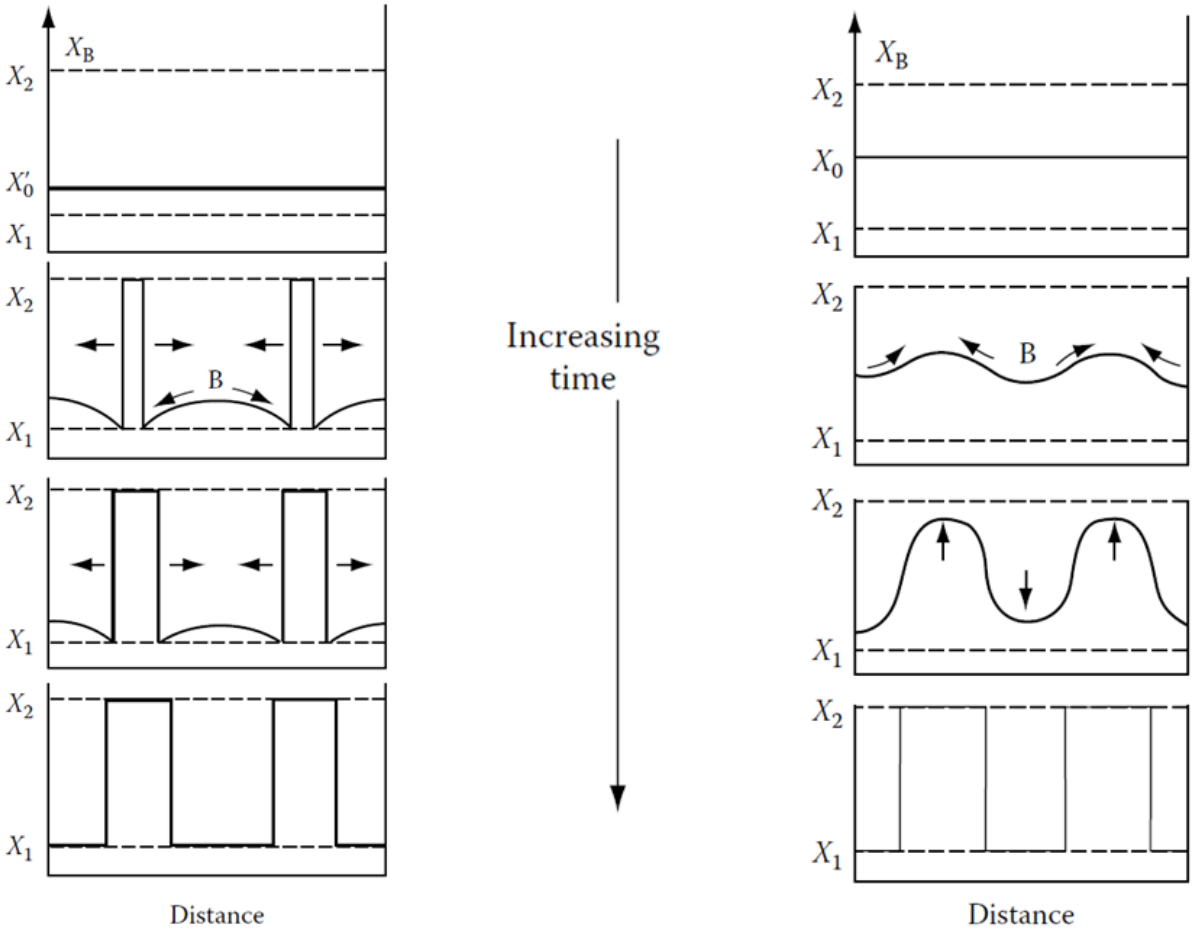

Figure 1.42: Schematic representation of a 1-D system undergoing phase transition due to a sudden temperature change showing nucleation and growth (left) and spinodal decomposition (right). Image adapted from ref. [135].

spinodal structures comes from their potential to generate connected heterogeneous microstructures[133]. It has been demonstrated that anisotropic spinodoid designs can achieve stiffness close to the Voigt bound [149]. However, numerically simulations using phase field models is challenging because of the formation of sharp edges [150]. Attempts to overcome these challenges have been made since the early 1990s [151, 152]. But these attempts were mostly limited to large scale models using smooth surface approximations, which limits their predictive utility [153]. In recent years more optimized methods have been proposed which make use of homogenization and regularization techniques to overcome small scale fluctuations [145, 150, 154]. One major downside to these techniques is that they solve the time-dependent Cahn-Hilliard formulation which can be a time consuming process [155]. In attempt to overcome this problem, researchers have applied Machine Learning (ML) techniques to anisotropic spinodoid designs [65, 156]. In one such example from 2020, Kumar et al. [65] used two ML models to predict and generate anisotropic designs. The first model was trained to predict mechanical properties of random topologies (the forward model), thereby bypassing expensive FE simulations. The second model (inverse model) was used to predict a topology based on a queried stiffness. This process is schematically represented by figure 1.45. Such an approach does not only significantly reduce computing time, it also provides a way to implement inverse homogenization. It was demonstrated that this technique was able to reproduce mechanical properties of trabecular bones [65].

Growth based

While spinodoid designs take inspiration from natural processes, other methods rely on mathematical theories. In particular, growth based Voronoi models have been demonstrated to provide an efficient method to flexibly design easy to fabricate metamaterials. This has been the subject of research in recent years by Martinez et al. [157, 158, 159]. Specifically for the purpose of 3D printing, due to its versatility and wide availability. The requirements put on the design by the condition that it can be 3D printed have been defined as follows [158]:

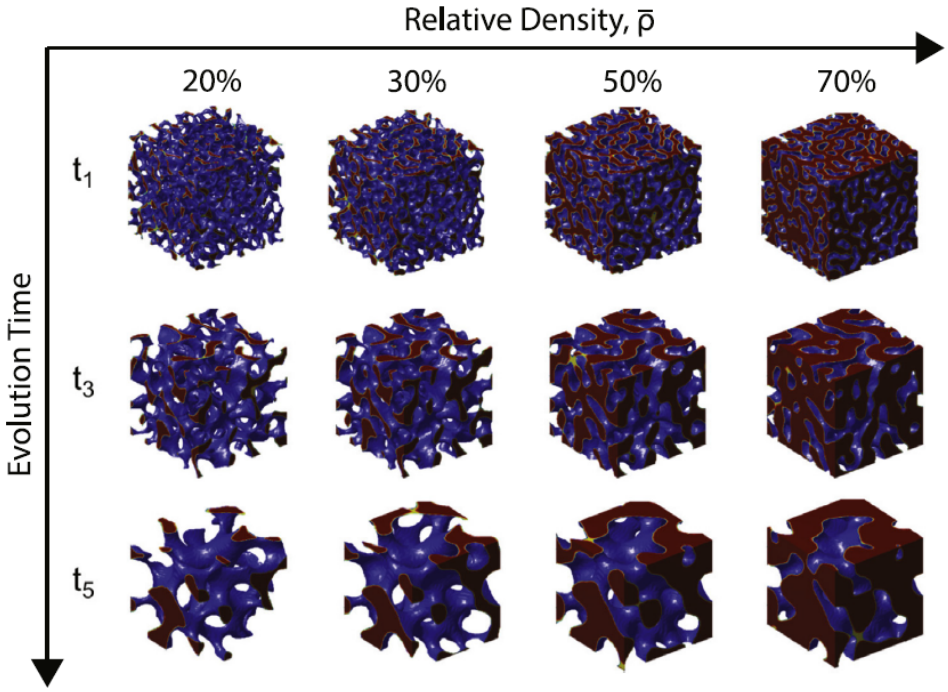

Figure 1.43: The effect of evolution time and relative density on the topology of solid spinodal structures. Image adapted from ref. [134].

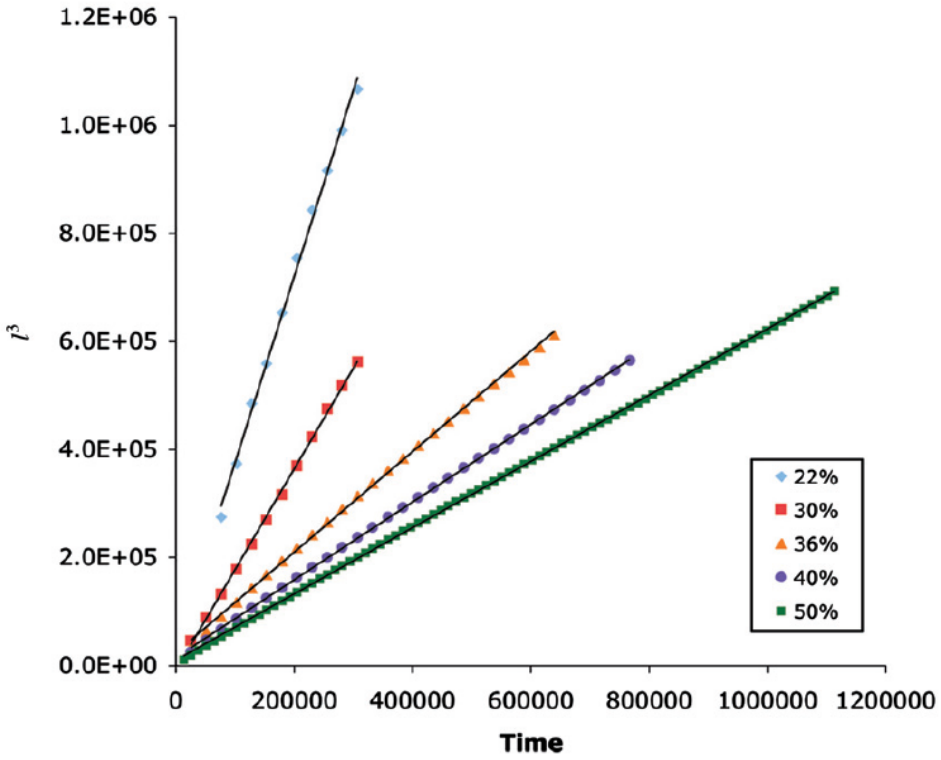

Figure 1.44: The effect of evolution time and relative density on characteristic feature size of spinodal structures. The different colours indicate different relative densities and characteristic length l is defined as $1/S_v$, with S_v the area surface per unit volume. Image adapted from ref. [141].

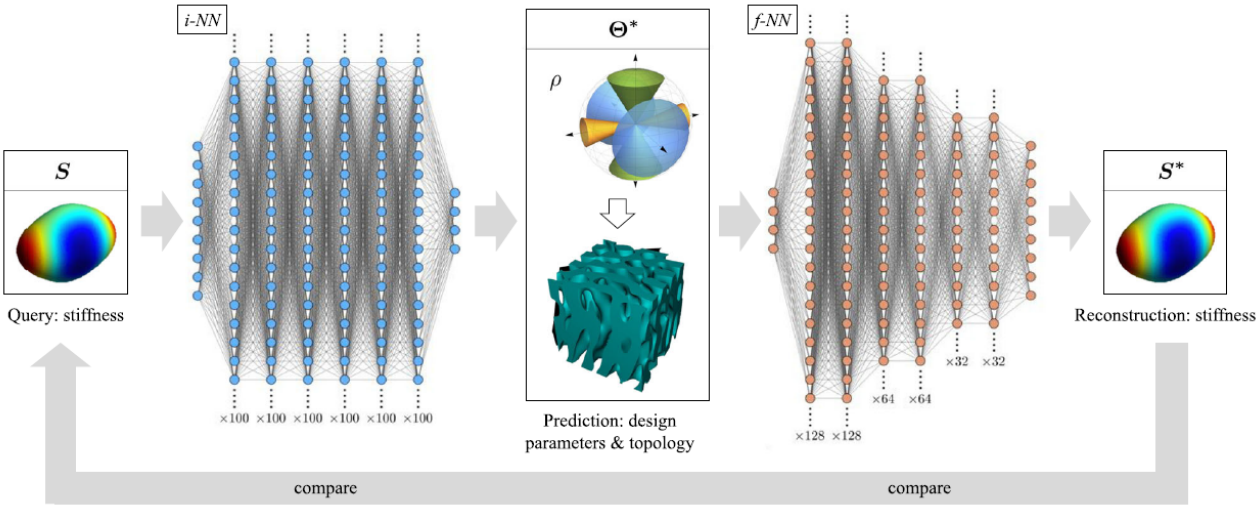

Figure 1.45: Schematic representation of the inverse design of anisotropic spinodoid microstructures. The inverse neural network (i-NN) takes stiffness (S) as input and produces design parameters Θ and ρ. The forward network (f-NN) takes the predicted parameters and calculates the expected stiffness. Image adapted from ref. [65].

- Self-supporting geometry
- The extrusion should be interrupted as little as possible
- Limited required acceleration rates for the printer head

The first condition is required because 3D printing is done in layers and an overhang would require the deposition of material "mid-air". The second condition is designed to limit the the number of small deposition defects caused by starting and stopping the extrusion process. The final condition follows from the observation that printer heads are generally relatively heavy and may be limited in their ability to quickly change velocity. Additionally, they have sought to find efficient ways to achieve global optimization by means of stochastic, a periodic structures [157]. The solution that has been suggested is to use foams based on Voronoi diagrams [157, 160]. Voronoi cells are created by taking a set of points on a domain, and assigning regions to each point based on a distance function [160, 161]. Figure 1.46 shows Voronoi diagrams of different distance functions for the same set of points.

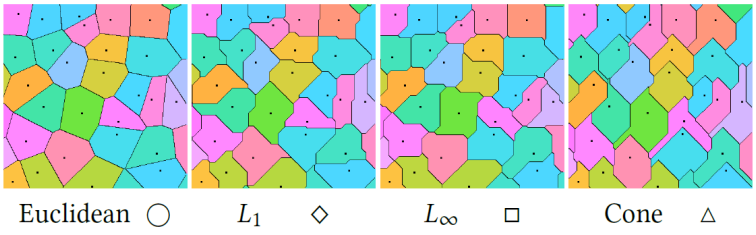

Figure 1.46: Voronoi diagrams based on different distance functions over the same set of points, image adapted from ref.[158].

Clearly, these structures suffer from overhang but the authors did note that every structure takes a fixed number of angles. It has been demonstrated that this is a general property of Voronoi cells based on polyhedral distance functions [160]. Martinez et al.[157, 158] demonstrated that by imposing conditions on local minima and wall angles, convex printable 3D structures could be designed and fabricated.

When applying the Voronoi method to 2D structures, the restrictions placed on the design become more relaxed, most notably those related to overhang. Martinez et al. in 2019 [159], investigated the potential of Voronoi diagrams based on star-shaped distance functions for 2D heterogeneous metamaterials. Star-shaped distance functions are parameterized through points with a specified distance from the center at equally spaced angles. The points are connected by polygonal or smooth interpolation, see figure 1.47a. To create a Voronoi diagram, the star-shaped distance definition is used. Consider a star-shaped set, $\mathcal{S}$, centered around point p and a random point p_i. The star-shaped distance $d_{\mathcal{S}}(p, p_i)$ is defined as the smallest factor by which $\mathcal{S}$ needs to be scaled so that p_i lies on its

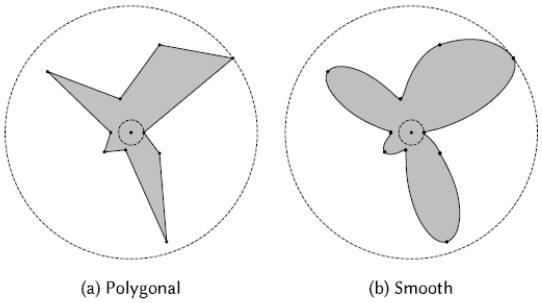

(a) Polygonal and smooth interpolation for the same parameterization of 10 equally spaced points.

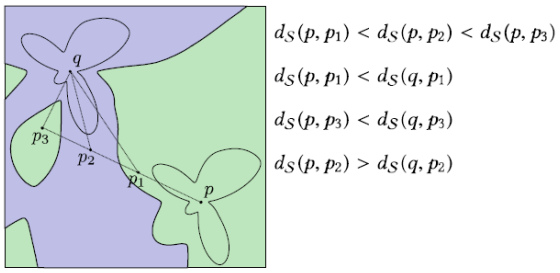

(b) The star-shaped metric does not guarantee connected microstructures by only considering star-shaped distance.

Figure 1.47: Paramaterization (a) and resulting Voronoi diagram (b) based on star-shaped metrics, images adapted from ref. [159].

boundary. Random points on the domain are assigned to the star-shaped centered points to which they have the lowest $d_{\mathcal{S}}$. Unfortunately, this does not always lead to connected cells, as demonstrated by figure 1.47b.

To solve this problem, the authors apply a growth model in which the initial structures grow incrementally using a global time parameter, as illustrated in figure 1.48a. This method can be enhanced by including a maximum growth radius to avoid potential degenerate cases, as demonstrated by figure 1.48b.

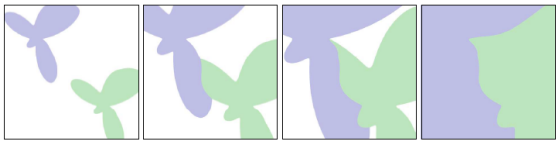

(a) Evolution from left to right of star-shaped cells following the growth model.

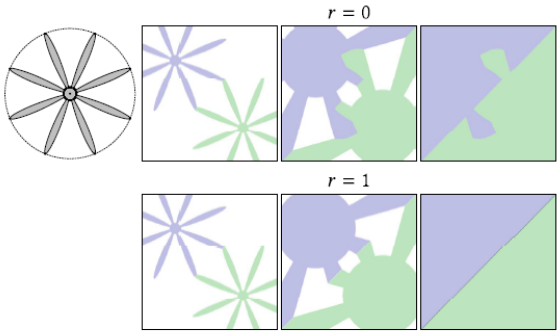

(b) Controlling undesired artefacts from unconstrained growth (r=0) by introducing a maximum growth radius (r=1).

Figure 1.48: Implementation of a growth based model leads to connected microstructures a and can be improved to suppress degeneracy by including a maximum growth criteria (right), images adapted from ref. [159].

A powerful property of this method is its ability to generate heterogeneous structures with connectivity. This can be done in a discrete manner, by assigning different shapes, $\mathcal{S}_1$ and $\mathcal{S}_2$, to different sites, or by a hard transition from one shape to another. It can also be done through a continuous metric interpolation between two sets,

$$\mathcal{S}(\beta) = \mathcal{S}_1\beta + \mathcal{S}_2(1-\beta) \tag{1.21}$$

where β takes values between 0 and 1 that can vary spatially. Examples of both the discrete and continuous method are shown in figure 1.49. It should be noted that in this approach, it is the star-shaped metric that is interpolated, not the microstructure.

The authors analyse a variety of lattices types and star-shaped metrics, and demonstrate that symmetries of the Voronoi diagrams will be preserved if they are matched with appropriate lattice types. This is also true when Voronoi diagrams with different metrics but similar symmetry are used. The paper studies in detail designs with with one-axis reflectional and three-fold rotational symmetry. It is found that the resulting properties are orthotropic and isotropic symmetry, which confirms results of earlier research [162, 163]. In studying the interpolation mechanism it is found that despite always achieving connectivity, the properties of the intermediate structures do not always show smooth transitions, as demonstrated by figure 1.50.

The authors conclude by stating that even though disconnected microstructures were not found in their study, it doesn't guarantee that this can never happen. Additionally, they point out that the method can naturally be extended to 3D structures and that research could be done on other interpolation functions.

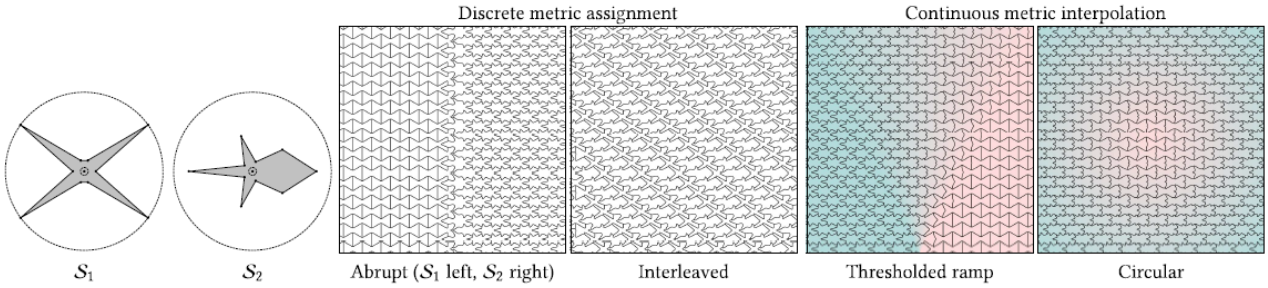

Figure 1.49: Discrete and continuous spatial variation of two different star-shaped metrics, $\mathcal{S}_1$ and $\mathcal{S}_2$, image adapted from ref.[158].

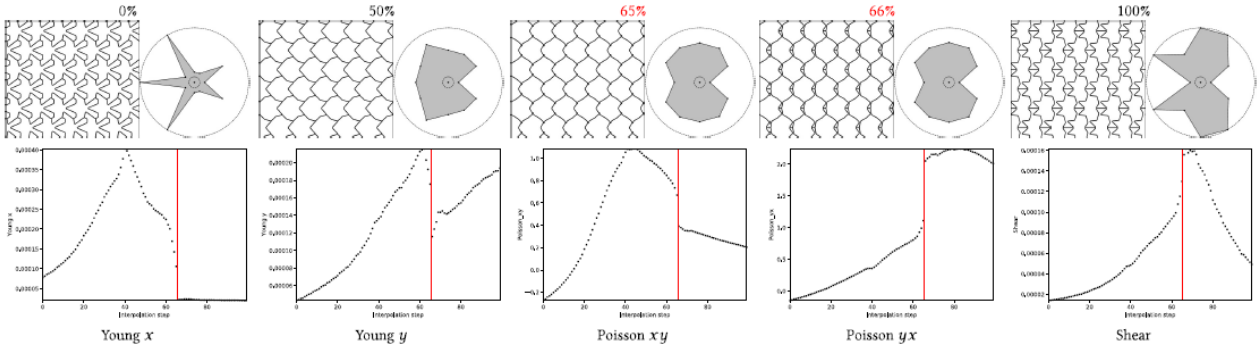

Figure 1.50: (Bottom layer) Mechanical properties as function of β according to equation 1.21 with discontinuous changes in properties (red lines). (Top layer) The associated microstructures for various values of degrees of interpolation, image adapted from ref.[158].

1.4 Recommendations

We have discussed theoretical models and design principles of metamaterials. In Section 1.2, theoretical limits and powerlaw theory were covered, followed by a discussion on auxetic and heterogeneous materials. Section 1.3 focused on design principles from truss based, to origami and kirigami and ended with foam based methods.
The theoretical limits that have been discussed follow from oversimplified models that are demonstrably unphysical. Nonetheless, to this day many researchers refer to them as relative measures for metamaterial performance. Therefore, these analytical models serve a very useful purpose in describing the limits to what can be achieved. However, to be truly useful in advancing the field, models should have predictive value beyond defining upper limits. To this end, more complex models may be required to give researchers tools to accurately design and predict new structures. Attempts at improved models have lead to increasingly complicated expressions, due to the need to capture complicated physics in as few as possible parameters. This seems to suggest that simple models will not suffice for this purpose. Intuitively, this can be expected since metamaterials can take vastly different designs with a variety of working principles that govern their behaviour. However, with powerful computers nowadays being widely available, FE models can be used to accurately predict behaviour without relying on simplified models. An advantage of FE models is that it makes use of mechanical and material models that represent physical reality. This means that if properly applied, insight can be gained into the physics behind the observed behaviour. This has been demonstrated to be an effective tool for predicting metamaterial behaviour. However, FE models become exceedingly expensive as microstructures grow more complex, even when homogenization theory is applied. A solution to this is provided by machine learning, which has been shown to provide an efficient alternative to expensive FE calculations. The benefits to computational cost can not be overstated, yet it should be noted that it comes at the cost of dismissing any insight in the physical process. This is not a real concern when it comes to property predictions of classes of metamaterial families which are well understood. But, over-reliance on black box methods could lead to a lack of understanding of underlying physics, if indiscriminately applied to a wide range of microstructures. It should be noted that there are no indications that this is currently the case, but as ML methods become more powerful this is something to keep in mind. Ultimately, lack of understanding of underlying mechanics will hamper progress in the long run. Scientists can reduce this risk by applying FE calculations to unexpected results, and by methodically comparing ML predictions to FE models.

Truss-based metamaterials have been demonstrated to be able to achieve high specific properties. However, sensitivity to imperfections tend to lead to lower than expected performance. An important topic of research would be to find methods to reduce sensitivity to fabrication errors. Ideally, this would lead to fundamental criteria that can guarantee reliable behaviour following geometric arguments. If this is not feasible, a solution could come in the form of tried and tested design principles that can serve as guidelines to produce optimal designs.
Due to the nature of truss-based metamaterials they are well suited for fractal designs. This can be especially useful in cases where expected loads are predictably directional. Starting from the concept of fractal designs, it could be interesting to investigate how various microstructures at various generations and spatial positions could lead to increased performance. The hierarchy of generations may also prove to be advantageous in terms of numerical optimization, because the different generations could be optimized sequentially. Additionally, truss based structures could be combined with deployment methods used in origami/kirigami structures (table 1.6). If truss based materials are designed with nodes that respond to external stimuli, it could lead to an interesting method to develop deployable truss based structures. This could be useful for space applications, since structural hierarchy can produce very light structures, albeit at the cost of increased volume. If deployment strategies can be implemented, so that unfolding can reliable happen after reaching orbit, the increased volume will no longer be an issue, while the decreased mass will reduce fuel costs for launch and orbit control.
Kirigami and Origami designs could also benefit from such developments, as it would open up the door to dynamically combine them with truss based structures. Kirigami and origami designs have long been used in space applications, like solar panels and the recently launched James Webb telescope, but their use in metamaterials has so far been limited. However, it has been demonstrated that in principle any shape can be made from a flat sheet. The problem with many metamaterials is that their complex designs make them difficult to fabricate. It could be interesting to research the potential to create complex structures that unfold from flat sheets. Sheet materials can be fabricated using high precision deposition techniques which provide maximum control over material distribution. Additionally, processing a flat sheet can be done fast and accurately using different techniques, including laser cutters. Perhaps an interesting goal would be to come up with two step methods in which; first a kirigami/origami design is deployed to form a 3D microstructure, followed by a second treatment step that fuses connecting parts together to form a 3D metamaterial. Another area that could benefit from kirigami/origami methods is that of flexible surfaces. Being able to control the topology of surfaces through the use of external stimuli means they can be used to create responsive surfaces. The fact they they would not rely on motors to move them would be a benefit. Research should then focus on maximizing service life and minimizing hysteresis in the joints.
Spinodoid methods have shown remarkable results, and their combination with inverse modelling provides a powerful tool to design both homogeneous and heterogeneous materials. As has been pointed out, this could proof to be very useful for designing bone implants. This has been successfully been demonstrated, but an it would be interesting to test this hypothesis on a large scale. For starters, one could start by replicating animal bones from livestock, as they are likely to be more readily available than human bones. It would be necessary to come up with a wide range of load cases to test the response to loads of different magnitude, direction and type. This course of research would require the production of numerically optimized designs. This on its own could also be a topic of interest. Since spinodal decomposition is a natural process, it is conceivable that spinodoid designs can be produced simply by allowing this process to take place and halting it at the right time. However, this requires two phase materials that can undergo the desired transformation, while having the desired material properties after separation. That this can be achieved is not a given, since spinodoid designs are not necessarily generated with real materials in mind. Research could aim to find materials where the final properties can be tuned over a wide range, while still performing spinodal decomposition. Additionally, it should be possible to manipulate the final microstructure by varying external parameters like temperature and pressure. Materials found that meet this requirements can be provided to the ML algorithm to be taken into account during the optimization procedure. Finally, spinodoid methods have been demonstrated to be able to generate connected anisotropic microstructures. This means key areas can be optimized first and intermediate regions can be connected in an interpolation step. It would be worth investigating the mechanical properties of the intermediate structures and if they show the same discontinuities as observed in the star-shaped materials.
The star-shaped method itself also offers a wide range of research directions. One of which could be to focus on the properties of intermediate structures. It is undesirable to have discontinuous properties and perhaps it is possible to condition the optimization in a way that this does not happen. Perhaps the star-shaped design space is filled with overlapping microstructures, meaning that similar properties can be achieved by many different metrics. This would greatly help to reduce potential discontinuity issues. It would be possible to try different combinations of structures, with the same effective properties, until a continuous intermediate region is found. Another way to potentially overcome such issues, could come from using different interpolation methods. It would be interesting to see how properties of the intermediate structures are affected by the choice of interpolation method. Another topic of research could be anisotropic designs. By placing no constraint on the location of lattice sites, a multitude of

anisotropic topologies can be generated. It is worth investigating how this would effect connectivity of different sites. Both for single star-shape metrics, and for combinations of two metrics. Additionally, it would be interesting to study the effect of combining more than two metrics. This could be investigated on both periodic, and non-periodic lattices. This could open the door for a versatile method to generate spatially varying anisotropic microstructures. The ultimate short-term goal would be to generate anisotropic microstrctures with tunable properties over a random domain. 2D microsctructures could also be fabricated using 3D printing methods to test numerical predictions to experimental results. Additionally, as has been pointed out earlier, this method should allow for application to 3D domains and it would be interesting to do research in this direction. Initial research might focus on determining microstructure and property relations while later research could look for conditions to allow fabrication with selected techniques.

Figure 2.1: Examples of microstructures produced by the Voronoi diagram growth-based method. Black pixels represent material and white pixels represent void.

2 Growth-based Voronoi metamaterials

In engineering, materials are typically selected to meet design requirements. Properties of materials can be tuned by changing bulk properties. For example, by changing the composition of alloying elements in steel. However, the design space is limited and might involve the use of expensive elements. On the other hand, metamaterials can be used to explore large design space, often using cheap and widely available materials. The main challenge is to design metamaterials that match desired properties, thus allowing for case specific designs with optimal properties. Taking inspiration from work done on the application of inverse modelling to spinodoid designs, we investigate how this method can be applied to 2D star-shaped Voronoi growth based methods, figure 2.1 [159]. This has the potential of opening up a large design space while using simple parameterization, making it an ideal candidate for machine learning. The inverse problem, where design parameters are predicted to meet stiffness requirements, is an inherently ill-posed problem because there are multiple designs that can lead to the same stiffness. To overcome this problem we make use of two neural networks, a forward and an inverse network, inspired by the work done on spinodoids by Kumar et al. [65]. The forward neural network (f-NN) predicts properties based on design parameters, while the inverse neural network (i-NN) predicts design parameters based on target properties. The combination of two networks renders the inverse problem well-posed, and allows training of the neural network to produce accurate results.

This requires a database that contains parameterized data on microstructures and associated properties. To this end, a database of growth based unit cells is produced, and a fast Fourier transformation homogenization method is used to determine their stiffness properties. The design parameters and homogenized stiffness components form the main data points for the neural networks.

The Voronoi based method is discussed in Section 2.1, this includes a discussion on the input parameters and how these affect the final microstructure. The stiffness matrix and methods to visualise their associated behaviour is discussed in Section 3. This is followed by a discussion on homogenization in Section 3.3, this includes a convergence study on the resolution of input data. In Section 5 the procedure and infrastructure to generate datasets is treated while also investigating the possible design space. Section 6 covers the training and validation of the forward networks, where special attention is given to the physical feasibility of the predictions. The inverse network is treated in Section 7 and in Section 8 the model is extended to produce multiple designs. Finally, tensile tests on 3D printed samples are compared FE calculations in Section 9 followed by a discussion in Section 10.

2.1 Growth based Voronoi diagrams with Star-shaped metrics

To design 2D metamaterials it is necessary to divide a spatial domain into material regions and voids. Designs should be tileable (boundary compatible) in order to fill arbitrarily sized domains. Additionally, from a fabrication perspective it is necessary that all material regions are interconnected. These constraints are naturally satisfied by growth based Voronoi diagrams with star-shaped metrics. This chapter starts with a treatment of star-shaped metrics, followed by a description of the Voronoi diagrams and growth-based method.

2.2 Star-shaped metrics

Let $\mathcal{S}$ be a star-shape centered on $\mathcal{O}$, with a and b the minimal and maximal radial span, as seen in figure 2.2a. To understand the process of constructing Voronoi diagrams the concept of star-shape distance is used, $d_{\mathcal{S}}$. Let

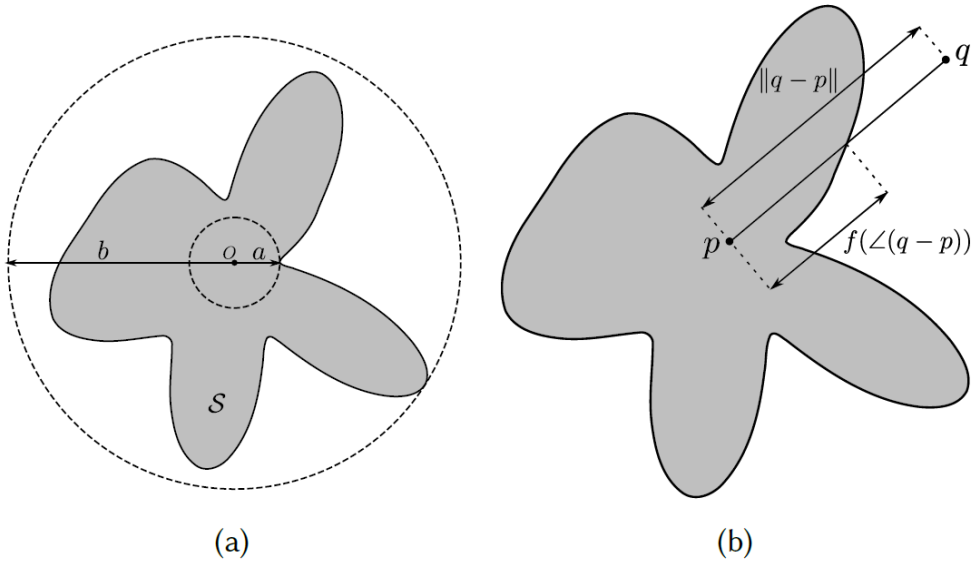

Figure 2.2: Visualization of star-shape metrics. (a) Star-shape $\mathcal{S}$ centered on $\mathcal{O}$ with minimal (a) and maximum (b) radial spans. (b) Star shape distance $d_{\mathcal{S}}(p,q)$ defined in terms of the Euclidean norm $\|q-p\|$ and $f(\angle(q-p))$, image adapted from ref.[159].

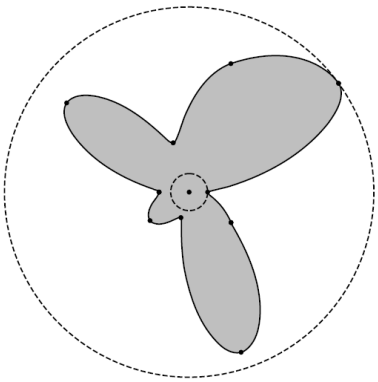

Figure 2.3: Parameterization of a star-shape with ten prescribed radial spans and a smooth interpolation function, image adapted from ref.[159].

star-shape $\mathcal{S}$ be centered on point p, while point q lies outside $\mathcal{S}$, figure 2.2b. The star-shape distance between points p and q, $d_{\mathcal{S}}(p,q)$, is then defined as

$$d_{\mathcal{S}}(p,q) = \frac{\|q-p\|}{f(\angle(q-p))}, \tag{2.1}$$

where $\|q-p\|$ is the Euclidean norm of p and q, and $f(\angle(q-p))$ represents the distance from p to the edge of $\mathcal{S}$ in the direction of q [160]. It can be interpreted as a measure that describes how much star-shape $\mathcal{S}$ must grow, such that point q lies on its boundary. In section 2.3, the star-shape distance is used for the construction of Voronoi diagrams.

In theory any arbitrary shape that obeys the the limits given by a and b in figure 2.2a, could be used as a legitimate star-shape. However, for the purpose machine learning it is desirable to limit the number of input parameters. Therefore, star-shapes will be parameterized through radial spans at equally spaced angles. For each span the distance from the center of the star is defined by a random number between 0.01 and 1. A smooth interpolation function is used to connect the prescribed spans to form a star-shape. Figure 2.3 shows an example where ten spans are prescribed. Please note that the number of prescribed spans can be chosen freely.

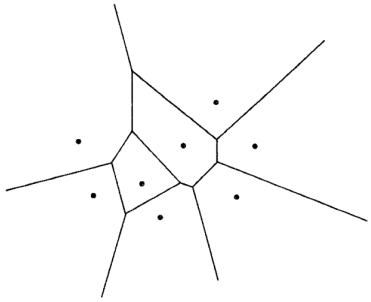

Figure 2.4: A Voronoi diagram constructed using the euclidean distance between eight points. Regions are assigned to the point to which they have the shortest euclidean distance, image adapted from ref.[164].

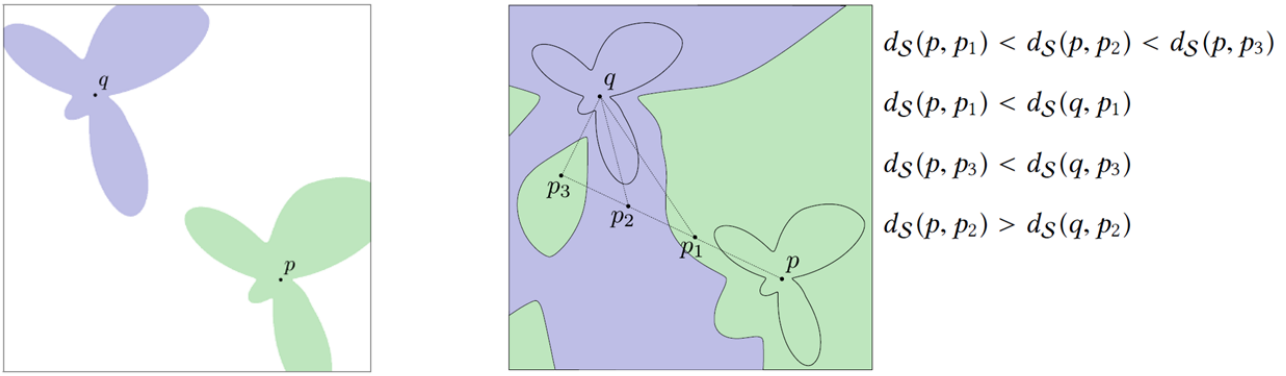

Figure 2.5: (a) A plane containing two star shapes centered on points p and q, which forms the basis of a stars-shape induced Voronoi diagram. (b) The star-shape induced Voronoi diagram produces an island of domain p surrounded by an area of domain q, this is explained by the inequalities on the right. Images adapted from ref.[159].

2.3 Voronoi diagrams and growth-based cells

Voronoi diagrams use a nearest neighbour approach to assign domains to different points on a plane [164]. Consider a plane that contains eight points, figure 2.4. The Voronoi diagram can be constructed by associating each point with the region closest to it.

Instead of using euclidean distances, Voronoi diagrams can also be constructed using star-shape distances. Consider a plane containing two points, p and q, that each have a star-shape centered on them, figure 2.5a. To construct the Voronoi diagram we assign each point in the plane to domain p or q, based on their star-shape distance. A point x, anywhere on the plane, will be assigned to domain p if $d_{\mathcal{S}}(p, x) < d_{\mathcal{S}}(q, x)$, and to q if $d_{\mathcal{S}}(q, x) < d_{\mathcal{S}}(p, x)$. This leads to the formation of cells that have non-trivial shapes and that divide the plane in regions belonging to either p or q. However, these Voronoi cells are not guaranteed to have connected components, as illustrated by figure 2.5b. The star-shape distance from p_2 to q ($d_{\mathcal{S}}(q, p_2)$) is smaller than the star-shape distance from p_2 to p ($d_{\mathcal{S}}(p, p_2)$), so p_2 is assigned to region q. The opposite is true for point p_3, which leads to the formation of an island of domain p inside a region of domain q. The inequalities on the right of figure 2.5b provide a more detailed analysis.

The formation of islands is an undesirable feature for metamaterial topology because it may lead to problems during fabrication. To remedy this, a flood-fill growth algorithm, based on star-shape metrics, is proposed [165]. The algorithm divides the domain in a grid of pixels and grows star-shapes to fill the entire plane. This leads to microstructures without disconnected islands, as visualised in figure 2.6.

The growth algorithm uses a maximum growth distance, r, to stop a growth front from expanding when it detects a filled cell in the growth direction within the set distance. This leads to the formation of walls at the interface between two growth fronts, represented by the black pixels in figure 2.7. This example shows a constant value for r, but a spatially varying r can be described through a parameterization similar to that of the star-shapes, figure 2.3. Max growth values are prescribed for each radial span distance that defines a given star-shape. Similarly, these points are connected through a smooth interpolation function, visualized by the "Max growth" plot in figure 2.8. As a result, the set of inputs that uniquely describe a given microstructure are defined by a set of radial span distances, plus an equal number of max growth values.

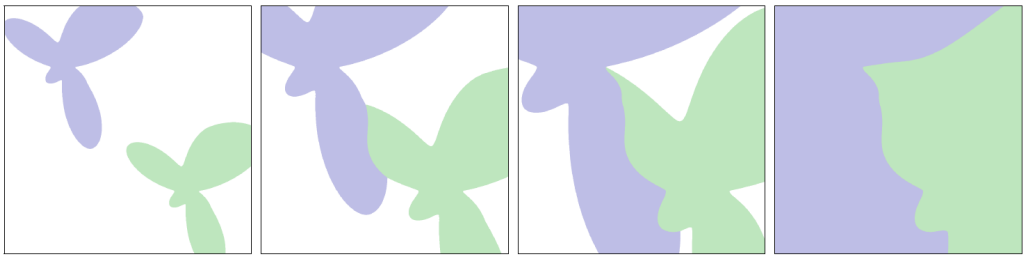

Figure 2.6: Visualisation of the growth-based algorithm evolution from left to right. The result is two fully connected domains. Image adapted from ref.[159].

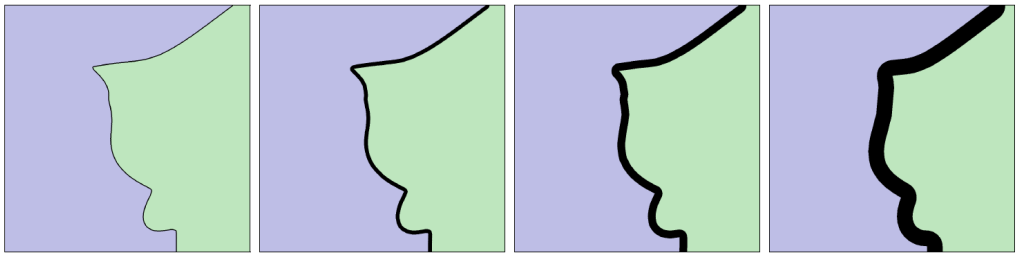

Figure 2.7: The effect of growth limiting parameter, r, on the wall thickness between two growth fronts, image adapted from ref.[159].

2.4 Unit cell generation

The algorithm from Martinez et al. [159] is used to grow microstructures based on Voronoi diagrams induced by star-shape designs. Structures are grown on a square domain, with periodic boundary conditions, and a single lattice point at its center. To obtain a unit cell, a set of radial spans and maximum growth parameters is provided as input to the growth algorithm. When the growth process is finished, the walls are considered to be solid material while the rest of the domain is considered to be void. An example of the input parameters, and resulting microstructure, is given in figure 2.8. The star-shape is used as initial shape for the growth algorithm, while the max growth determines when a growth front stops growing, the latter effectively determines wall thickness. In figure 2.8 seven radial spans and growth parameters were used to prescribe the plotted inputs.

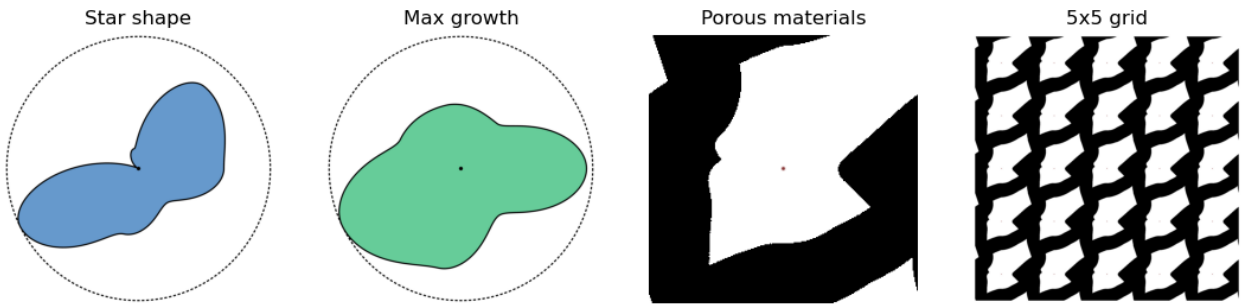

Figure 2.8: A visual representation of the input parameters for the star-shape and max growth parameters, the resulting microstructure (porous material) and a 5x5 tessellation of the unit cell. Black and white pixels represent solid material and void, respectively.

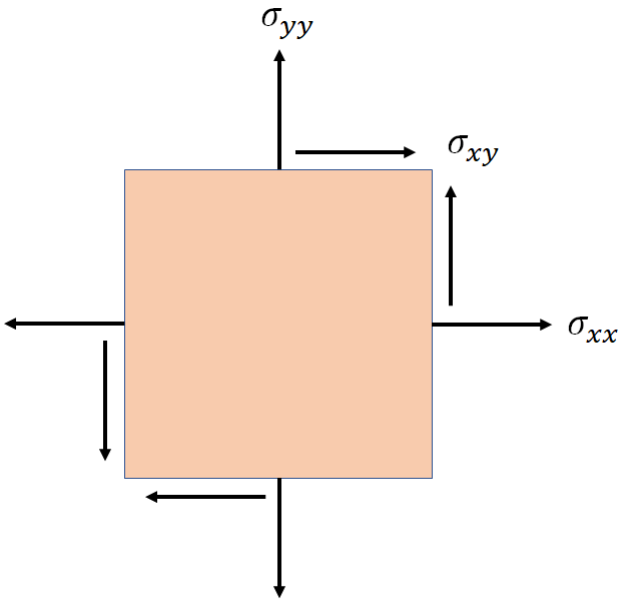

Figure 3.1: Under plane stress conditions the relevant stress components are the two normal components (σ_x and σ_y) and one shear component (σ_{xy}).

3 Homogenization of growth-based Voronoi metamaterials

3.1 Effective stiffness matrix

The stiffness tensor describes the stress ($\boldsymbol{\sigma}$) response of a material given a strain state (ε),

$$\boldsymbol{\sigma} = \mathbb{C}\boldsymbol{\varepsilon}, \tag{3.1}$$

where $\mathbb{C}$ represents the stiffness tensor. The stiffness follows from the generalized Hooke's law and takes the form of a fourth-rank tensor with 81 components. This tensor can be expressed in matrix form ($\boldsymbol{C}$) through the Voigt notation [166]. For 3D materials this matrix contains 21 independent components. However, in the case of plane stress the only relevant stresses and strains are those within the plane, figure 3.1. As a result, 3.1 in Voigt notation takes the form of

$$\begin{bmatrix}\sigma_{11}\\ \sigma_{22}\\ \sigma_{12}\end{bmatrix} = \begin{bmatrix}C_{11} & C_{12} & C_{13}\\ C_{21} & C_{22} & C_{23}\\ C_{31} & C_{32} & C_{33}\end{bmatrix}\begin{bmatrix}\varepsilon_{11}\\ \varepsilon_{22}\\ \varepsilon_{12}\end{bmatrix}, \tag{3.2}$$

where due to symmetry, $C_{12} = C_{21}$, $C_{13} = C_{31}$ and $C_{23} = C_{32}$. Therefore, the stiffness matrix is uniquely defined by the six independent components in the upper right (or lower left) triangle of matrix $\boldsymbol{C}$.

3.2 Young's modulus, Poisson's ratio and shear modulus

For isotropic linear elastic materials, the stiffness matrix is determined by two independent constants, Young's Modulus (E) and Poisson's ratio (ν),

$$\boldsymbol{C}(E,\nu) = \frac{E}{(1+\nu)(1-2\nu)}\begin{bmatrix}1-\nu & \nu & 0\\ \nu & 1-\nu & 0\\ 0 & 0 & 1-2\nu\end{bmatrix}, \tag{3.3}$$

with shear modulus

$$G = \frac{E}{2(1+\nu)}. \tag{3.4}$$

However, for anisotropic materials these quantities are directional and will vary depending on loading direction and/or contraction or shear direction [167]. To analyze anisotropic unit cells, these three quantities can be plotted on a polar diagram as function of loading direction [168]. This requires the use of compliance ($\boldsymbol{S}$), which describes the (engineering) strain response of material under a prescribed stress field

$$\varepsilon = \boldsymbol{S}\boldsymbol{\sigma}, \tag{3.5}$$

Table 3.1: Voigt scheme for converting matrix to tensor notation.

Matrix index (m, n)	1	2	3
Tensor index (ij, kl)	11	22	12, 21

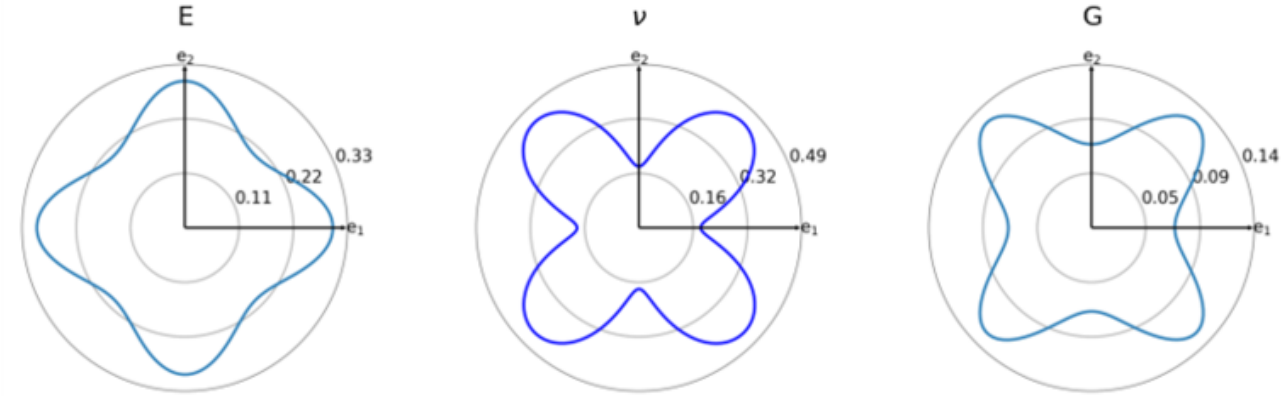

Figure 3.2: Visualization of Young's modulus (E), Poisson's ratio (ν) and shear modulus (G) as function of direction.

and is equal to the inverse of the stiffness matrix, $\boldsymbol{S} = \boldsymbol{C}^{-1}$. The compliance matrix is converted to a fourth-rank tensor (S_{ijkl}). Consider the compliance matrix in Voigt notation

$$S_{mn} = \begin{bmatrix} S_{11} & S_{12} & S_{13} \\ S_{21} & S_{22} & S_{23} \\ S_{31} & S_{32} & S_{33} \end{bmatrix}, \tag{3.6}$$

where m and n denote matrix indices. To convert 3.6 to a fourth-rank tensor of the form S_{ijkl}, the Voigt scheme in table 3.1 is used to map the matrix indices to tensor indices. The fourth-rank compliance tensor can then be constructed through

$$\begin{aligned} S_{ijkl} &= S_{mn}, && \text{when } m \text{ and } n \text{ are } 1 \text{ or } 2, \\ S_{ijkl} &= \tfrac{1}{2} S_{mn}, && \text{when either } m \text{ or } n \text{ is } 3, \\ S_{ijkl} &= \tfrac{1}{4} S_{mn}, && \text{when both } m \text{ and } n \text{ are } 3. \end{aligned} \tag{3.7}$$

To determine E, ν and G, a loading direction ($\vec{d}$) needs to be defined. Additionally, for ν and G it is necessary to define a shear/contraction direction ($\vec{n}$). In principle, $\vec{n}$ can be chosen arbitrarily but in this thesis it is set to be perpendicular to $\vec{d}$,

$$\begin{aligned} \vec{d} &= (\cos\theta, \sin\theta)^{\mathrm{T}}, \\ \vec{n} &= (-\sin\theta, \cos\theta)^{\mathrm{T}}. \end{aligned} \qquad 0 \leq \theta \leq 2\pi \tag{3.8}$$

With these definitions, and using the Einstein notation, we get

$$\begin{aligned} E(\vec{d}) &= \frac{1}{S_{ijkl} d_i d_j d_k d_l}, \\ G(\vec{d}, \vec{n}) &= \frac{1}{4} \frac{1}{S_{ijkl} d_i n_j d_k n_l}, \\ \nu(\vec{d}, \vec{n}) &= \frac{S_{ijkl} d_i d_j n_k n_l}{S_{ijkl} d_i d_j d_k d_l}. \end{aligned} \tag{3.9}$$

By sampling θ, polar plots of the properties can be obtained to visualize the directional behaviour of a unit cell, an example of which is plotted in 3.2. The Young's modulus plot shows the modulus that would be found if the material was loaded in a specific direction, with maxima at 0, $\frac{1}{2}\pi$, π and $\frac{3}{2}\pi$, and minima at $\frac{1}{4}\pi$, $\frac{3}{4}\pi$, $\frac{5}{4}\pi$ and $\frac{7}{4}\pi$. The plots of ν and G show the contraction/shear behaviour, respectively, perpendicular to the loading direction as function of the loading direction. For example, if the material in figure 3.2 is loaded in $\vec{e_1}$ direction, the values of ν and G on the $\vec{e_1}$ axis corresponds to the contraction/shear perpendicular to the $\vec{e_1}$ direction.

3.3 Homogenization methodology

After generating a unit cell, homogenization is used to determine its stiffness properties. The constituent material is modelled to be isotropic linear elastic. However, growth based microstructures consist of a combination of voids and

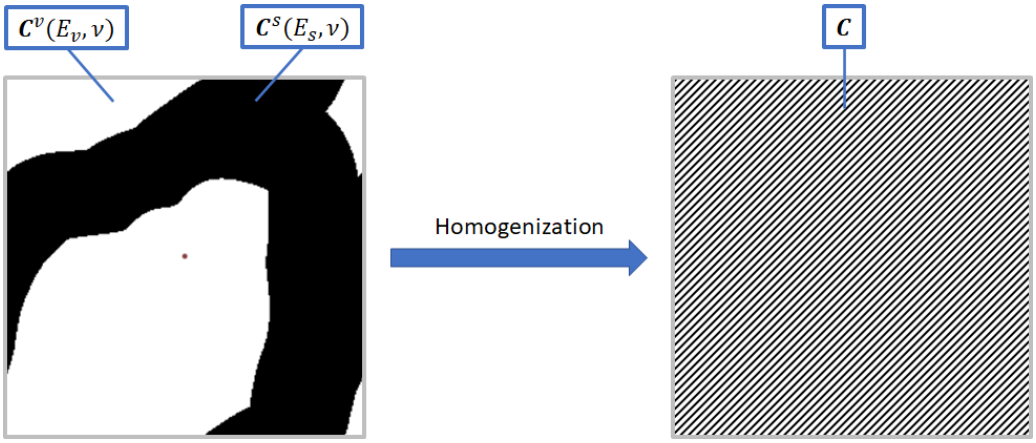

Figure 3.3: Using homogenization a growth based unit cell (left) can be represented by a RVE with the same properties (right).

material, which results in unit cells with anisotropic properties. The purpose of homogenization is to replace complex microstructure by a representative volume element (RVE) of continuum material, figure 3.3. The material properties of a RVE are described by an anisotropic stiffness tensor that behaves the same way as the complex microstructure of the original unit cell.

The solid material of a unit cell is considered to be isotropic and is assigned a Young's modulus $E_s = 1$ and Poisson's ratio $\nu_s = 0.3$. For computational stability, the void pixels are given the same Poisson's ratio and a Young's modulus of $E_v = 10^{-6}$. The homogenization procedure is based on Fast Fourier Transform (FFT) homogenization [169]. It considers the strain field ε to be a function of the displacement field $\boldsymbol{u}(x, y)$. By applying periodic boundary conditions, the local strain field $\varepsilon(\boldsymbol{u}(x, y))$ can be divided in two parts: the average strain $\boldsymbol{E}$ and local fluctuations $\varepsilon(\boldsymbol{u}^*(x, y))$,

$$\varepsilon(\boldsymbol{u}(x, y)) = \varepsilon(\boldsymbol{u}^*(x, y)) + \boldsymbol{E}. \tag{3.10}$$

Under the assumption of periodic boundary conditions, the fluctuations $\boldsymbol{u}^*(x, y)$ will be periodic as well. Additionally, it implies anti-periodic traction on the cell edges to satisfy equilibrium conditions. By prescribing a strain $\boldsymbol{E}$, the stress response of the material can be calculated and the homogenized stiffness tensor be determined. Because of the assumption of periodicity, the problem can be converted to Fourier space using FFT, which significantly improves performance [170]. Finally, the method requires inputs in the form of discretized images consisting of pixels, which means the growth based unit cells can directly be used.

3.4 Convergence study

The homogenization procedure is computationally the most expensive operation and is related to the size of the input image. To limit computing time, a convergence study is done to determine the optimal image size. Such that an input image can be as small as possible, without leading to significant losses in accuracy.

To arrive at an optimal size for input images of the homogenization process, two methods are considered, figure 3.4. The first is to find the optimal image size at which to grow the microstructures directly. The second method is to grow the microstructure on a large grid (256×256), and to resize it to a lower resolution in a post processing step. To test the first method, the output of the growth process is changed step-wise, from 16×16 to 256×256, in increments of 16×16. For the second method, the image size of the growth process output is fixed at 256×256, and the output is subsequently resized to the match the resolutions of the first method. The reasoning behind the second method is that output of the growth-process is influenced by grid resolution, figure 3.5. At low resolutions, this can lead to coarse features which can effect the homogenized properties. This effect can be observed when comparing the density and C_{11} of a unit cell at different resolutions, figure 3.6. The plots shows how density and stiffness are a function of the resolution at which the material is grown (original), leading to lower densities at lower resolutions. Results on resized images are less sensitive to changes in resolution.

The second method could lead to convergence at a lower resolution, compared to growing the unit cells directly at that resolution. To compare the convergence of multiple microstructures, the convergence error is calculated according to

$$\text{Convergence\_error} = \frac{{C_{ij}}^{n-1} - {C_{ij}}^{n}}{{C_{ij}}^{n}}, \qquad i, j = 1, 2, 3 \quad \text{and} \quad n = 16, 32, ..., 256 \tag{3.11}$$

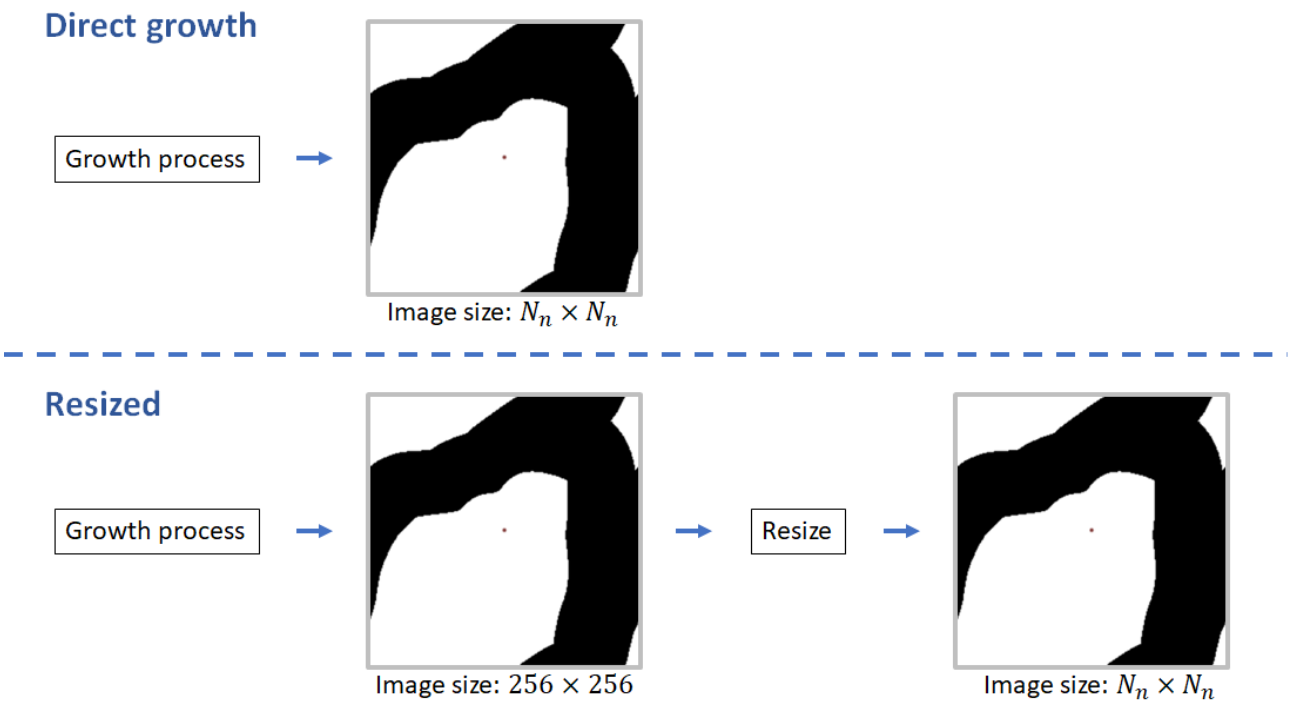

Figure 3.4: Two methods for producing input images for the homogenization process, where $N_n = 16, 32, 48, ..., 256$. (top) The direct growth method where the output of the growth process is changed to produce images of the desired resolution. (bottom) The output of the growth process is fixed at 256×256 and images are subsequently resized to the desired resolution.

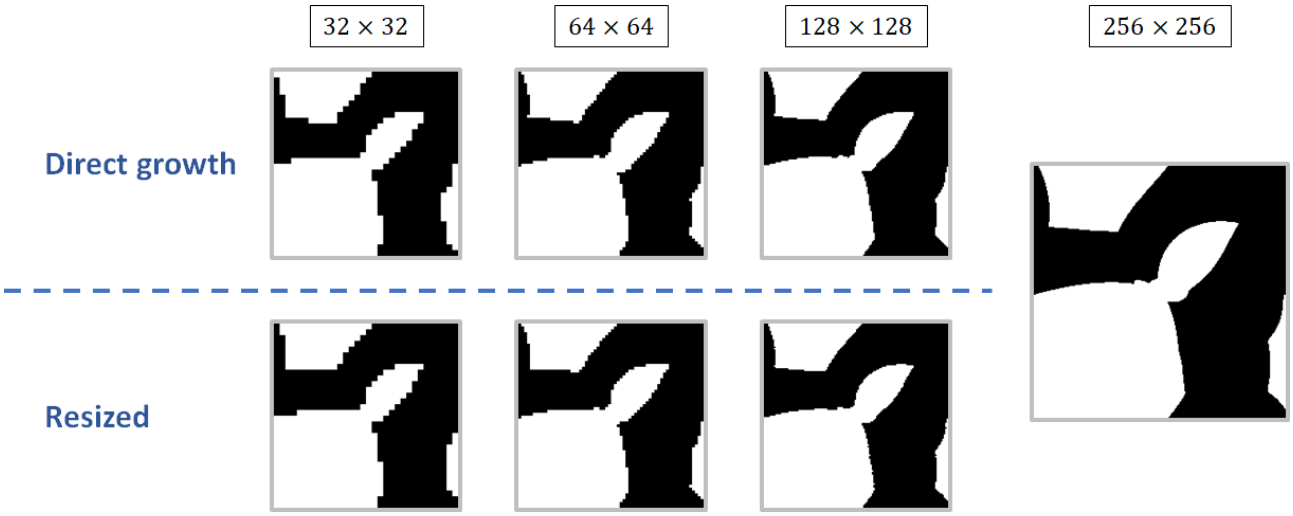

Figure 3.5: Unit cell topology at different image sizes, using the same set of design parameters. (Top) Unit cells grown directly on different image sizes. (Bottom) Unit cells that are resized versions of the 256×256 image.

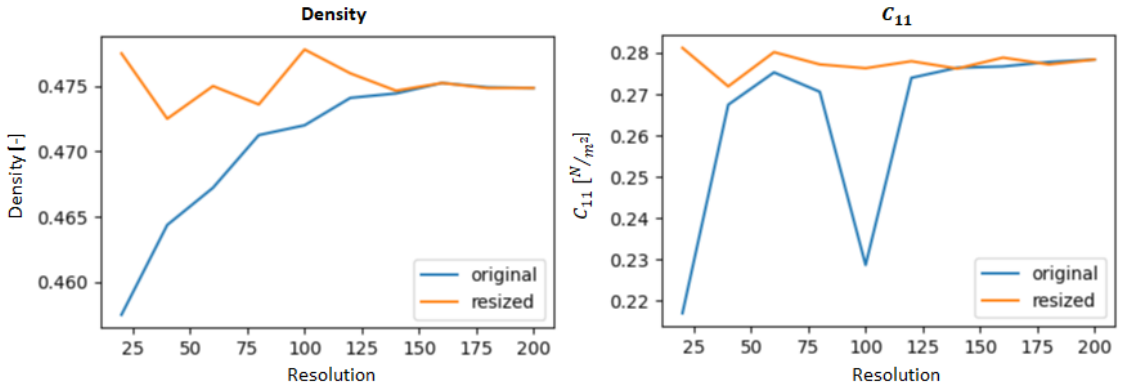

Figure 3.6: Change in density (left) and C_{11} (right) of porous material grown at different resolutions vs material grown at 256×256 and subsequently resized in a post-processing step. The resized images show more consistent density and stiffness across different image sizes.

where i, j represent matrix indices of the stiffness matrix and n the resolution. The result is a dimensionless quantity which represents the relative change in a stiffness component, due to an incremental increase in image size. One-hundred of the same samples are repeatedly generated for each image size increment and 3.11 used to determine the mean, and standard deviation of the six stiffness components, figure 3.7. Only C_{11} and C_{12} are shown, as they are representative of the behaviour of the other components. The results indicate that the mean error of the resize method is generally lower than that of the growth based approach. Additionally, this resize method produces consistently lower standard deviations, which indicates results are more consistent. Therefore, the method selected for this thesis will be the resizing method at 128×128 pixels. Thus, microstructures will be grown at 256×256 and resized to 128×128.

4 Neural Network Training

When analyzing data, be it artificially generated or obtained through experiments, it is often desirable to fit a model to the observations. A model can be used to make predictions about data that has not been directly observed or to extrapolate data beyond the measured domain. Additionally, a model could give insight in underlying mechanisms of the observed system.

4.1 Regression

The type of data that we are interested consists of feature vectors $\boldsymbol{X} = (\boldsymbol{X}_1, \boldsymbol{X}_2, ..., \boldsymbol{X}_N)$ and associated target vectors ($\boldsymbol{y}$). Models are designed to map input data ($\boldsymbol{X}$) to output ($\hat{\boldsymbol{y}}$). In the case that the model output consists of one or more continuous variables, the process of fitting data to the model is called regression. In classical approaches, regression requires a pre-defined model to fit the data to. In the case of 1D polynomial regression, this model takes the form of

$$\hat{y}(X, \boldsymbol{w}) = w_0 + w_1 X + w_2 X^2 + ... + w_M X^M, \tag{4.1}$$

where M represents the power of the polynomial and $\boldsymbol{w} = (w_0, w_1, ..., w_M)$ a vector of weight factors. Training this model means finding $\boldsymbol{w}$, such that predictions most accurately match the targets. This can be done by minimizing a loss function, which in this case takes the form of

$$E(\boldsymbol{w}) = \sum_{n=1}^{N} |\hat{y}(X_n, \boldsymbol{w}) - y_n|, \tag{4.2}$$

which is the sum of the absolute differences between prediction and target. Minimizing 4.2 means minimizing the difference between output $\hat{\boldsymbol{y}}$ and target vectors $\boldsymbol{y}$. The absolute value is used to make sure the difference between $\hat{y}_n$ and y_n is always positive. The plot in figure 4.1 shows how the loss function would be zero if the predictions perfectly match the targets. This method can produce accurate models, but it relies on an good a priori decision about the form of the model, i.e. the power of the polynomial.

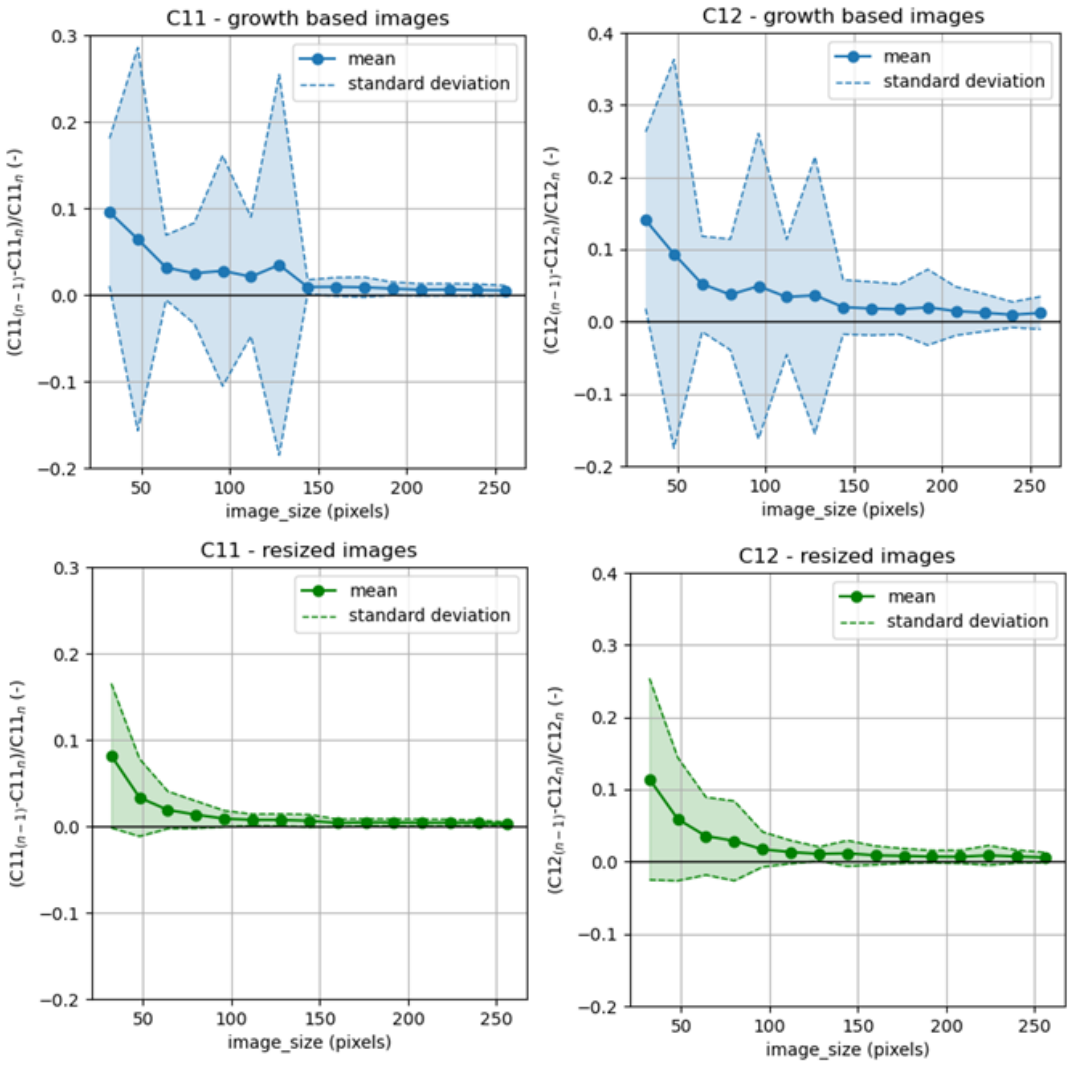

Figure 3.7: Convergence of two stiffness components, C_{11} (left) and C_{12} (right), using method 1 (top) and method 2 (bottom), using one-hundred samples.

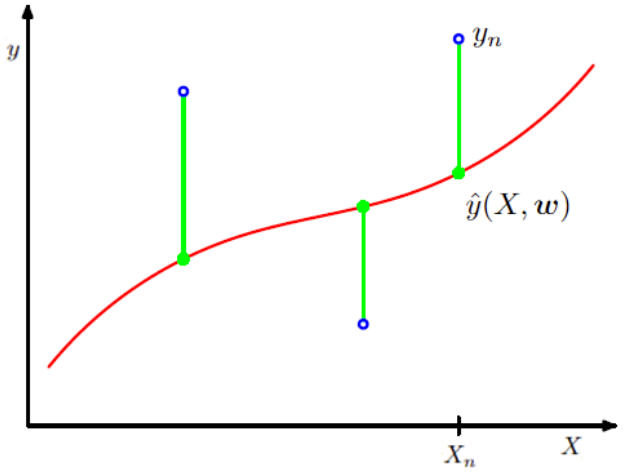

Figure 4.1: The continuous model prediction $\hat{y}$ of a regression model and the target values $\boldsymbol{y}$. Figure adapted from ref. [171].

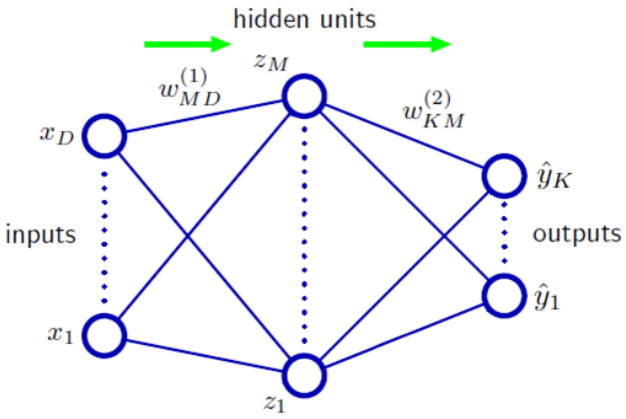

Figure 4.2: A graphical representation of neural networks. A series of linear functional transformations are applied to input x to produce output y. Figure adapted from ref. [171].

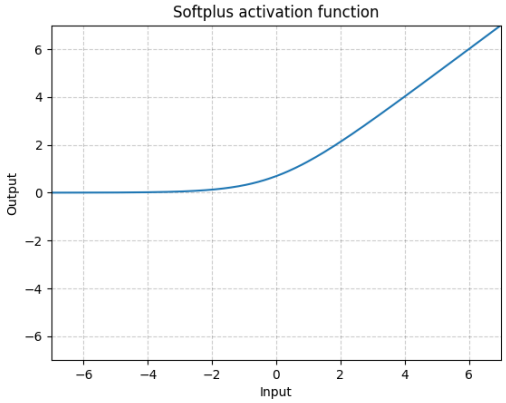

Figure 4.3: A plot of the softplus activation function which transforms any input to a 0 or positive output.

4.2 Forward propagation

Artificial neural networks, or simply neural networks, offer an advantage over traditional regression methods in that they do not require a prior assumption about the model. This is achieved by applying a series of functional transformations to an input to produce an output. The data flow and operations can be schematically represented as a network which somewhat resembles natural neural networks, figure 4.2. To understand how information passes through the network, consider the units in the hidden layer $z_1, ..., z_M$. The inputs of these node, also called activations, $a_1, ..., a_M$, are the sums of all the input parameters, $x_1, ..., x_D$, multiplied by their respective weight factors

$$a_j = \sum_{i=1}^{D} {w_{ji}}^{(1)} x_i, \tag{4.3}$$

where $j = 1, ..., M$, corresponding to the number of hidden units and the subscript (1) indicates that these weights are associated with the first layer. In the hidden units, the activations are transformed using a differentiable function, also called the activation function. An example of which is the softplus activation function

$$h(x) = \log(1 + e^x), \tag{4.4}$$

which transforms any input to a 0 or positive value, figure 4.3. In theory, any differentiable function can be used, and various activation functions can be assigned to various units. However, in this thesis the same activation function is applied to every unit. The outputs of the hidden layer are

$$z_j = h(a_j), \tag{4.5}$$

where $h(.)$ represents the activation function. This procedure is repeated in the second layer, where the activations are calculated using the outputs of the hidden layers,

$$a_k = \sum_{i=1}^{M} {w_{kj}}^{(2)} z_j, \tag{4.6}$$

with the subscript now indicating that these weights are in the second hidden layer. Finally, activation functions are used to transform the activations to outputs $\hat{y}_1, ..., \hat{y}_K$,

$$\hat{y}_k = h(a_k). \tag{4.7}$$

This example has only one hidden layer, but in principle the process of taking weighted sums of outputs, and transforming them with an activation function, can be repeated indefinitely. The process of calculating and transforming the activations for successive layers is called forward propagation, referring to the direction of the flow of information.

4.3 Backward propagation

In the case that the same activation function is applied to every unit, the optimization of the network in figure 4.2 means finding the optimal values for the weights. If a dataset with N datapoints exists, the loss function to minimize is the sum of the errors for each datapoint,

$$E(\boldsymbol{w}) = \sum_{n=1}^{N} E_n(\boldsymbol{w}). \tag{4.8}$$

To find the optimal weights a gradient descent optimization process can be applied to iteratively update the weights. This method uses the derivative of the loss function with respect to the weights to update the network. To update the weights from iteration τ to iteration $\tau + 1$ the weights are updated according to

$$\boldsymbol{w}^{\tau+1} = \boldsymbol{w}^{\tau} - \eta \nabla E(\boldsymbol{w}^{\tau}), \tag{4.9}$$

where the factor η is the learning rate which controls the step size of an update. This is called the gradient descent method because in every step the network is updated in the direction in which the loss function decreases most. Going back to equation 4.8, the squared error of one datapoint can be expressed as

$$E_n = \sum_{k=1}^{K} (\hat{y}_{nk} - y_{nk})^2, \tag{4.10}$$

where $\hat{y}_{nk}$ and y_{nk} are the prediction and target for unit k of datapoint n. Using 4.6 and 4.7 the derivative of E_n to a weight w_{kj} in the second layer can be expressed as

$$\frac{\partial E_n}{\partial w_{kj}} = \frac{\partial E_n}{\partial a_k} \frac{\partial a_k}{w_{kj}}. \tag{4.11}$$

By introducing the error δ as

$$\delta_k = \frac{\partial E_n}{\partial a_k}, \tag{4.12}$$

and using 4.6 to obtain

$$\frac{\partial a_k}{w_{kj}} = z_j, \tag{4.13}$$

we can rewrite 4.11 to

$$\frac{\partial E_n}{\partial w_{kj}} = \delta_k z_j. \tag{4.14}$$

This demonstrates that the error of a unit, with respect to a weight, can be found by determining the error δ of the output units, and multiplying them by the input value z. Thus, in order to calculate the error of a unit in the hidden layer (δ_j) we need to sum over all K connected output units,

$$\delta_j = \frac{\partial E_n}{\partial a_j} = \sum_{k=1}^{K} \frac{\partial E_n}{\partial a_k} \frac{\partial a_k}{\partial a_j}, \tag{4.15}$$

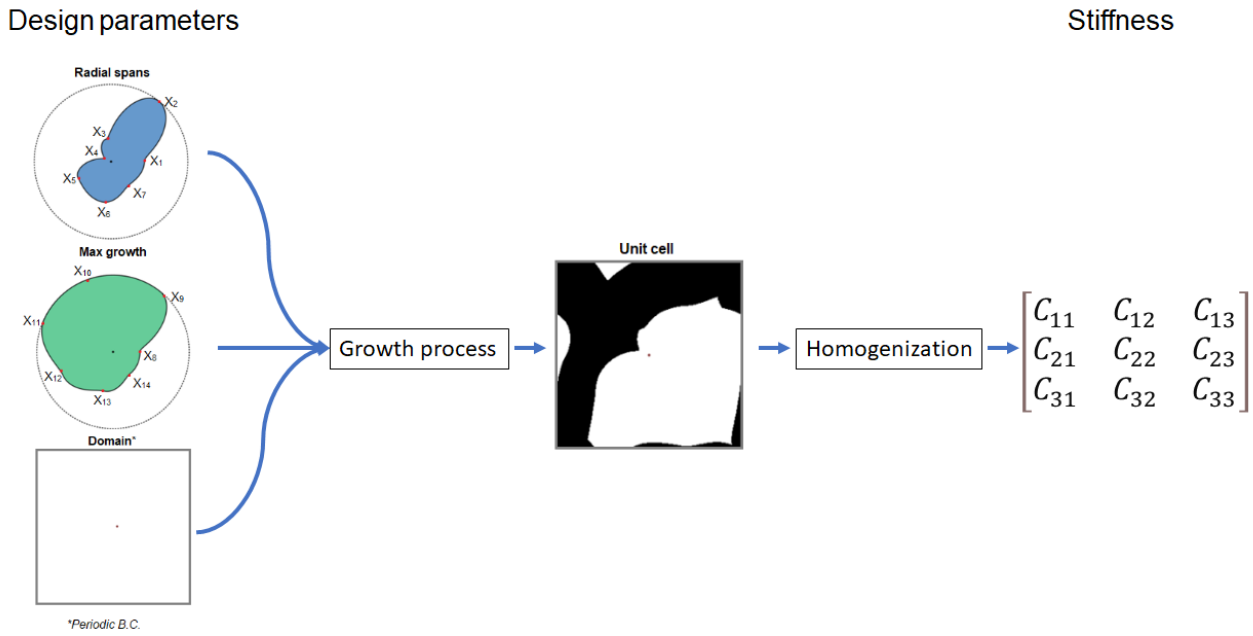

Figure 5.1: A schematic of the steps required to go from design parameters, to an image of a unit cell, to a stiffness matrix. From left to right: a set of design parameters that prescribe radial spans and maximum growth fed to the growth process, which outputs an image of the resulting unit cell. By homogenizing this image the stiffness matrix is obtained.

or

$$\delta_j = h'(a_j) \sum_{k=1}^{K} w_{kj} \delta_k. \tag{4.16}$$

This equation shows that the error of a hidden unit can be found through the errors in units deeper in the network. Therefore, this procedure is often referred to as backward propagation, as the errors flow to the network from output to input. For a dataset of multiple training points, the total error can be found by summing over the errors of each datapoint. Using the knowledge of the derivatives of the error with respect to the weights, the gradient descent method can be used to iteratively update the network. This is done by first performing a forward propagation of the training data, followed by backward propagation to find the derivates, and update the weights according to 4.9.

5 Design space and data generation

5.1 Design space

To train neural networks, a dataset of design parameters and associated stiffness components is required. For our method, one datapoint consists of a set of design parameters and six stiffness components. Although the relationship between design parameters and unit cell topology/stiffness is non-trivial, a correlation between them must exist. By obtaining a large enough database, a neural network can learn this correlation and predict stiffness properties directly from design parameters.

To produce one datapoint requires a number of steps, which are schematically depicted in figure 5.1. First, a set of design parameters is generated and provided to the growth process.This outputs a unit cell which is subsequently homogenized to obtain the stiffness matrix. The design parameters and stiffness components are together form a datapoint. To generate a database, random values are sampled for the design parameters and provided to the growth process. This produces random combinations of inputs and associated stiffness components. In principle, this method can produce a database of arbitrary size and in a format that is compatible with neural networks.

5.2 Data generation

The growth process requires an input of radial spans, and an equal number of max growth parameters. In principle there is no limit to how many spans can be prescribed. While a larger number of input parameters can open up a larger design space, it could also negatively affect neural network performance. To find out the optimal number of inputs, three datasets of 100.000 samples are created. Each set prescribing a different number of radial spans (and

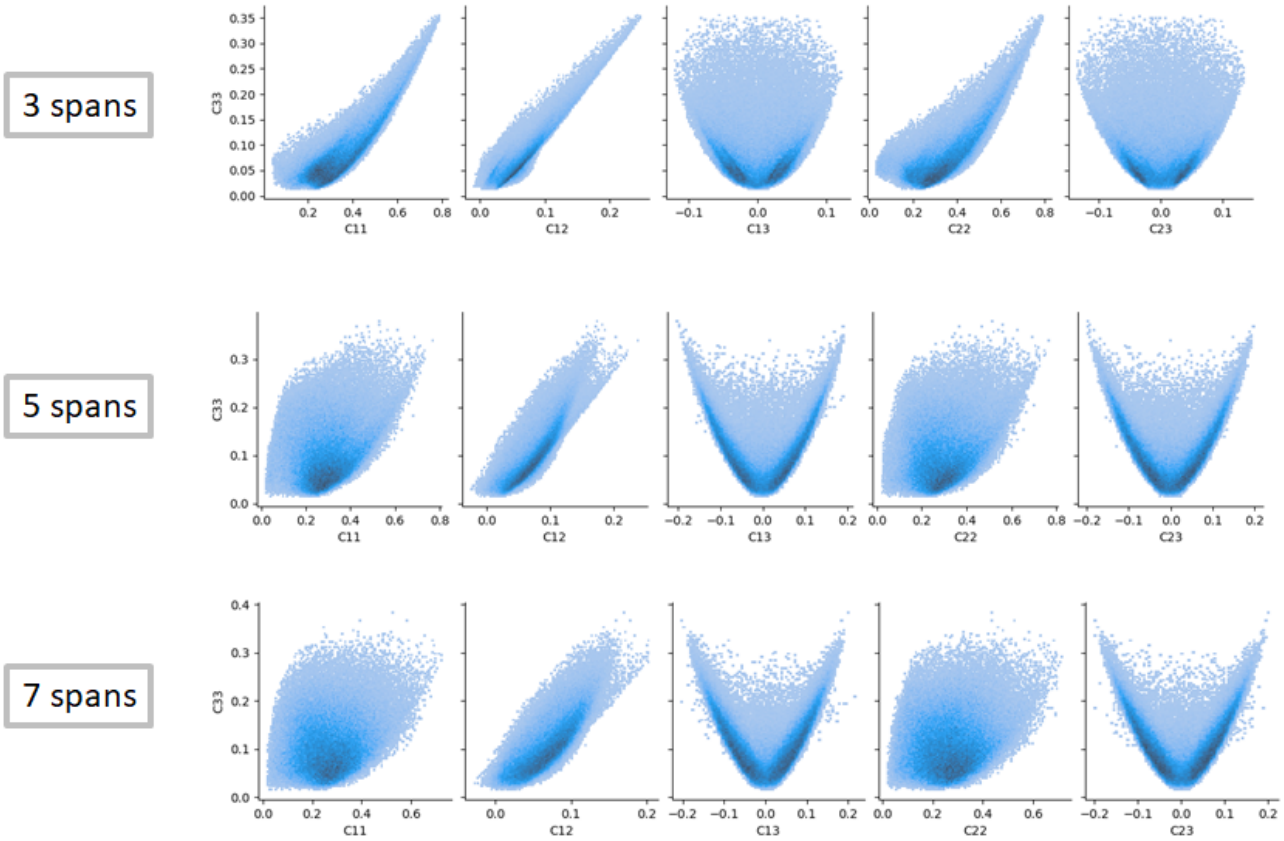

Figure 5.2: Correlation between component C_{33} and the other components of the stiffness matrix for different spans.

max growths): three, five or seven. This corresponds to sets of inputs of either six, ten or fourteen design parameters. For example, when three radial spans are prescribed, three max growth parameters need to be prescribed as well, leading to a total of six design parameters.

The three datasets are analysed to determine the influence of the number of prescribed spans on the design space. First, the correlation between the six stiffness components is studied. A strong correlation between two components indicates a small design space as it limits the possible combination of properties that can be achieved by one unit cell. Figure 5.2 shows the correlation between component C_{33} and the others for the three datasets. Correlation plots between all components can be found in Appendix A. Increasing the number of spans reduces the correlation between different components. This is most notable in the correlation between C_{33} and C_{11} and C_{22}, but can be observed for the other components too. In addition, the correlations between maximum and minimum Young's modulus, Poisson's ratio and shear modulus are compared. The ratio between the maxima and minima is a measure for the anisotropicity of a unit cell, as it indicates how much a property can vary within a single structure. The results, shown in figure 5.3, show that the design space of five and seven spans is notably larger than that of three spans. Comparing five and seven spans reveals that using seven spans does not increase the design space in terms of E and G much compared to using five spans. However, the range of possible Poisson's ratio's is significantly increased by using seven spans. These results are in line with the expectation that a larger number of design parameters opens up a larger design space.

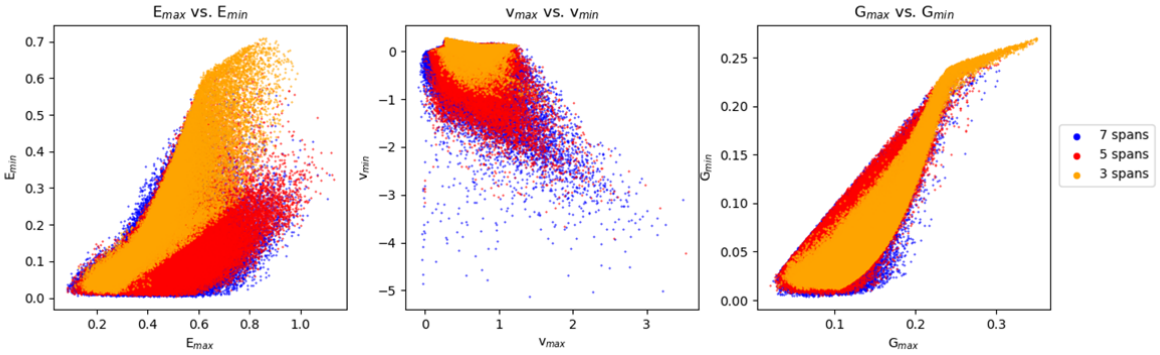

Figure 5.3: Correlation between maximum and minimum Young's modulus (left), Poisson's ratio (middle) and shear modulus (right).

5.3 Data verification

To test the impact of the number of spans on prediction accuracy on neural networks, the three datasets are used to train both forward and inverse models. The datasets are split in train, test and validation sets before training. The validation set is not used during training and is only used to validate the models. The forward models is verified by comparing query to prediction. The inverse models is verified by passing the predicted design parameters through the growth process, to obtain the predicted unit cells. The homogenized properties of the unit cells are compared to the original query for validation. The training and validation methods of both networks will be discussed in more detail in Section 6 and 7, respectively.
Figure 5.4 shows the prediction accuracy for the C_{11} component of each model. Results for the other components can be found in Appendix B. The prediction accuracy for three span unit cells are the most accurate, with $R^2 > 0.997$ for every component for both f-NN and i-NN. Increasing the number of prescribed spans does reduce accuracy, but does not lead to significant errors even with seven spans. A larger dataset will be used to train the final model, which is expected to increase accuracy.

Based on these results, a total of 1M datapoints is generated using seven prescribed spans. This dataset is inspected to verify that the input parameters are evenly distributed. It is found that all fourteen input parameters are sampled evenly, as illustrated by the histogram of one of the input parameters in figure 5.5, which is representative of all the other input parameters.

To verify the results of the homogenization process, both the distribution of, and the correlation between, the components is investigated. Strong correlation between some components, or sharp peaks in the individual distributions, could point to flaws in the data generation or homogenization process. Additionally, by visualizing the data distribution, it is possible to identify outliers, which could complicate the training process. The results, shown in figure 5.6, for the C_{33} component show smooth distribution curves, centered on a one or two mean values. The data for the other components can be found in figure A.4 in Appendix A.

6 Forward modelling

To apply neural networks to growth-based Voronoi metamaterials requires a forward and inverse model. The forward model will be trained to predict stiffness components from design parameters. Every unit cell is uniquely mapped to a stiffness matrix, which means this problem is well-posed. Therefore, it is likely that machine learning methods can be used to substitute the, computationally costly, growth and homogenization process, as visualized in figure 6.1. The design parameters will form the input $\boldsymbol{X}$, and the predicted six independent components of the stiffness matrix will form output $\hat{\boldsymbol{y}}$, with target values $\boldsymbol{y}$.

6.1 Methodology

The dataset is split in a training, test and validation set, comprising 80%, 15% and 5%, of the total data number of datapoints, respectively. The input parameters are normalized before training. The stiffness components are not transformed in order to be able to implement Cholesky factorization, which will be discussed in section 6.1. However, since all stiffness components have similar orders of magnitude (between -1 and 1), this is not expected to lead to problems during training. The networks are trained on the training set, while the test set is used for early stopping. The loss function that the models aims to minimize is the Mean Absolute Error (MAE) of the difference between

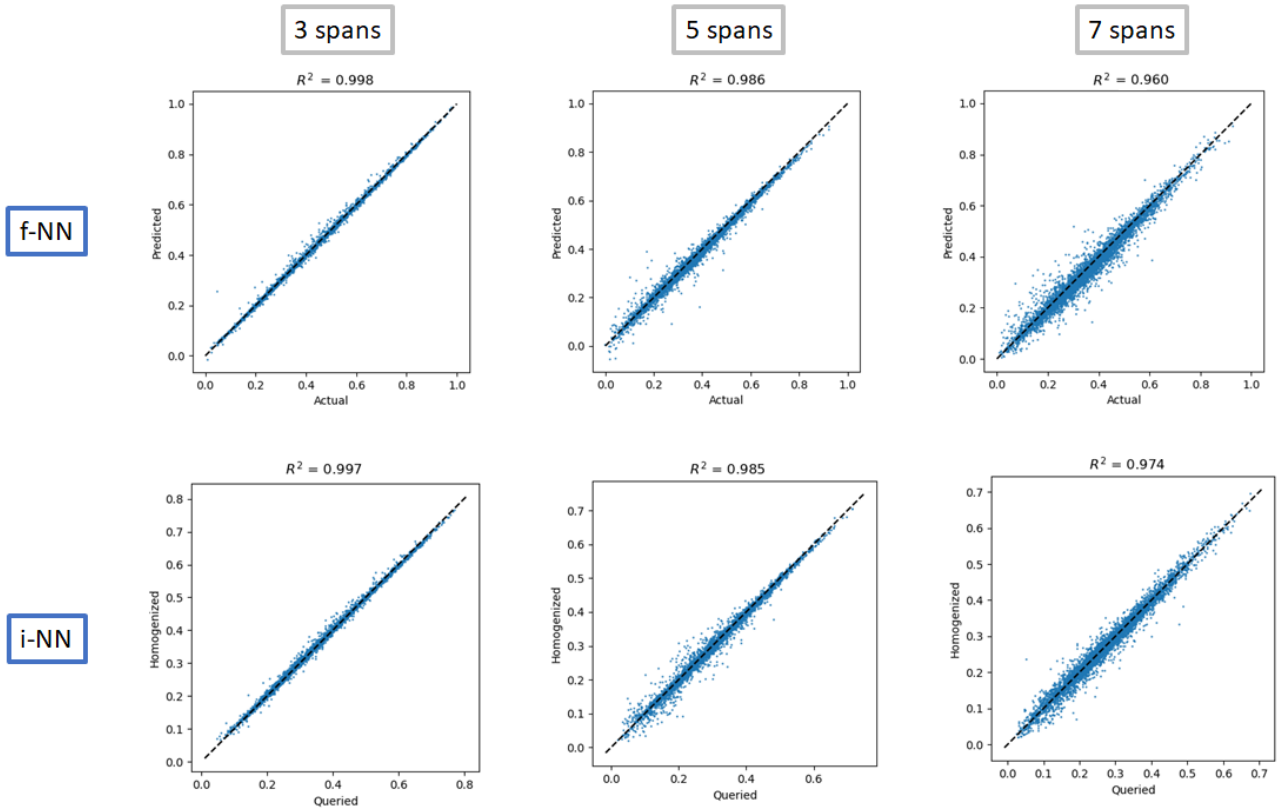

Figure 5.4: Accuracy of predictions for C_{11} of trained f-NN (top) and i-NN (bottom) networks using (from left to right) 3, 5 or 7 prescribed spans.

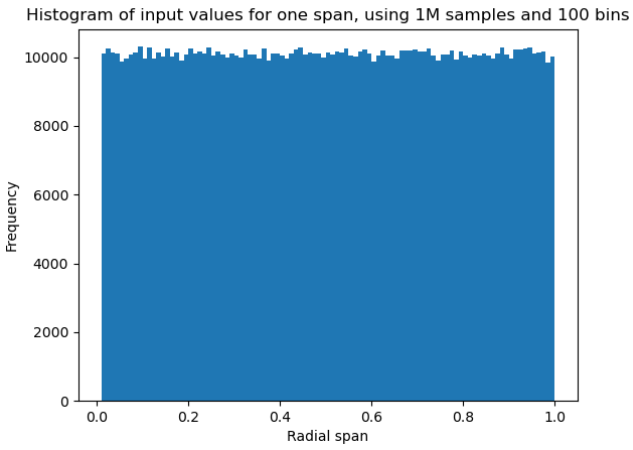

Figure 5.5: Histogram of the distribution of randomly sampled values for one input parameter.

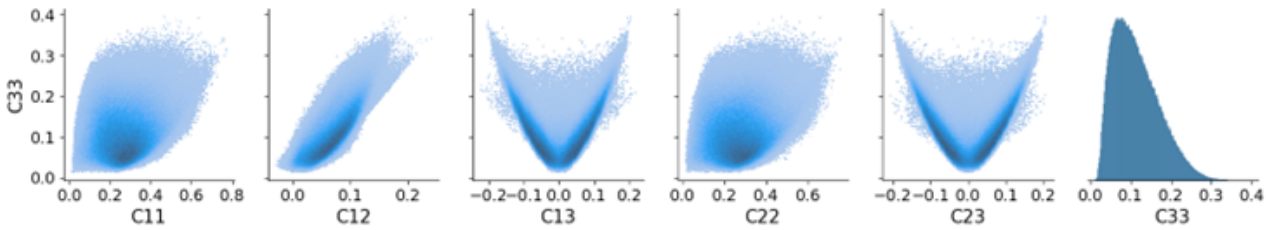

Figure 5.6: Distribution of, and correlation between, C_{33} and the five other independent components of the stiffness matrix for 1M samples.

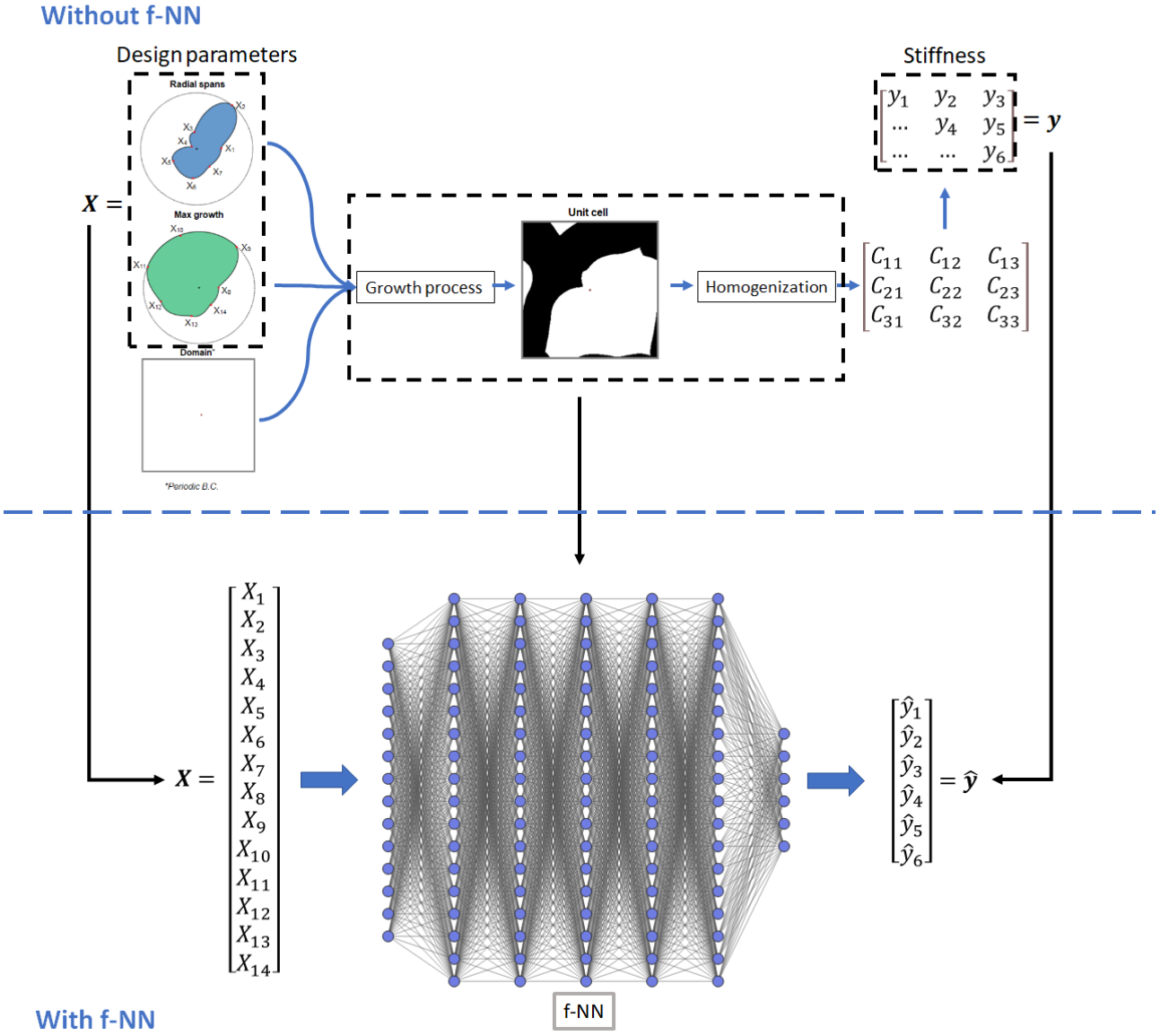

Figure 6.1: The forward network can act as surrogate model for the growth process and homogenization procedure, significantly improving the speed at which stiffness properties can be predicted. The neural network takes fourteen design parameters ($\boldsymbol{X}$) as input and predicts the associated stiffness properties ($\hat{\boldsymbol{y}}$).

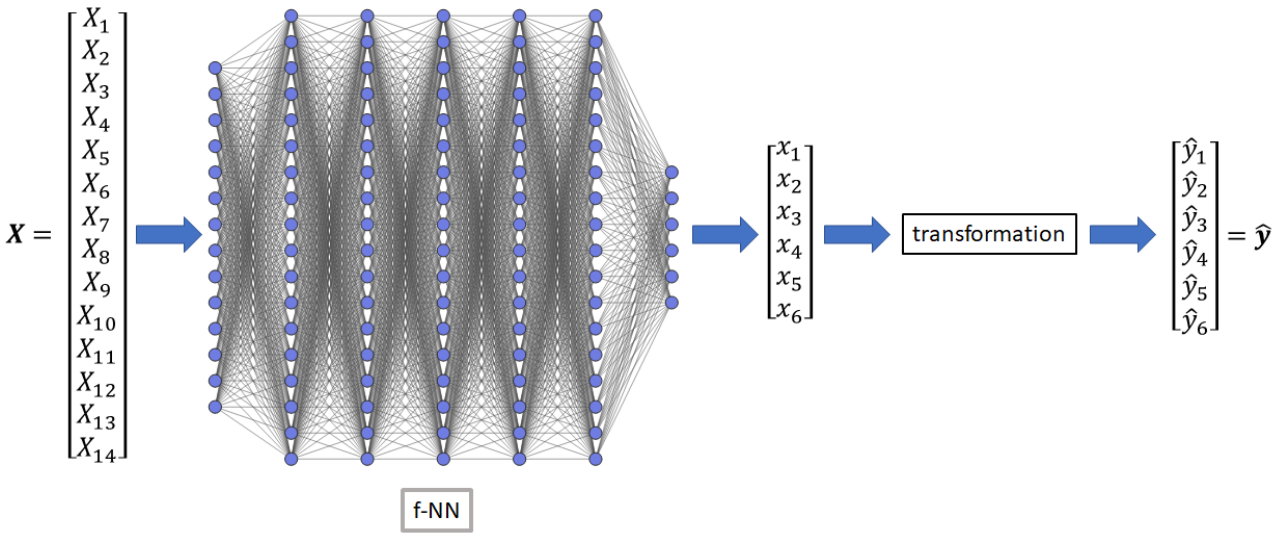

Figure 6.2: The outputs of the forward network (x_1, x_2, x_3, x_4, x_5, x_6) go through a transformation layer to produce physically admissible stiffness matrix predictions ($\hat{\boldsymbol{y}}$).

predicted stiffness, $\hat{\boldsymbol{y}}$, and actual stiffness, $\boldsymbol{y}$,

$$\frac{1}{N}\sum_{i=1}^{N}|\hat{\boldsymbol{y}}_i - \boldsymbol{y}_i|. \tag{6.1}$$

The validation set is used to verify the accuracy of the trained model. Both the forward and inverse model are programmed in Python using the Pytorch module. Pytorch allows customization of network parameters such as configuration of the number of layers, layer width, activation function and error function. After several iterations it is found that a model with five layers, each 512 wide, using softplus activation functions, produced the most accurate models without overfitting.

Cholesky factorization

For a stiffness matrix to be physically admissible, it must be symmetric positive definite (SPD). However, using neural networks to predict stiffness matrices does not guarantee this property. A solution has been proposed by Jekel et al.[172] through the implementation of a Cholesky factorization transformation layer. The Cholesky decomposition of a real stiffness matrix is expressed as

$$\boldsymbol{C} = \boldsymbol{L}\boldsymbol{L}^{\mathrm{T}}. \tag{6.2}$$

If $\boldsymbol{L}$ is a lower triangular matrix with positive values on the diagonal, the stiffness matrix is guaranteed to be SPD. Therefore, if an $\boldsymbol{L}$ can be made that meets these requirements, a SPD stiffness matrix can always be constructed. To implement this in the forward network, a transformation layer as added to the output. Consider the model in figure 6.2 where the outputs of the f-NN have been renamed to x_1, x_2, x_3, x_4, x_5 and x_6. These terms are rearranged to form a lower triangular matrix,

$$\boldsymbol{L} = \begin{bmatrix} p(x_1) & 0 & 0 \\ x_2 & p(x_3) & 0 \\ x_4 & x_5 & p(x_6) \end{bmatrix}, \tag{6.3}$$

where a softplus activation function ($p(x)$) is applied to the diagonal terms. The softplus activation function will output a positive value for any input, figure 4.3. Thus, 6.3 will always have positive diagonal components. Combining and 6.2 and 6.3, the SPD stiffness matrix prediction can be constructed,

$$\boldsymbol{L}\boldsymbol{L}^{\mathrm{T}} = \begin{bmatrix} p(x_1) & 0 & 0 \\ x_2 & p(x_3) & 0 \\ x_4 & x_5 & p(x_6) \end{bmatrix} \begin{bmatrix} p(x_1) & x_2 & x_4 \\ 0 & p(x_3) & x_5 \\ 0 & 0 & p(x_6) \end{bmatrix} = \begin{bmatrix} \hat{y_1} & \hat{y_2} & \hat{y_3} \\ & \hat{y_4} & \hat{y_5} \\ symm & & \hat{y_6} \end{bmatrix}. \tag{6.4}$$

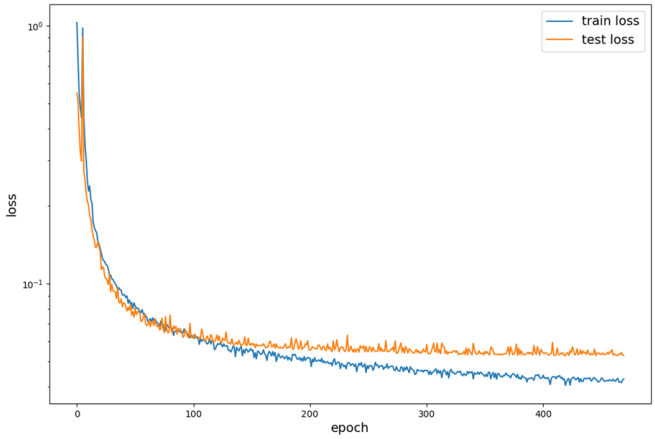

(a) f-NN loss (MAE) as function of epoch.

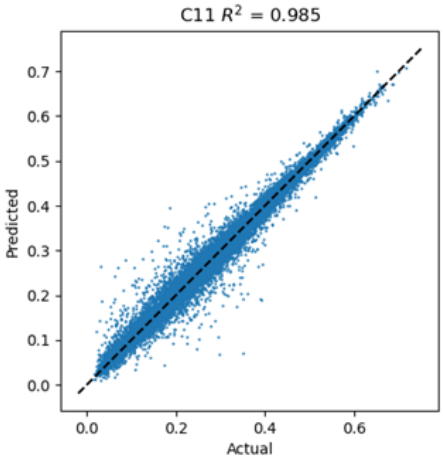

(b) C_{11} component - predicted vs. query

Figure 6.3: (a) Evolution of the Mean Absolute Error (MAE) of the train and test set for the forward model. **(b)** Predicted vs actual values of the C_{11} component of the stiffness matrices of the validation set (50k samples) using the forward model. The dashed lines indicate the points of perfect match between query and prediction.

The six independent stiffness components form the new output of the network $\hat{\boldsymbol{y}}$. Because $p(x_1)$, $p(x_2)$ and $p(x_3)$ are guaranteed to be positive, every stiffness prediction will be physically admissible. When the f-NN is schematically shown in other figures, the transformation layer will not be shown to avoid clutter.

6.2 Validation

During training, the evolution of the train and test error is monitored to determine if the model has been overfitted, figure 6.3a. In case of overfitting it is expected that the train loss is significantly smaller than the test loss. However, the train and test loss show very similar patterns, not indicative of overfittin, with values after the final epoch of 0.043 (train) and 0.053 (test). After training, the accuracy of the model is analysed using the validation set. The validation set is never used during training so the data is new to the model. The input parameters of the validation set are queried, and stiffness predictions are compared to the actual stiffness values. To visualize the results, the predicted stiffness values are plotted against the actual values. Figure 6.3b shows the correlation for C_{11}, plots for the other components can be found in Appendix B. Additionally, the R^2 value for each component is calculated, to quantify the accuracy of the predictions. A value of 1 indicates perfect correlation while a value of 0 indicates no correlation at all. The forward model produces R^2 scores above 0.98 for each component.

7 Inverse modelling

The inverse model should predict design parameters based on stiffness queries. However, there can be multiple designs that can produce a given stiffness matrix, which makes the inverse problem ill-posed. To overcome the ill-posedness a novel approach is implemented, following the work done by Kumar et al.[65]. This method uses a combination of forward and inverse neural networks to render the inverse problem well-posed. This allows training of the inverse network to reproduce queried stiffnesses without trying to reproduce specific design parameters.

7.1 Methodoloy

In this approach the trained forward model is used during the training of the inverse model. It takes the predicted design parameters from the inverse model to predict stiffness components. The error between queried stiffness and predicted stiffness is used to train the inverse network, this process is illustrated in figure 7.1. By training the inverse model to reduce the error in stiffness, instead of the error in design parameters, the problem is rendered well-posed.

Lets consider a single datapoint to illustrate the training process. One datapoint consists of fourteen design parameters ($\boldsymbol{X}$) and six target stiffness components ($\boldsymbol{y}$). The six stiffness components are provided as input to the i-NN model, which predicts a set of fourteen design parameters ($\hat{\boldsymbol{X}}$). These are passed through the the (trained) forward model, which produces six stiffness component predictions ($\hat{\boldsymbol{y}}$). The error function to be minimized then

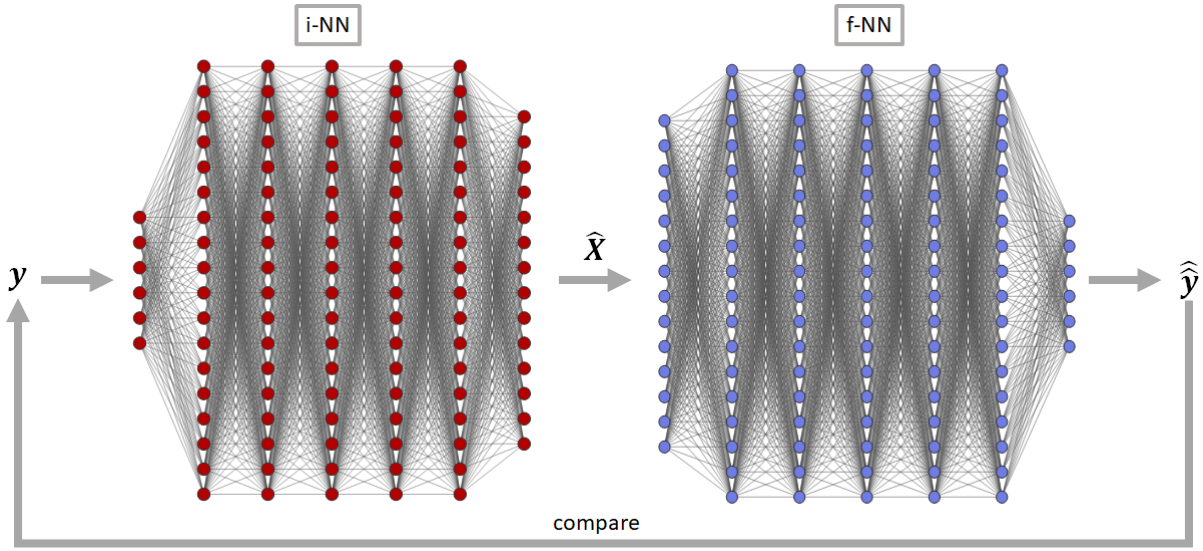

Figure 7.1: A diagram illustrating the training of an inverse model (i-NN) using forward model (f-NN) to predict stiffness. The i-NN takes a stiffness query ($\boldsymbol{y}$) and predicts a set of design parameters ($\hat{\boldsymbol{X}}$). These are provided to the f-NN to predict the stiffness properties $\hat{\hat{\boldsymbol{y}}}$. The predicted stiffness is compared to the queried stiffness to update the i-NN during training.

becomes

$$\frac{1}{N}\sum_{i=1}^{N}|\hat{\hat{\boldsymbol{y}}}_i - \hat{\boldsymbol{y}}_i|. \tag{7.1}$$

A network configuration similar to that of the f-NN is used: five layers with a width of 512, using softplus activation functions.

7.2 Validation

Evaluating the loss history indicates that no overfitting took place, figure 7.2a. To validate the output of the i-NN model, additional steps are required, compared to those used for f-NN. To validate the f-NN model, input parameters of the validation set were queried, and predicted stiffness components were compared to stiffness components of the dataset. However, the i-NN is not trained to reproduce the input parameters of the original dataset. Instead, it is trained to produce accurate stiffness predictions, regardless of the original input parameters. This process involves the f-NN, which plays an essential role in determining the prediction error. Therefore, if the model would be validated the same way that it was trained (i.e. by querying stiffness components to the i-NN, and using the f-NN to verify the predictions) it would be impossible to identify errors introduced by the f-NN. To remedy this, the stiffness values of the validation set are queried to the trained i-NN model and the predicted design parameters are provided to the growth process. This produces the unit cells of the i-NN predictions, which are used to obtain the homogenized stiffness components. These components are compared to the queried values to validate the accuracy of the inverse model, figure 7.2b. The results indicate remarkable accurate predictions, with R^2 values above 0.99 for all but one component.

7.3 Correlation with density

The density (ρ) of a unit cell is defined as the ratio of material pixels (n_{px}) to total number of pixels (N),

$$\rho = \frac{n_{px}}{N}. \tag{7.2}$$

To compare the density of queried and predicted samples, 10.000 samples are randomly generated and homogenized. The homogenized stiffness values are queried to the i-NN and the outputs are used to grow the predicted microstructures. Subsequently, the densities of the queried and predicted materials are compared to investigate their correlation, figure 7.3. The histogram shows a strong correlation between prediction and query, with an R^2 value of 0.833. The model does not directly aim to reproduce density between query and prediction. However, stiffness of a unit cell is related to its density so it would be expected that densities between query and prediction are correlated.

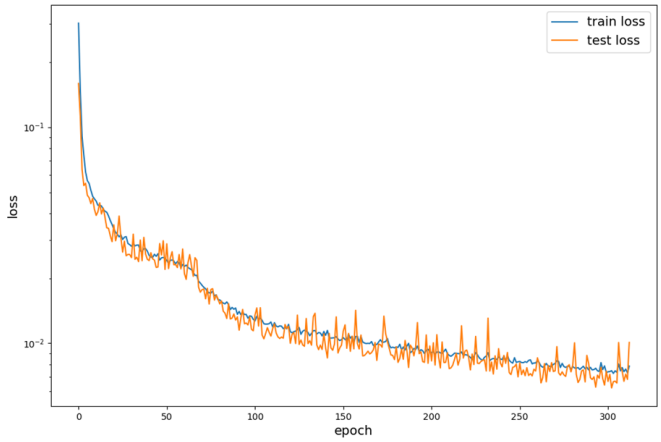

(a) i-NN loss as function of epoch.

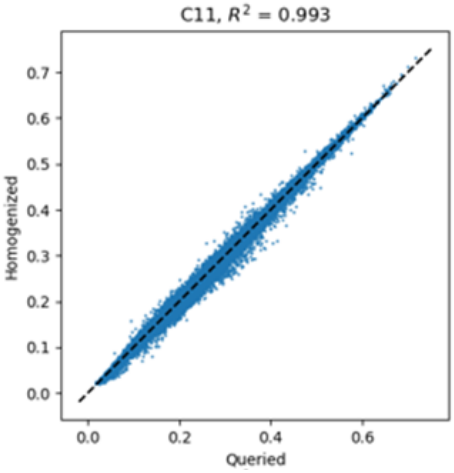

(b) C_{11} component - homogenized vs. query

Figure 7.2: (a) Evolution of the Mean Absolute Error (MAE) of the train and test set for the inverse model. **(b)** Predicted vs homogenized values of the C_{11} component of the stiffness matrices of the validation set (50k samples) using the inverse model. The dashed lines indicate the points of perfect match between query and homogenized property.

7.4 Verification of non-uniqueness challenge in inverse design

To compare input parameters of queried and predicted materials, the values of the validation set are queried to the i-NN. The predicted input parameters are compared to those of the original query. As mentioned in the introduction of this chapter, it is expected that there is a weak correlation between the two. This is confirmed by the histogram plot in 7.4, which shows the correlation between query and prediction for one of the input parameters. This plot is representative of correlations of the other thirteen inputs.

To study this behaviour in more detail, microstructure and properties of queried and predicted materials are compared, figure 7.5. Interestingly, the input parameters are very different between query and prediction, and so is the resulting microstructure. However, when inspecting the stiffness components and material properties, there seems to be a very close match between the two. The i-NN is able to accurately recreate material properties despite producing a vastly different combination of input parameters.

7.5 Young's modulus, Poisson's ratio and shear modulus

To compare queried to predicted material properties the Young's modulus, Poisson's ratio and shear modulus of the validation set are compared to those of the predictions. The maximum and minimum values of E, ν and G of the queries are determined and the direction, $\vec{n}$, at which these values were found are stored. The material properties in the same $\vec{n}$ direction of the predicted materials are compared to the queried values, figure 7.6. The correlation

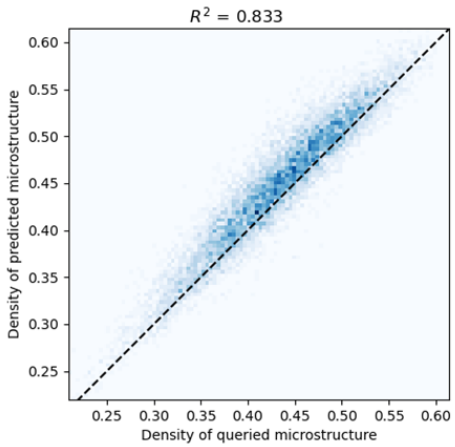

Figure 7.3: Histogram of the correlation between densities of queried and predicted unit cells of 10000 samples using 100×100 bins .

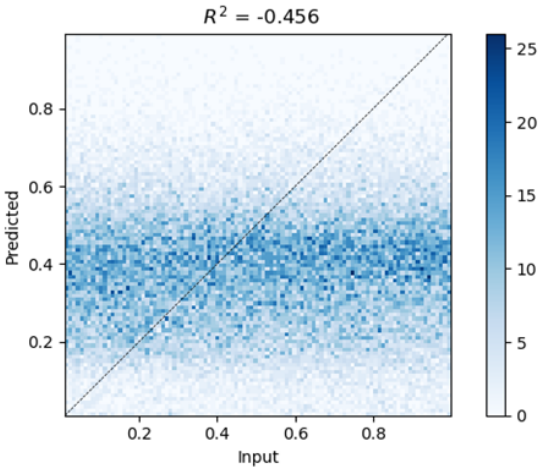

Figure 7.4: Correlation between queried and predicted values of one input parameter of the validation set.

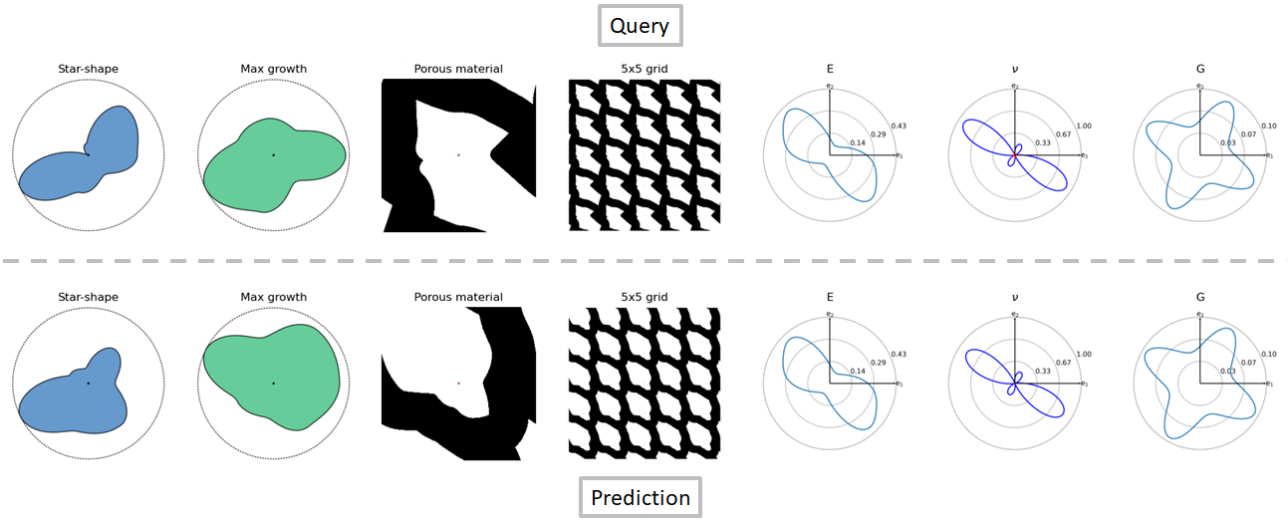

Figure 7.5: Comparison between queried (top) and predicted (bottom) microstructures and elastic properties. From left to right: the input parameters for the growth process (star-shape and max growth), microstructure (porous material) unit cell, 5x5 tessellation of unit cells (5x5 grid), Young's modulus (E), Poisson's ratio (ν) and shear modulus (G).

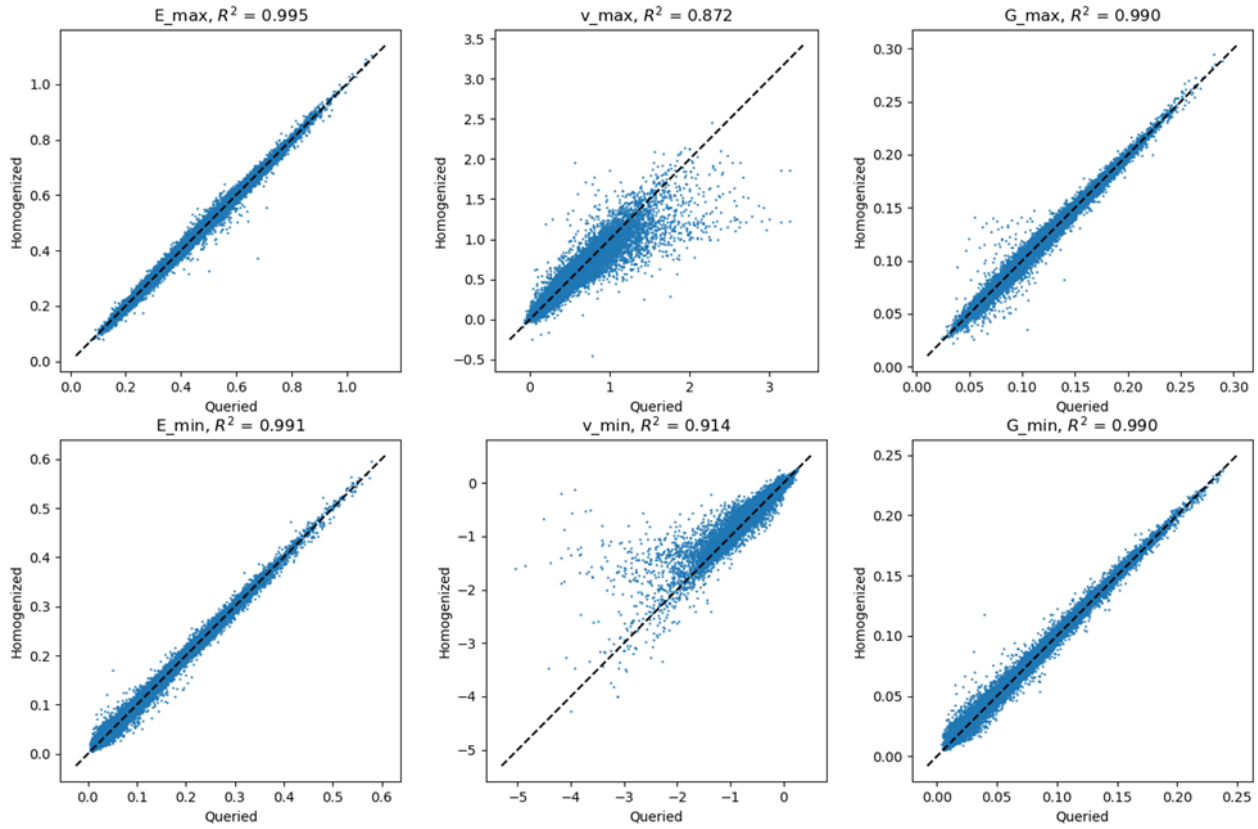

Figure 7.6: Correlation of maximum and minimum E, ν and G values between homogenized (predicted) and queried samples. Values for of the predicted samples were calculated in the directions in which the respective max/min values were found in the queried samples.

between these values is less than for the stiffness components, in particular for the Poisson's ratio. This can partially be explained by the fact that the network is not trained to predict these values directly. Additionally, ν may be sensitive to small variations in the stiffness matrix. A last point of consideration in this regard, is that this analysis only takes into account directional properties. These may highlight local discrepancies between queries and predictions that have little influence on the global behaviour.

7.6 Generalization beyond the design space

The model is trained, verified and inspected using growth based microstructures only. To test the versatility of the model, random microstructures are selected, and their homogenized stiffness components queried to the i-NN. The predicted designs and their properties are subsequently compared to those of the original designs, figure 7.7. A circular microstructure would be challenging (although not impossible), to reproduce using the growth process, since we prescribe an odd number of radial spans. Figure 7.7a shows that the reproduced microstructure is not visually similar to the original circle. However, the material properties and stiffness components show an accurate match between query and prediction. The diagonal voids in the queried design of figure 7.7b are impossible for the growth process to replicate since it can only produce single void per unit cells. As such, the predicted microstructure is very different from the original, yet it shows a similar void elongation orientation. Additionally, the material properties of the predicted microstructure closely match those of the original. A symmetric star-shape with eight spans 7.7c cannot be perfectly replicated with seven prescribed spans. The model predicts a nearly square shaped microstructure which closely, but not perfectly, the queried properties. The predictions has similar symmetry as the original query, albeit with a very different topology.

The stiffness reconstruction of all three non-growth based queries is remarkable, given that the structures were impossible to perfectly reconstruct. Despite, small difference between queried and predicted stiffness, these result demonstrate that the growth-based method has the potential to reproduce properties from structures outside its original design space.

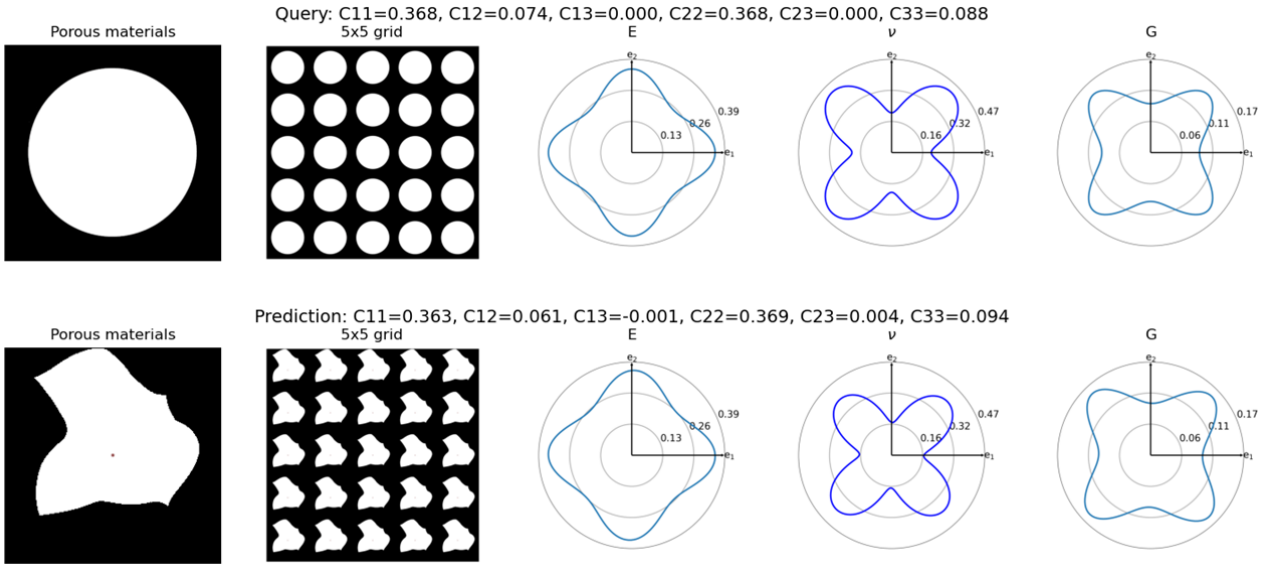

(a) Microstructure with circular void.

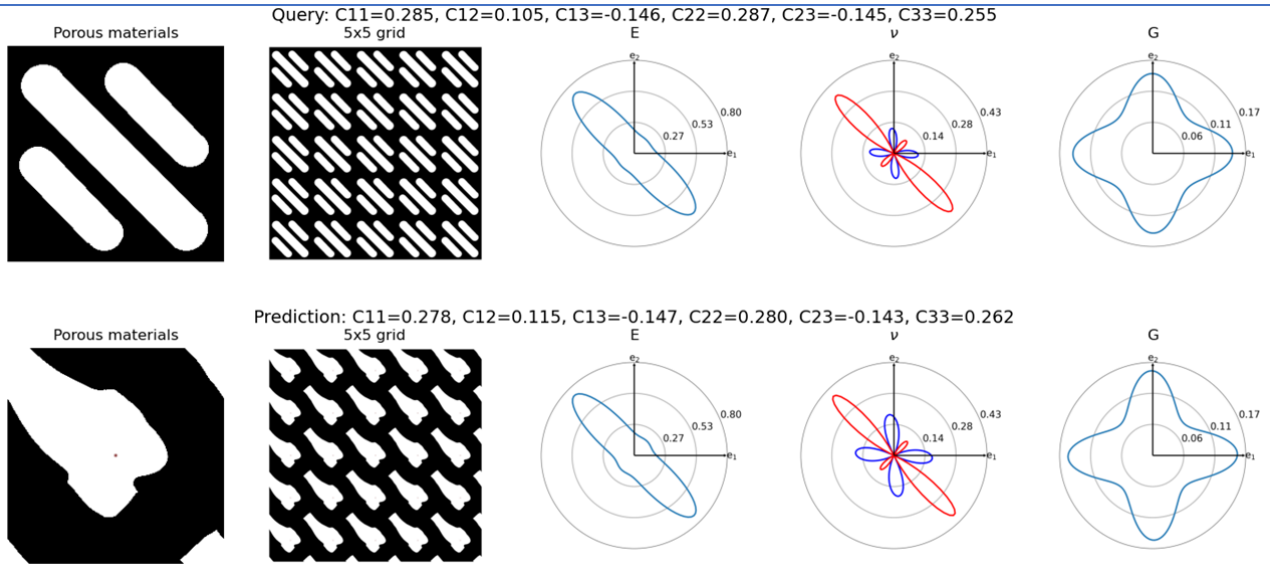

(b) Microstructure with diagonal voids.

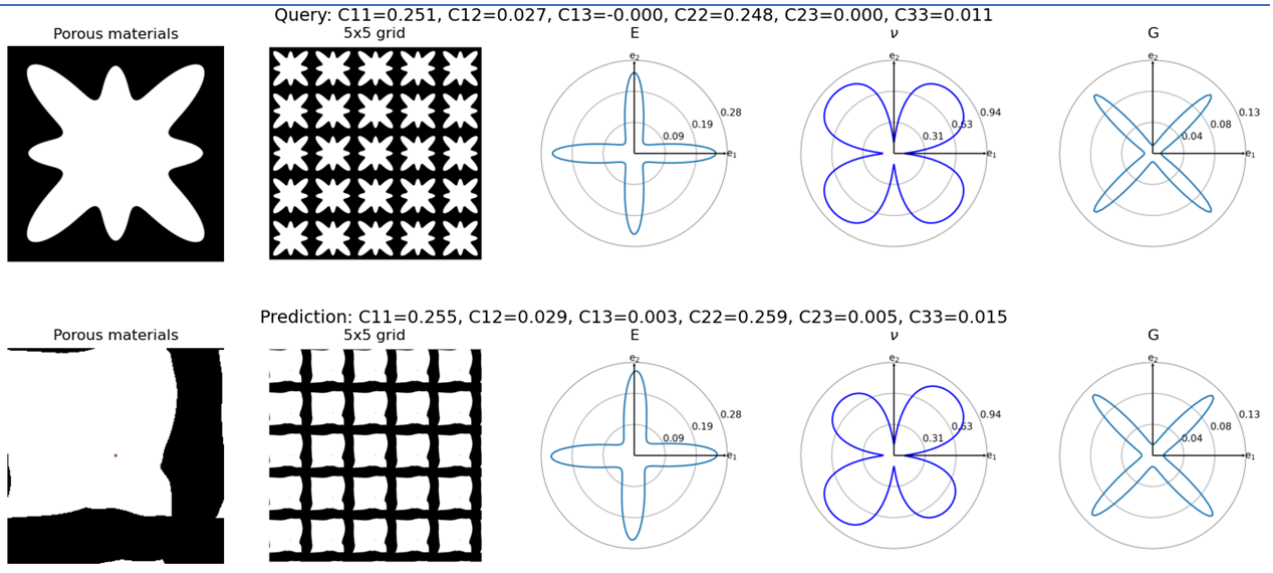

(c) Microstructure with a star void.

Figure 7.7: Comparison of query (top rows) and prediction (bottom rows) of two non-growth-based microstructures, whose homogenized stiffness were queried to the i-NN.

Table 8.1: R^2 values of the validation set for the six stiffness components at different levels of dropout.

	Dropout			
Component	**0.2**	**0.5**	**0.8**	**0.9**
C_{11}	0.996	0.984	0.921	0.862
C_{12}	0.980	0.946	0.880	0.745
C_{13}	0.997	0.988	0.956	0.929
C_{22}	0.995	0.984	0.918	0.846
C_{23}	0.996	0.986	0.946	0.929
C_{33}	0.991	0.962	0.891	0.777

8 Stochastic inverse design

The model that has been treated in the previous chapter is deterministic and generates a single set of design parameters per queried stiffness. However, it may be desirable to obtain multiple designs for a queried stiffness to allow an engineer to select the most suitable design for a specific purpose. To make a model that can make multiple and varying predictions, a number of methods are implemented. The first method makes use of dropout to randomly switch off parts of the network during, and after, training. The second method makes use of the FFT difference between unit cells to promote difference during training.

8.1 Dropout

Dropout is a technique whereby random parts of the neural network are switched off during training [173]. Typically, this is used to improve neural network performance and reduce the risk of overfitting. However, it could theoretically be used to predict multiple designs, in case dropout is also used when predictions are made with a trained model. If random parts of the network are switched off when querying, multiple queries of the same stiffness could produce different designs.

8.1.1 Methodology

Dropout can be set to any value between 0 and 1, with 0 corresponding to no dropout and 1 to a complete network switch off. It is expected that the fraction of the network that is randomly switched off will influence both the accuracy of the predictions, as well as the variability in designs. High dropout may produce more varied designs but lack accuracy, while high accuracy and small variations may be obtained with low dropout. To test this hypothesis, inverse networks (similar to the i-NN discussed in section 7) with 0.2, 0.5, 0.8 and 0.9 dropout are trained and their accuracy is compared using the validation set. Additionally, multiple queries of the same stiffness are done to compare variability in design.

8.1.2 Validation

It is found that increasing dropout leads to lower accuracy, which is reflected in the R^2 values of the stiffness components, table 8.1. At 0.2 dropout all R^2 values are above 0.98 while values as low as 0.745 are obtained at 0.9 dropout. However, the latter model is the only one to show noticeable variation in design across multiple queries of the same stiffness, three examples of which are shown figure 8.1. It is interesting to note that the predicted design parameters can take very different values from structure to structure, while still producing similar properties. However, despite these variations in design parameters the actual microstructures are visually similar, with only minor variations in designs.

8.2 Promoting difference

Using dropout to produce multiple designs has the potential to produce multiple random designs but it offers no means to influence the output. Additionally, there is no inherent incentive for the model to produce a wide variety of designs. These issues are addressed by considering the difference between designs during training. By training a model to produce multiple predictions and rewarding difference between them in the loss function, it is possible to promote variation in design.

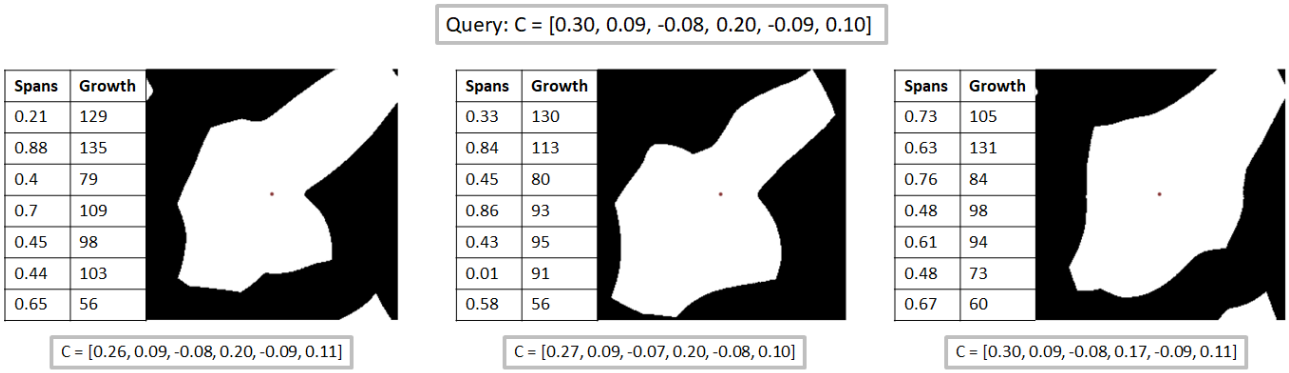

Figure 8.1: Three different microstructures that were produced for a single stiffness query, using a NN with 0.9 dropout. The design parameters and stiffness components for each prediction are plotted to the left and below each unit cell, respectively.

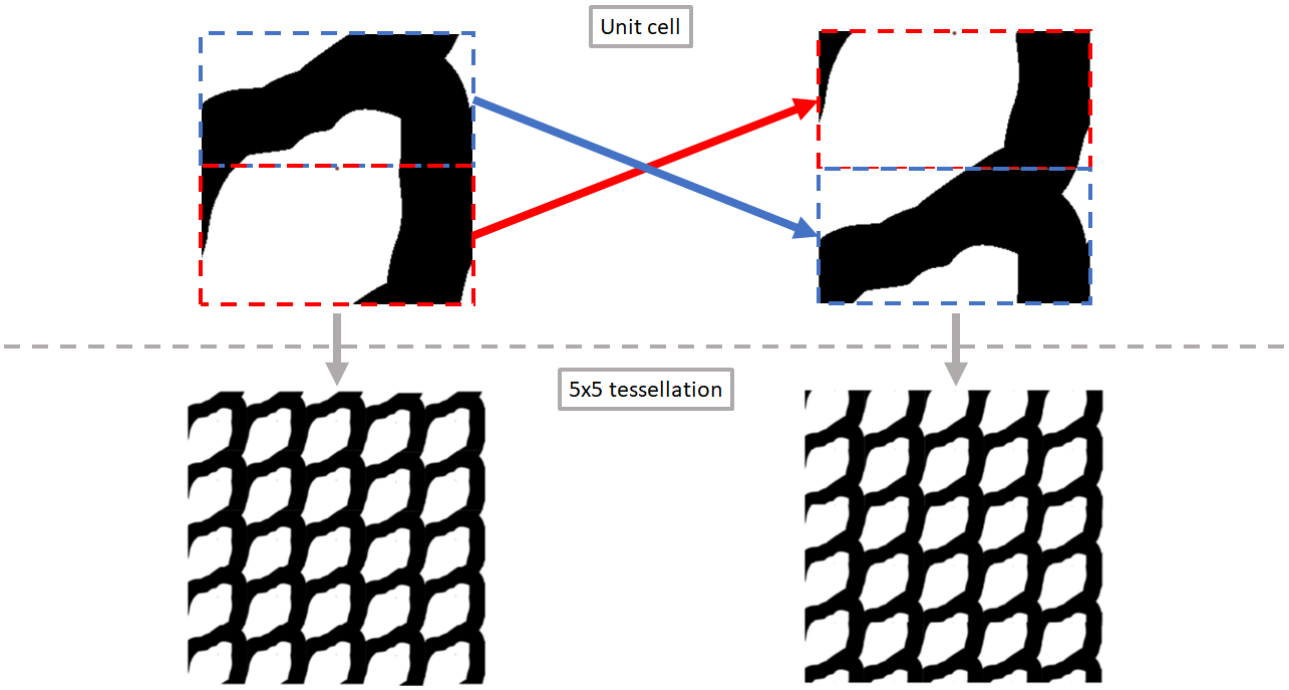

Figure 8.2: The unit cell on the right is created by swapping the bottom and top half of the unit cell on the left. Tiling together multiple unit cells produces the same pattern.

8.2.1 Defining difference

This approach requires a quantitative measure for difference that scales depending on how dissimilar two designs are. A straightforward measure would be to take the sum the number of dissimilar pixels between two designs. However, this method does not take into account that translationally symmetric unit cells have similar properties under the assumption of periodic boundary conditions, as illustrated by the example in figure 8.2. In this example, two unit cells with translational symmetry are created by swapping the top and bottom half of the original unit cell. By creating a 5x5 grid of unit cells, the same structure emerges, despite using two unit cells with a large number of dissimilar pixels.

Instead of counting dissimilar pixels, a Fast Fourier Transform (FFT) is used to determine differences between microstructures, while also accounting for translational symmetry. The FFT algorithm converts data from a spatial domain to a frequency domain in terms of complex numbers [174]. The FFT data can be stored in a matrix of the same size as the original image (128x128). The absolute values, $F = |\text{FFT}|$, can be plotted and compared for different microstructures, figure 8.3.

The example in this image demonstrates that translated images are represented by the same F, even with cross-boundary features, while different structures produce different F matrices. To capture the difference (D) between two microstructures (k and l) in a single value we define

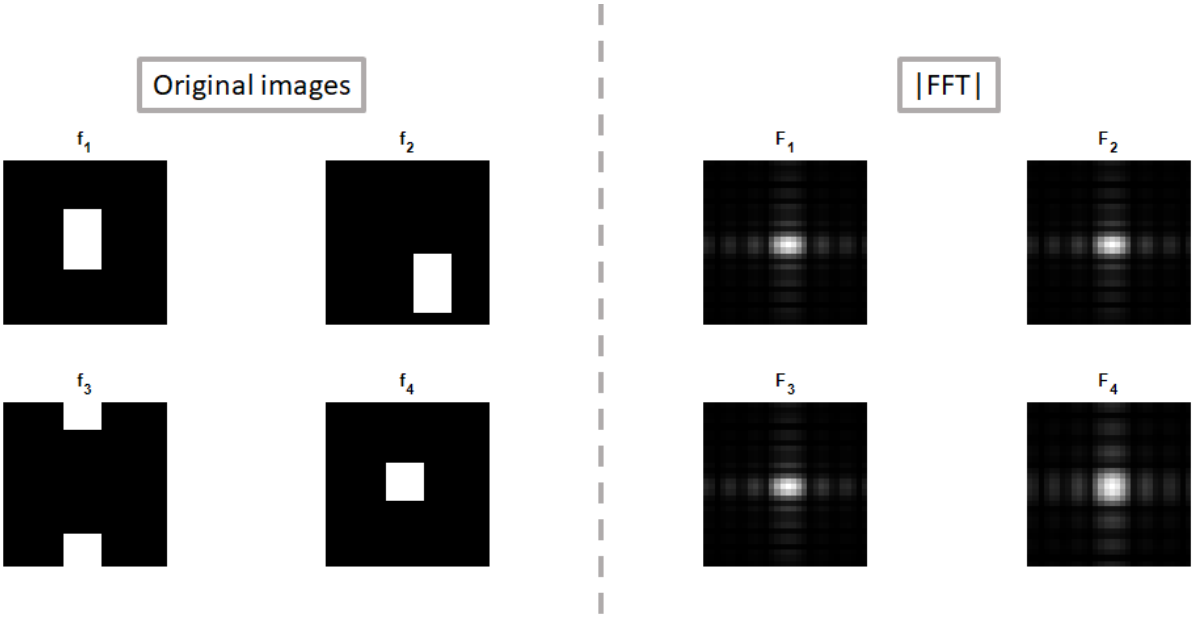

Figure 8.3: Original images, (left) and the absolute values of their FFT (right). The first three images, f_1, f_2 and f_3 are translations of each other, while f_4 has a different structure. As a result, F_1, F_2 and F_3 are similar to each other but different from F_4.

$$D_{kl} = \sum_{i=1}^{128} \sum_{j=1}^{128} |F_k(i,j) - F_l(i,j)|, \tag{8.1}$$

where i and j correspond to matrix indices. Applying equation 8.1 to the example of figure 8.2 yields $D_{12} = D_{13} = D_{23} = 0$ and $D_{14} = D_{24} = D_{34} = 315$, demonstrating that translational symmetry is taken into account in this definition of difference.

8.2.2 Data generation

Definition 8.1 requires the input of two microstructures, and their FFT, to calculate difference. The i-NN discussed in section 7 predicts a set of input parameters for every query. Thus, to include D in its loss function would require knowledge of the microstructure associated with each prediction, which means every set of input parameters would have to pass through the growth process. This would make the training process computationally inefficient. A more efficient method would be to use a NN (d-NN) to predict the difference between two designs directly from input parameters, figure 8.4.

To train the d-NN requires a database of pairs of design parameters and their difference. The database discussed in section 5.2 holds data on 1M sets of input parameters and associated microstructures. To create a database for the training of d-NN, two samples were randomly selected from the 1M structures and their D calculated. The two sets of input parameters, together with D, form one datapoint. This method is used to generate a 1M datapoints. However, it is found that the data is unevenly distributed, which leads to problems during d-NN training. To get a more evenly distributed database, 100M datapoints are generated, and selectively sampled to produce a database of 1M points with a more even distribution, figure 8.5. With this database a d-NN is trained that can accurately predict the normalized difference between two microstructures, with an R^2 of 0.920.

8.2.3 Implementation

To integrate difference into the training procedure it is necessary to obtain at least two predictions for every query. Additionally, the aim is to include a method to control the variation in the designs to some degree. To that end, a new input variable (z) is introduced which can have an arbitrary number arguments, each of which can take any value between 0 and 1. During training of the i-NN z will be provided as input to the i-NN, along with the stiffness query. Every stiffness query will be passed to the i-NN at least twice, each time with a different z. The stiffness of predicted designs can be calculated using the trained f-NN while the difference between different designs can be determined by the trained d-NN. Figure 8.6 shows the training process with two passes. For the sake of simplicity, the following

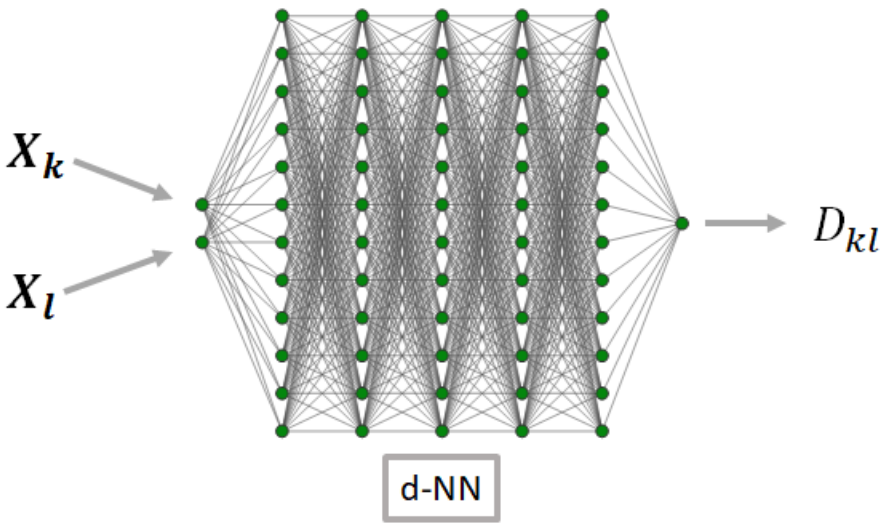

Figure 8.4: A neural network (d-NN) can be used to predict the difference (D_{kl}) between two microstructures directly from their input parameters ($\boldsymbol{X}_k$ and $\boldsymbol{X}_l$). Please note that each set of input parameters contains fourteen inputs, leading to a total number of input nodes of 28.

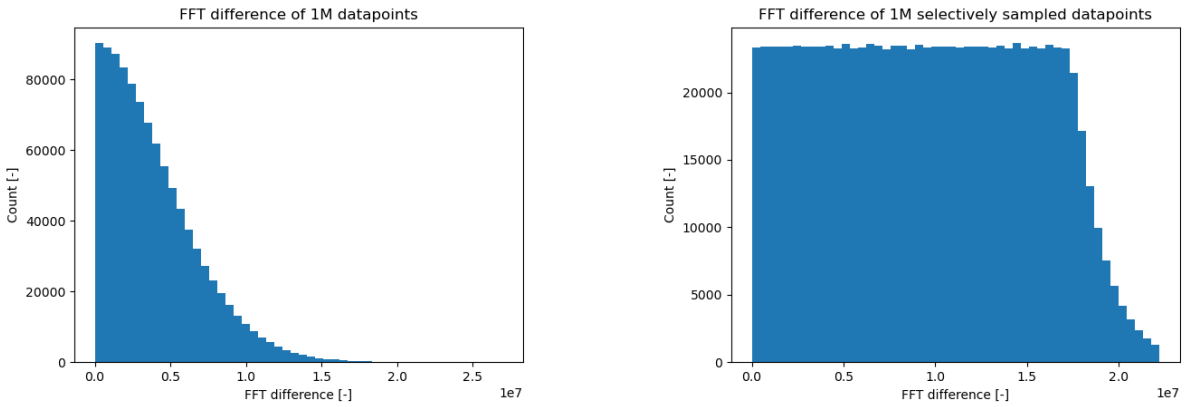

Figure 8.5: Distribution of difference data from 1M randomly generated data points (left) and 1M datapoints that were selectively sampled from a database of 100M (right).

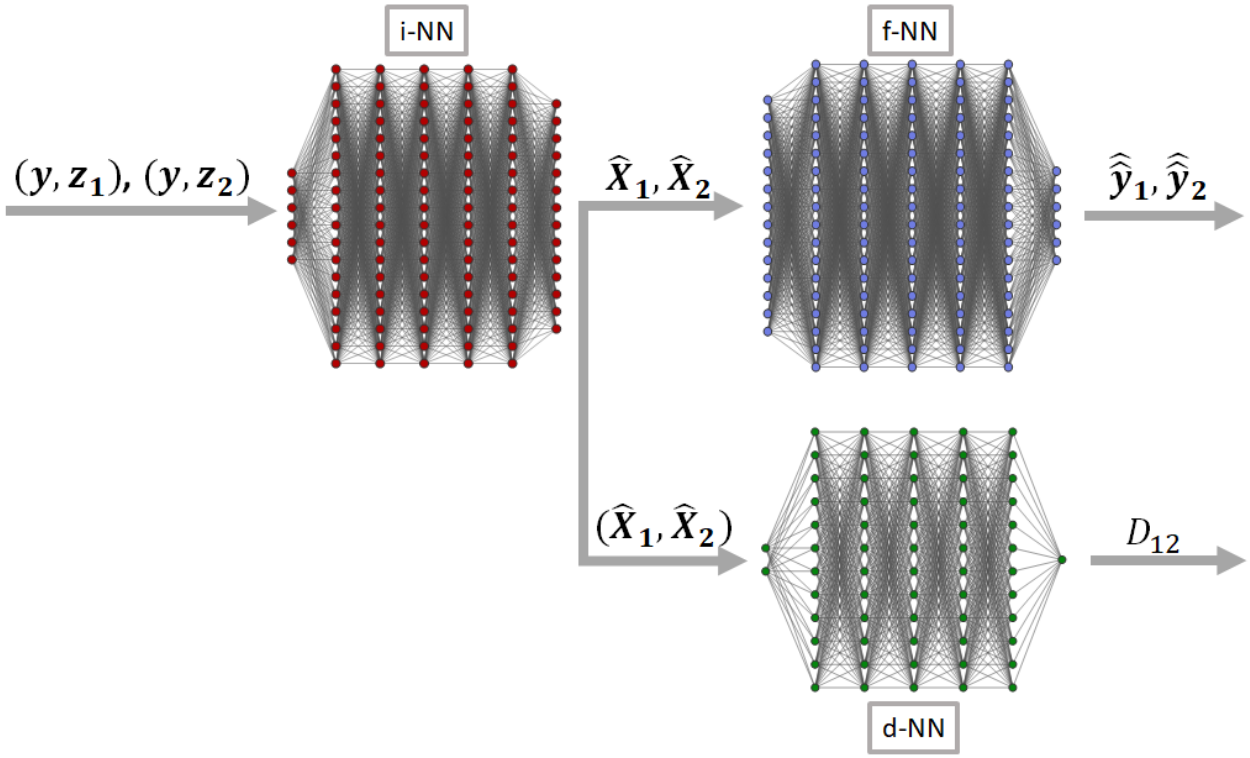

Figure 8.6: A schematic overview of the training process of the i-NN using two passes with trained f-NN and d-NN. During the first pass, the queried stiffnes ($\boldsymbol{y}$) is paired with a randomly sampled parameter ($\boldsymbol{z_1}$) and provided to the i-NN, which produces a set of design parameters ($\hat{\boldsymbol{X}}_\mathbf{1}$). During the second pass, the same $\boldsymbol{y}$ is paired with another random parameter ($\boldsymbol{z_2}$) to produce $\hat{\boldsymbol{X}}_\mathbf{2}$. $\hat{\boldsymbol{X}}_\mathbf{1}$ and $\hat{\boldsymbol{X}}_\mathbf{2}$ are sequentially passed to the forward model to predict the stiffness properties of each design ($\hat{\hat{\boldsymbol{y}}}_\mathbf{1}$ and $\hat{\hat{\boldsymbol{y}}}_\mathbf{2}$). Additionally, $\hat{\boldsymbol{X}}_\mathbf{1}$ and $\hat{\boldsymbol{X}}_\mathbf{2}$ are passed to the d-NN together to predict their difference (D_{12}).

passage will explain the implementation using a two step procedure as example. Please note that the actual training used three passes, this will be discussed in section 8.2.4.

The loss function used to update the network for the example in figure 8.6 includes the stiffness errors of both designs, and the FFT difference between them,

$$\frac{1}{N}\sum_{i=1}^{N}\left(|\boldsymbol{y}_i - \hat{\hat{\boldsymbol{y}}}_{\mathbf{1}i}| + |\boldsymbol{y}_i - \hat{\hat{\boldsymbol{y}}}_{\mathbf{2}i}| + \phi\|\boldsymbol{z}_{\mathbf{1}i} - \boldsymbol{z}_{\mathbf{2}i}\|\,|1 - D_i|\right). \tag{8.2}$$

The first two terms represent the prediction loss of the two structures and the last term is used to promote difference in design. The last layer of the d-NN guarantees that every prediction will take a value between 0 and 1, which represents the normalized difference. Thus, by aiming to minimize $|1 - D|$ (similarity) the network is incentivized to maximize difference. The term $\|\boldsymbol{z}_{\mathbf{1}i} - \boldsymbol{z}_{\mathbf{2}i}\|$ is included to provide a physical interpretation of $\boldsymbol{z}$. By penalizing similarity based on the euclidean distance between $\boldsymbol{z_1}$ and $\boldsymbol{z_2}$, $\boldsymbol{z}$ becomes a measure for relative difference between designs. For example, when a model is trained using a $\boldsymbol{z}$ parameter with a single argument, the two most different designs would be found by querying with $z = 0$ and $z = 1$. Using another value z_r should result in a design with a relative difference to the two extremes that is correlated to the difference between z_r and the two extremes. Lastly, a weight factor, ϕ, is included to set the relative contribution of the similarity penalty to the loss function.

8.2.4 Training and validation

The previous section explained how a two pass network would be trained. As mentioned before, the actual training was done using a three pass process. This means that every stiffness query is passed through the inverse network three times; once with $\boldsymbol{z} = \mathbf{0}$, once with $\boldsymbol{z} = \mathbf{1}$ and once with a random $\boldsymbol{z}$. Thus, every stiffness query will have three design predictions: $\hat{\boldsymbol{X}}_\mathbf{1}$, $\hat{\boldsymbol{X}}_\mathbf{2}$ and $\hat{\boldsymbol{X}}_\mathbf{3}$. Loss function 8.2 is adapted to include the stiffness errors of the three predictions and the three differences D_{12}, D_{13} and D_{23}. This way the network sees the two extremes of $\boldsymbol{z}$ for every query. This should help the network to understand the relative design difference associated with different values of $\boldsymbol{z}$. If only random values are chosen, the network might struggle to interpret the meaning of $\boldsymbol{z}$ and could decide

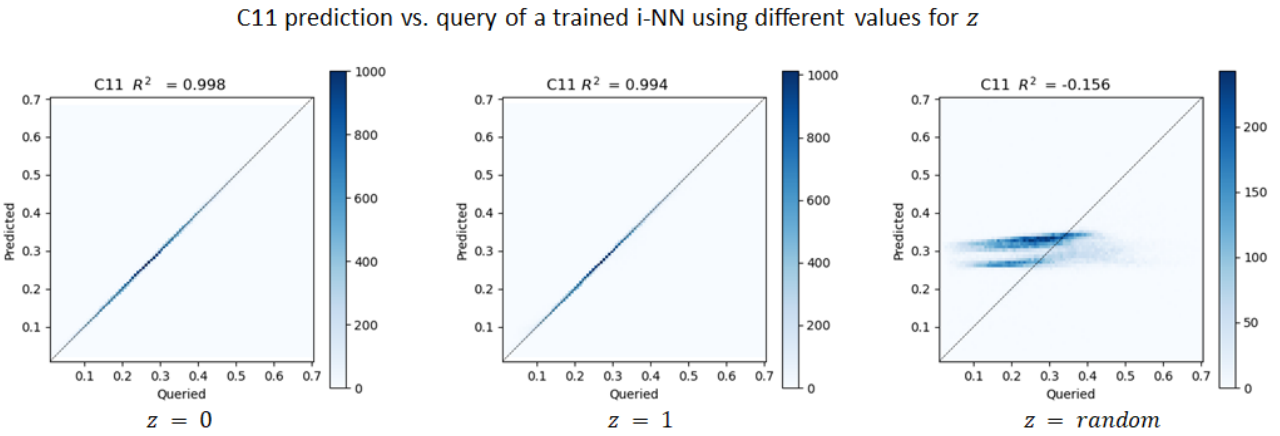

Figure 8.7: C_{11} predictions vs. query of a trained i-NN, with $\phi = 1$, for different values of z: 0, 1 and random. The predictions for $z = 0$ and $z = 1$ are very accurate while a random z leads to very poor predictions. This is representative of the behaviour for the other stiffness components. Changing the value of ϕ has minimal impact on these results.

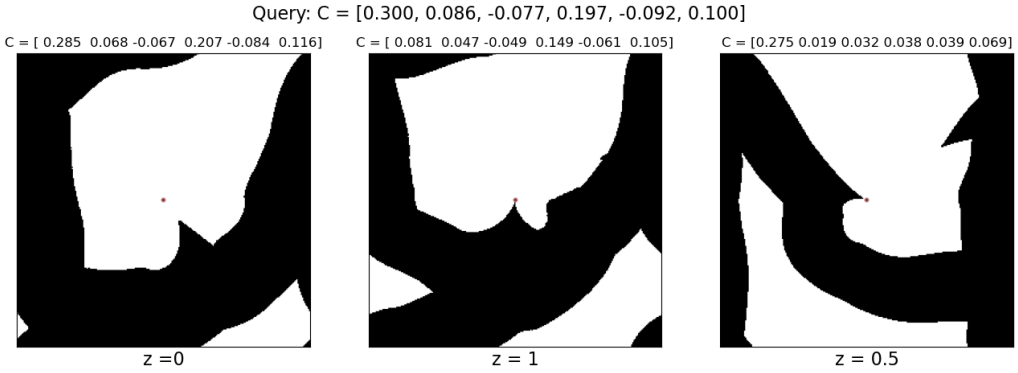

Figure 8.8: Three predictions of the trained i-NN for the same stiffness query, using different values for z. Above each figure the homogenized stiffness components of the predicted structure are plotted.

to ignore it instead. In case of a higher dimensional z, this method can be expanded to include other boundary extremes. Various models are trained, each with a different weight factor, ϕ, ranging from 0.1 to 20. Validation of the models is done using the validation set. The validation set is passed through the network three times; with $z = 0$, $z = 1$ and a random z. The predicted stiffness components for each of the passes are calculated separately and compared to the queried values. Figure 8.7 shows the results for one of the stiffness components for a model trained with $\phi = 0.5$, these results are representative of all stiffness components. The queries with $z = 0$ and $z = 1$ are accurate with R^2 values close to 1, while a random z leads to inaccurate results with negative R^2 values.

To get more insight in these predictions, a stiffness query is done with three different z values: 0, 1 and 0.5. The predicted design parameters are subsequently used to grow and homogenize the three structures, figure 8.8. Despite there being a difference in design between the three structures, the queried stiffness is only close to reproduced by the query with $z = 0$. None of the models that were trained was able to generate multiple designs, while also accurately reconstructing the queried stiffness with each design. Depending on the value of ϕ, models will either produce accurate stiffness properties but with similar unit cells, or they predict different unit cells but with inaccurate stiffness properties.

9 FE simulations and tensile testing

To test the properties of growth based microstructures samples were 3D printed and subjected to a uniaxial tensile test. The results were compared to Finite Element (FE) simulations. To make an interesting test case, a samples with a large negative Poisson's ratio is selected to study the auxetic properties, figure 9.1.

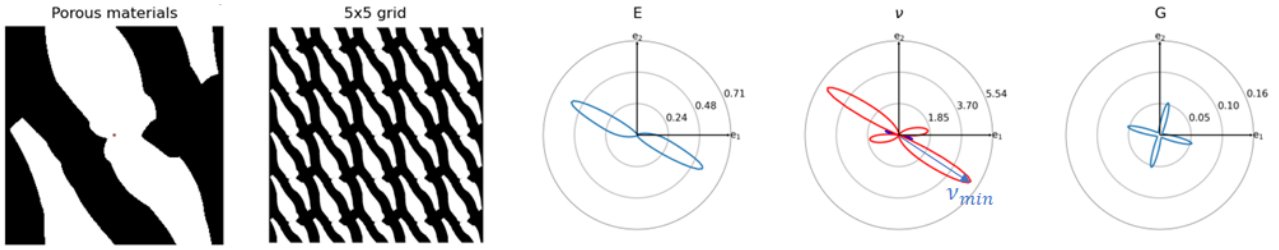

Figure 9.1: The unit cell that was used for 3D printing, with E, ν and G predictions. The red lines in the Poisson's ratio plot indicate a negative value. The direction of most negative ν is indicated by a blue arrow.

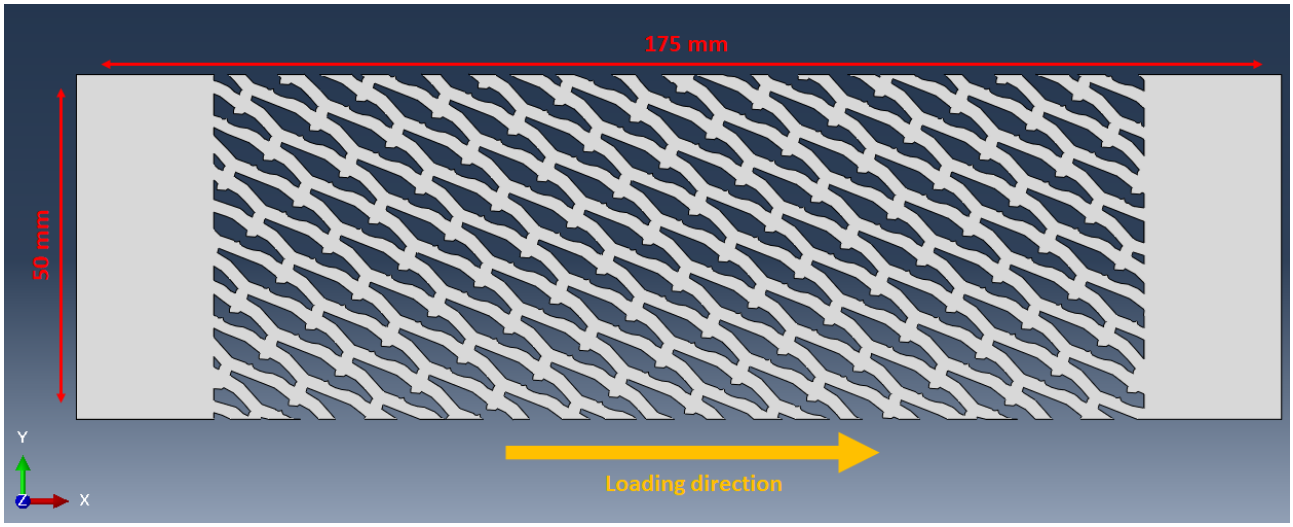

Figure 9.2: A tesselation of the unit cell from figure 9.1 rotated to align ν_{min} with the loading direction. The solid parts on the left and right side of the sample are use to clamp the material during tensile testing.

9.1 Methodology

Since the elastic properties are directional, the unit cell is orientated to align ν_{min} with the loading direction, indicated by a blue arrow in 9.1. Samples are created on an Ultimaker 2+ using a Thermoplastic Polyurethane (TPU) filament. To avoid loss of detail due to printing resolution, unit cells of 8×8 mm were used. Several unit cells are tesselated to produce a sample of 175×50 mm, with a thickness of 3 mm, figure 9.2. The tests are performed on a tensile test bench, using the solid areas on the side to clamp the material. The samples are pre-loaded and a displacement in X direction is prescribed. The reaction forces are measured and a camera is used to record the deformation.

FE simulations are done using Abaqus/CAE 2022 on the same geometry that is used for printing. The 3D model is meshed with standard hex elements, using a linear elastic material model with $E = 67$ MPa and $\nu = 0.3$, which are the values provided by the manufacturer. The load step is configured to take into account non-linear behaviour. To replicate the conditions of the tensile test, XYZ displacements are constrained on the left side, while on the right side YZ are constrained. A displacement in X direction is prescribed, similar to the tensile test, figure 9.2. The reaction forces on the loading edge are recorded and compared to the results of the tensile test. Finally, simulations are done using the same boundary conditions and displacement, but without restraining movement in Y direction on the loading edge.

9.2 Results

The sample is subjected to a maximum displacement of 26 mm during tensile testing. The FE simulations are done with a maximum displacement of 11 mm, to guarantee convergence. The initial and final state of the tensile test are shown in figure 9.3. An overlay of the FE simulation results, and of the sample at the same applied displacement, is also plotted. The deformations of the real sample and simulation show excellent agreement. In the final deformed state of the sample, large deformations near the edges can be observed. These edge effects which make comparing the results to the homogenized properties not straightforward. The FFT homogenization procedure assumes periodic boundary conditions, which implies infinite unit cells in every direction. Due to the size of the sample, the observed behaviour is largely dominated by edge effects. This is confirmed by the computed stress field of the FE results,

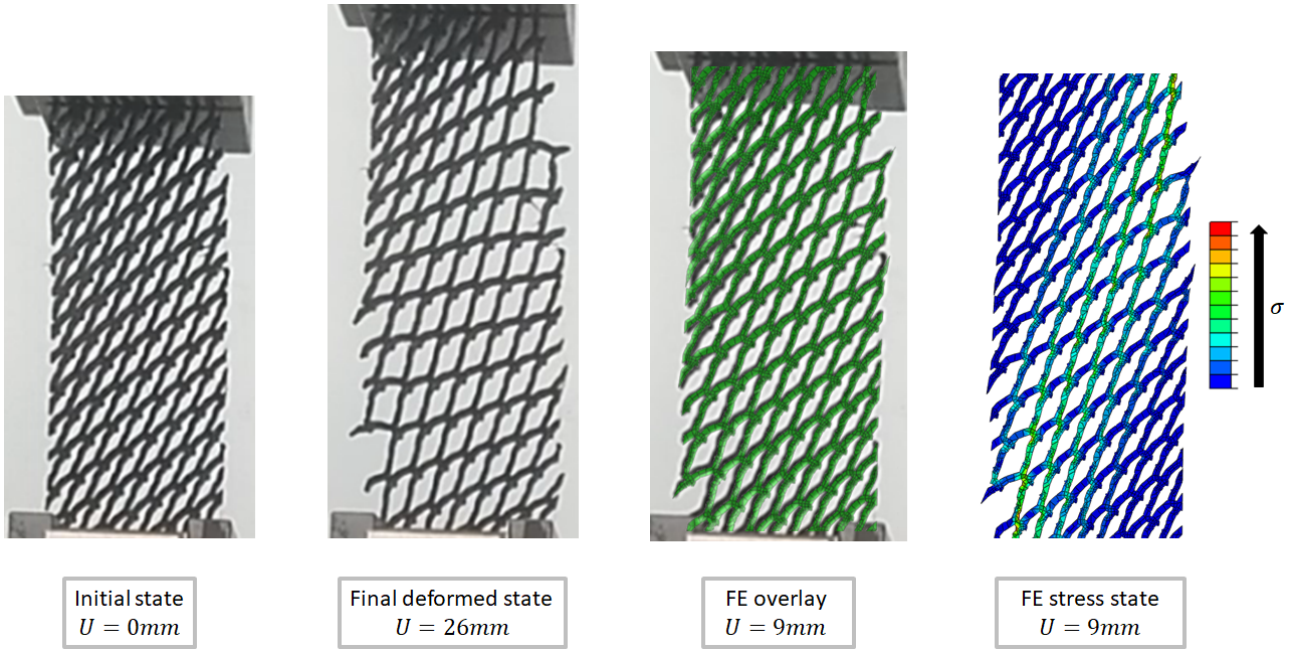

Figure 9.3: Results of the tensile test and FE simulations at different applied displacements U. From left to right: the initial state of the pre-loaded sample, the state of the sample at maximum load, overlay of FE and sample at maximum FE load and FE stress state at maximum FE load. Please note that 11 mm displacement in the FE calculations corresponds to a 9 mm displacement of the printed sample due to pre-loading strain.

figure 9.3. It shows that the stresses are concentrated in the features that connect the two sides. This invalidates the basic assumptions made with periodic boundary conditions, which means these results cannot directly be compared to FFT homogenization. However, the unit cells in the middle of the sample are the best approximation to the homogenized results, and these do exhibit auxetic behaviour.

The force-displacement curves of the two experiments can give insight in the influence of the fabrication process on final properties, figure 9.4. Both curves show a similar trend but the tensile test results reveal a weaker material than predicted by the FE simulation. This can partially be explained by a possible difference in real and modelled TPU properties. The material properties that are used in the FE simulation are averages provided by the manufacturer. However, the actual properties vary from batch to batch and depend on printing conditions. Additionally, 3D printing is an additive process which can introduce voids and imperfect bonds in the sample. This will weaken the final product and result in lower than expected stiffness of the sample.

Lastly, simulations are done where the loading edge is free to move in the Y direction, figure 9.5. The stiffness matrix of the sample has a non-zero component C_{13}, which implies a shear-normal coupling. The C_{13} component

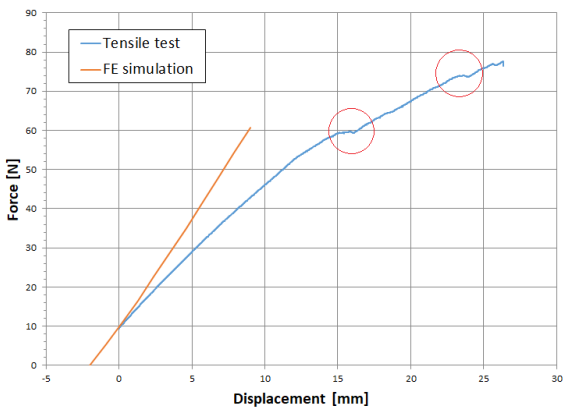

Figure 9.4: Force-displacement curves of the tensile test and FE simulations under similar conditions. The FE results have been shifted to start at a negative displacement to account for the pre-loading of the tensile test. The jumps in the curve in the red circles are caused by the sample slipping during the test.

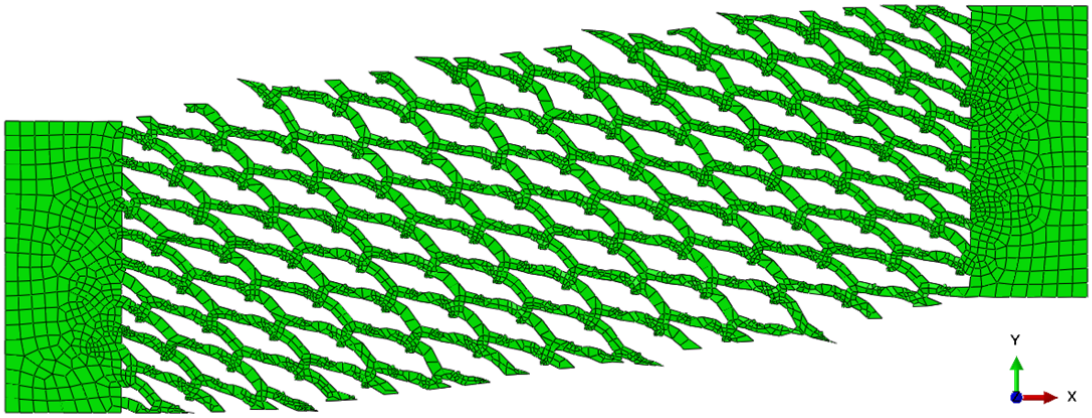

Figure 9.5: Deformed structure of FE tensile simulation without restraining movement in Y direction on the loading edge.

characterizes the interaction between normal displacement and shear reaction force. Thus, applying displacement in the X direction (in FE coordinates) results in a shear force which leads to a displacement of the loading edge in the Y direction.

10 Discussion

The Voronoi diagram growth based method opens up a large design space using simple parameterization. This has allowed us to build accurate forward and inverse models that can produce unit cell that meet target properties. However, producing stochastic outputs has proven challenging and requires more consideration. The problem in the current approach maybe that a single seed location is used to grow a unit cell. As a result, the basic structure of the microstructure will always be formed by a single, arbitrarily shaped, void surrounded by material. It is likely that this makes the possible topologies that can produce a queried stiffness close to unique. This would partially explain the correlation between densities of predicted and queried unit cells. The density correlation could be a result of similarity between the topologies of queries and predictions. Depending on how much we penalize similarity between multiple predictions, the i-NN will either ignore similarity to make predictions that accurately reproduce the queried stiffness, but the unit cells will be similar. Or, if similarity is weighed heavily, the i-NN will predict different unit cells, but stiffness will not match the query. To overcome this issue, it would be interesting to investigate the use of multiple seed locations when growing unit cells, where each of the seeds is assigned different design parameters. Structures will then not be a tesselation of a single void shape, instead it will be formed by multiple voids. This would allow struts to form and may lead to non-unique topology to stiffness relations. Research could first be done on unit cells with multiple seed locations at fixed positions, and could later be extended to allow variable seed locations. The seed locations and growth parameters could all be used as inputs of a neural network, in similar fashion as was done in this thesis.

An alternative method to predict multiple designs could be to focus on elastic properties instead of the whole stiffness matrix. For many applications, stiffness requirements are dictated by one loading direction. Thus, it is not necessary to reproduce an exact stiffness matrix, instead only the maximum Young's modulus of unit cell should match a target value. Using the available data from this research, the maximum and minimum values of E, ν and G can be calculated for each datapoint. A f-NN can be trained to predict one, or more, of these values from design parameters, and an i-NN can be trained to make the inverse predictions. By penalizing similarity, it is likely that an i-NN can be trained that produces different designs for single property targets, i.e. E_{max}. Additionally, this method would let us explore the exotic property space associated with large negative Poisson's ratios. A network trained to inverse design unit cells from ν_{min} queries could be used to produce auxetic structures.

A related research topic would be to study the application of growth based methods for the purpose of origami/kirigami structures. Of particular interest would be out of plane and shear properties. The anisotropic behaviour of most unit cells leads to interesting possibilities for folding and unfolding, using relatively simple actuation methods. For example, under conditions of shear-normal coupling the material would naturally shear under a normal load. This can be done in plane, but can also be exploited when a flat specimen is rolled into a cylinder, which would lead to an extending cylinder in direction of the rolling axis. Other interesting properties could be in the form of out of plane behaviour, where loads can lead to curved surfaces. In theory, a combination of different unit cells could lead to tuneable and specific local curvatures under simple loads. Ultimately, such structures could be of interest for aerospace applications. Payloads could be launched in a space efficient manner and transformed after deployment

using simple actuators. This can reduce complexity of the system, reducing both payload mass and risk of failure.

Another topic of future research would be the extension to 3D. In principle, the growth based method works in 3D space too where it should be able to generate connected structures using simple parameterization. A bottleneck for this research would be generating sufficient data. Producing 1M 2D samples took several days using multiple cores. Both growing and homogenizing of 3D microstructures would be computationally more expensive meaning data generation will take significantly longer. However, 3D models could be applied to real world test cases, such as bone implants. This would serve as an interesting proof of concept to demonstrate the potential of growth based structures. Real world applications will also require to consider fabrication limitations in their design. The necessary conditions are well defined, see Chapter 1.3.2, but may not be straightforward to implement in a NN based approach. It maybe possible to enforce theses conditions by using a postprocessing step on all samples that removes incompatible geometric features before homogenizing them. Alternatively, research could be done on fabrication methods with less stringent requirements, reducing the limits placed on possible designs.

Lastly, more research can be done on fabricating and testing predicted designs. Much of our work has been based on numerical methods and results. This implies that predicted properties and expected behaviour are based on the assumption of perfect conditions. However, in reality the fabrication process will impose limits on feature sizes, and material imperfections will impact performance. Research could be done on the impact of artefacts introduced by fabrication on the final properties to understand the extend of their impact. Additionally, investigating limitations imposed by the chosen method of fabrication could allow to formulate, and enforce, general design rules to limit their impact. This knowledge could also be used to develop or improve fabrication methods for this specific purpose. Additionally, homogenized properties assume periodic boundaries, which implies an infinite number of unit cells in every direction. As demonstrated by the tensile test and FEM simulation, this may not be a realistic real-world scenario, and behaviour might be dominated by boundary effects. Fabricated samples and FE simulations could both be used to analyse these effects in more detail.

References

[1] S. Babaee, J. Shim, J. C. Weaver, E. R. Chen, N. Patel, and K. Bertoldi, "3D Soft Metamaterials with Negative Poisson's Ratio," *Advanced Materials*, vol. 25, pp. 5044–5049, Sept. 2013.

[2] E. Garner, H. M. Kolken, C. C. Wang, A. A. Zadpoor, and J. Wu, "Compatibility in microstructural optimization for additive manufacturing," *Additive Manufacturing*, vol. 26, pp. 65–75, Mar. 2019.

[3] Y. Mao, Q. He, and X. Zhao, "Designing complex architectured materials with generative adversarial networks," *Science Advances*, vol. 6, p. eaaz4169, Apr. 2020.

[4] S. A. Tretyakov, "A personal view on the origins and developments of the metamaterial concept," *Journal of Optics*, vol. 19, p. 013002, Jan. 2017.

[5] E. Shamonina and L. Solymar, "Metamaterials: How the subject started," *Metamaterials*, vol. 1, pp. 12–18, Mar. 2007.

[6] S. K. Jha, "A study of significance of metamaterials on physics and engineering," vol. 6, no. 7, p. 10, 2015.

[7] A. Sengar, "Meta-materials and comparison between antenna parameters of normal micro-strip antenna and meta-material micro-strip antenna," vol. 3, no. 4, p. 4, 2017.

[8] V. G. Veselago, "The electrodynamics of substances with simultaneously negative values of permittivity and permeability," *Soviet Physics Uspekhi*, vol. 10, pp. 509–514, Apr. 1968. Publisher: Uspekhi Fizicheskikh Nauk (UFN) Journal.

[9] F. Ding, A. Pors, and S. I. Bozhevolnyi, "Gradient metasurfaces: a review of fundamentals and applications," *Reports on Progress in Physics*, vol. 81, p. 026401, Feb. 2018.

[10] D. R. Smith, D. C. Vier, N. Kroll, and S. Schultz, "Direct calculation of permeability and permittivity for a left-handed metamaterial," *Applied Physics Letters*, vol. 77, pp. 2246–2248, Oct. 2000.

[11] C. M. Soukoulis and M. Wegener, "Past achievements and future challenges in the development of three-dimensional photonic metamaterials," *Nature Photonics*, vol. 5, pp. 523–530, Sept. 2011.

[12] S. A. Cummer, J. Christensen, and A. Alù, "Controlling sound with acoustic metamaterials," *Nature Reviews Materials*, vol. 1, p. 16001, Mar. 2016.

[13] F. Bosia, A. O. Krushynska, M. Miniaci, B. Morvan, and N. M. Pugno, "Editorial: Advances in Mechanical Metamaterials," *Frontiers in Materials*, vol. 5, p. 56, Sept. 2018.

[14] A. Alù, "Prime time," *Nature Materials*, vol. 15, pp. 1229–1231, Dec. 2016.

[15] M. Kadic, T. Bückmann, R. Schittny, and M. Wegener, "Metamaterials beyond electromagnetism," *Reports on Progress in Physics*, vol. 76, p. 126501, Dec. 2013.

[16] T. A. Schaedler, A. J. Jacobsen, A. Torrents, A. E. Sorensen, J. Lian, J. R. Greer, L. Valdevit, and W. B. Carter, "Ultralight Metallic Microlattices," *Science*, vol. 334, pp. 962–965, Nov. 2011.

[17] D. P. Hampshire, "A derivation of Maxwell's equations using the Heaviside notation," *Philosophical Transactions of the Royal Society A: Mathematical, Physical and Engineering Sciences*, vol. 376, p. 20170447, Dec. 2018.

[18] S. A. Ramakrishna, "Physics of negative refractive index materials," *Reports on Progress in Physics*, vol. 68, pp. 449–521, Feb. 2005.

[19] "https://polymerdatabase.com/polymer%20physics/Refractive%20Index.html, accessed Dec. 2021."

[20] "Chegg.com, accesssed Dec. 2021."

[21] A. E. Musa, K. M. Haroun, M. D. A. Allah, and I. A. I. Hammad, "The Relation Between Incident And Medium Electromagnetic Field And Left Handed Materials," *American Journal of Engineering Research*, p. 10, 2018.

[22] A. Vian, E. Davies, M. Gendraud, and P. Bonnet, "Plant Responses to High Frequency Electromagnetic Fields," *BioMed Research International*, vol. 2016, pp. 1–13, 2016.

[23] J. Pendry, A. Holden, D. Robbins, and W. Stewart, "Magnetism from conductors and enhanced nonlinear phenomena," *IEEE Transactions on Microwave Theory and Techniques*, vol. 47, pp. 2075–2084, Nov. 1999.

[24] D. R. Smith, W. J. Padilla, D. C. Vier, S. C. Nemat-Nasser, and S. Schultz, "Composite Medium with Simultaneously Negative Permeability and Permittivity," *Physical Review Letters*, vol. 84, pp. 4184–4187, May 2000.

[25] N. I. Landy, S. Sajuyigbe, J. J. Mock, D. R. Smith, and W. J. Padilla, "Perfect Metamaterial Absorber," *Physical Review Letters*, vol. 100, p. 207402, May 2008.

[26] Q. Huang, G. Wang, M. Zhou, J. Zheng, S. Tang, and G. Ji, "Metamaterial electromagnetic wave absorbers and devices: Design and 3D microarchitecture," *Journal of Materials Science & Technology*, vol. 108, pp. 90–101, May 2022.

[27] C. Cen, Z. Yi, G. Zhang, Y. Zhang, C. Liang, X. Chen, Y. Tang, X. Ye, Y. Yi, J. Wang, and J. Hua, "Theoretical design of a triple-band perfect metamaterial absorber in the THz frequency range," *Results in Physics*, vol. 14, p. 102463, Sept. 2019.

[28] F. Ding, Y. Cui, X. Ge, Y. Jin, and S. He, "Ultra-broadband microwave metamaterial absorber," *Applied Physics Letters*, vol. 100, p. 103506, Mar. 2012.

[29] H. Tao, C. M. Bingham, A. C. Strikwerda, D. Pilon, D. Shrekenhamer, N. I. Landy, K. Fan, X. Zhang, W. J. Padilla, and R. D. Averitt, "Highly flexible wide angle of incidence terahertz metamaterial absorber: Design, fabrication, and characterization," *Physical Review B*, vol. 78, p. 241103, Dec. 2008.

[30] A. A. Zadpoor, "Mechanical meta-materials," *Materials Horizons*, vol. 3, no. 5, pp. 371–381, 2016.

[31] K. Bertoldi, V. Vitelli, J. Christensen, and M. van Hecke, "Flexible mechanical metamaterials," *Nature Reviews Materials*, vol. 2, p. 17066, Nov. 2017.

[32] T. Liu, Z.-M. Li, S. Jin, and W. Chen, "Compliant assembly analysis including initial deviations and geometric nonlinearity—Part I: Beam structure," *Proceedings of the Institution of Mechanical Engineers, Part C: Journal of Mechanical Engineering Science*, vol. 233, pp. 4233–4246, June 2019.

[33] G. W. Milton and A. V. Cherkaev, "Which Elasticity Tensors are Realizable?," *Journal of Engineering Materials and Technology*, vol. 117, pp. 483–493, Oct. 1995.

[34] W. Voigt, "Ueber die Beziehung zwischen den beiden Elasticitätsconstanten isotroper Körper," *Annalen der Physik*, vol. 274, no. 12, pp. 573–587, 1889.

[35] B. Liu, X. Feng, and S.-M. Zhang, "The effective Young's modulus of composites beyond the Voigt estimation due to the Poisson effect," *Composites Science and Technology*, vol. 69, pp. 2198–2204, Oct. 2009.

[36] A. Reuss, "Berechnung der Fließgrenze von Mischkristallen auf Grund der Plastizitätsbedingung für Einkristalle .," *ZAMM - Zeitschrift für Angewandte Mathematik und Mechanik*, vol. 9, no. 1, pp. 49–58, 1929.

[37] R. Hill, "The Elastic Behaviour of a Crystalline Aggregate," *Proceedings of the Physical Society. Section A*, vol. 65, pp. 349–354, May 1952.

[38] W. J. Parnell and C. Calvo-Jurado, "On the computation of the Hashin–Shtrikman bounds for transversely isotropic two-phase linear elastic fibre-reinforced composites," *Journal of Engineering Mathematics*, vol. 95, pp. 295–323, Dec. 2015.

[39] C. C. Swan and I. Kosaka, "Voigt-Reuss topology optimization for structures with linear elastic material behaviours," *International Journal for Numerical Methods in Engineering*, vol. 40, pp. 3033–3057, Aug. 1997.

[40] M. P. Bendsøe and O. Sigmund, "Material interpolation schemes in topology optimization," *Archive of Applied Mechanics (Ingenieur Archiv)*, vol. 69, pp. 635–654, Nov. 1999.

[41] Z. Hashin and S. Shtrikman, "A variational approach to the theory of the elastic behaviour of multiphase materials," *Journal of the Mechanics and Physics of Solids*, vol. 11, pp. 127–140, Mar. 1963.

[42] S. Pellegrino and C. Calladine, "Matrix analysis of statically and kinematically indeterminate frameworks," *International Journal of Solids and Structures*, vol. 22, no. 4, pp. 409–428, 1986.

[43] V. Deshpande, M. Ashby, and N. Fleck, "Foam topology: bending versus stretching dominated architectures," *Acta Materialia*, vol. 49, pp. 1035–1040, Apr. 2001.

[44] R. Schwaiger, L. Meza, and X. Li, "The extreme mechanics of micro- and nanoarchitected materials," *MRS Bulletin*, vol. 44, pp. 758–765, Oct. 2019.

[45] L. R. Meza, A. J. Zelhofer, N. Clarke, A. J. Mateos, D. M. Kochmann, and J. R. Greer, "Resilient 3D hierarchical architected metamaterials," *Proceedings of the National Academy of Sciences*, vol. 112, pp. 11502–11507, Sept. 2015.

[46] T. Tancogne-Dejean and D. Mohr, "Elastically-isotropic truss lattice materials of reduced plastic anisotropy," *International Journal of Solids and Structures*, vol. 138, pp. 24–39, May 2018.

[47] N. A. Fleck, V. S. Deshpande, and M. F. Ashby, "Micro-architectured materials: past, present and future," *Proceedings of the Royal Society A: Mathematical, Physical and Engineering Sciences*, vol. 466, pp. 2495–2516, Sept. 2010.

[48] C. Calladine, "Buckminster Fuller's "Tensegrity" structures and Clerk Maxwell's rules for the construction of stiff frames," *International Journal of Solids and Structures*, vol. 14, no. 2, pp. 161–172, 1978.

[49] L. R. Meza, G. P. Phlipot, C. M. Portela, A. Maggi, L. C. Montemayor, A. Comella, D. M. Kochmann, and J. R. Greer, "Reexamining the mechanical property space of three-dimensional lattice architectures," *Acta Materialia*, vol. 140, pp. 424–432, Nov. 2017.

[50] K. E. Evans, "Auxetic polymers: a new range of materials," *Endeavour*, vol. 15, pp. 170–174, Jan. 1991.

[51] T.-C. Lim, *Auxetic Materials and Structures*. Engineering Materials, Singapore: Springer Singapore, 2015.

[52] S. Poisson, "Note sur l'extension des fils et des plaques élastiques.," *Annales de Chimie et de Physique*, vol. 36, pp. 384–387, 1827.

[53] S. Ji, L. Li, H. B. Motra, F. Wuttke, S. Sun, K. Michibayashi, and M. H. Salisbury, "Poisson's Ratio and Auxetic Properties of Natural Rocks: Poisson's Ratio and Auxetic Properties of Natural Rocks," *Journal of Geophysical Research: Solid Earth*, vol. 123, pp. 1161–1185, Feb. 2018.

[54] P. Karasudhi and P. Karasudhi, *Foundations of Solid Mechanics*. Dordrecht, Netherlands, the: Springer Netherlands, 1990.

[55] J. Pérez, B. Thomaszewski, S. Coros, B. Bickel, J. A. Canabal, R. Sumner, and M. A. Otaduy, "Design and fabrication of flexible rod meshes," *ACM Transactions on Graphics*, vol. 34, pp. 1–12, July 2015.

[56] H. D. Wagner and S. Weiner, "On the relationship between microstructure of bone and its mechanical stiffness," p. 10.

[57] W. M. Han, S.-J. Heo, T. P. Driscoll, J. F. Delucca, C. M. McLeod, L. Smith, R. L. Duncan, R. L. Mauck, and D. M. Elliott, "Microstructural heterogeneity directs micromechanics and mechanobiology in native and engineered fibrocartilage," *Nature Materials*, vol. 15, pp. 477–484, Apr. 2016.

[58] G. D. O'Connell, H. L. Guerin, and D. M. Elliott, "Theoretical and Uniaxial Experimental Evaluation of Human Annulus Fibrosus Degeneration," *Journal of Biomechanical Engineering*, vol. 131, p. 111007, Nov. 2009.

[59] B. Zhu, M. Skouras, D. Chen, and W. Matusik, "Two-Scale Topology Optimization with Microstructures," *ACM Transactions on Graphics*, vol. 34, no. 4, p. 17.

[60] C. Schumacher, B. Bickel, J. Rys, S. Marschner, C. Daraio, and M. Gross, "Microstructures to control elasticity in 3D printing," *ACM Transactions on Graphics*, vol. 34, pp. 1–13, July 2015.

[61] B. Bickel, M. Bacher, M. A. Otaduy, W. Matusik, H. P[U+FB01]ster, and M. Gross, "Capture and Modeling of Non-Linear Heterogeneous Soft Tissue," p. 9.

[62] G. Kiziltas, J. Volakis, and N. Kikuchi, "Metamaterial design via the density method," in *IEEE Antennas and Propagation Society International Symposium (IEEE Cat. No.02CH37313)*, vol. 1, (San Antonio, TX, USA), pp. 748–751, IEEE, 2002.

[63] T. I. Zohdi and P. Wriggers, *An introduction to computational micromechanics*. Lecture Notes in Applied and Computational Mechanics, Berlin: Springer, 2008.

[64] S. Zhou and Q. Li, "Design of graded two-phase microstructures for tailored elasticity gradients," *Journal of Materials Science*, vol. 43, pp. 5157–5167, Aug. 2008.

[65] S. Kumar, S. Tan, L. Zheng, and D. M. Kochmann, "Inverse-designed spinodoid metamaterials," *npj Computational Materials*, vol. 6, p. 73, Dec. 2020.

[66] Z. Du, X.-Y. Zhou, R. Picelli, and H. A. Kim, "Connecting Microstructures for Multiscale Topology Optimization With Connectivity Index Constraints," *Journal of Mechanical Design*, vol. 140, p. 111417, Nov. 2018.

[67] A. Ion, J. Frohnhofen, L. Wall, R. Kovacs, M. Alistar, J. Lindsay, P. Lopes, H.-T. Chen, and P. Baudisch, "Metamaterial Mechanisms," in *Proceedings of the 29th Annual Symposium on User Interface Software and Technology*, (Tokyo Japan), pp. 529–539, ACM, Oct. 2016.

[68] B. Bickel, M. Bächer, M. A. Otaduy, H. R. Lee, H. Pfister, M. Gross, and W. Matusik, "Design and fabrication of materials with desired deformation behavior," *ACM Transactions on Graphics*, vol. 29, pp. 1–10, July 2010.

[69] C. C. Seepersad, R. S. Kumar, J. K. Allen, F. Mistree, and D. L. Mcdowell, "Multifunctional design of prismatic cellular materials," *Journal of Computer-Aided Materials Design*, vol. 11, pp. 163–181, Jan. 2004.

[70] H. Li, Z. Luo, L. Gao, and P. Walker, "Topology optimization for functionally graded cellular composites with metamaterials by level sets," *Computer Methods in Applied Mechanics and Engineering*, vol. 328, pp. 340–364, Jan. 2018.

[71] Y. Wang, F. Chen, and M. Y. Wang, "Concurrent design with connectable graded microstructures," *Computer Methods in Applied Mechanics and Engineering*, vol. 317, pp. 84–101, Apr. 2017.

[72] M. Niino and S. Maeda, "Recent development status of functionally gradient materials.," *ISIJ International*, vol. 30, no. 9, pp. 699–703, 1990.

[73] A. Radman, X. Huang, and Y. M. Xie, "Topology optimization of functionally graded cellular materials," *Journal of Materials Science*, vol. 48, pp. 1503–1510, Feb. 2013.

[74] A. D. Cramer, V. J. Challis, and A. P. Roberts, "Microstructure interpolation for macroscopic design," *Structural and Multidisciplinary Optimization*, vol. 53, pp. 489–500, Mar. 2016.

[75] R. Lakes, "Materials with structural hierarchy," *Nature*, vol. 361, pp. 511–515, Feb. 1993.

[76] R. S. Farr, "Fractal design for an efficient shell strut under gentle compressive loading," *Physical Review E*, vol. 76, p. 056608, Nov. 2007.

[77] R. S. Farr, "Fractal design for efficient brittle plates under gentle pressure loading," *Physical Review E*, vol. 76, p. 046601, Oct. 2007.

[78] R. S. Farr and Y. Mao, "Fractal space frames and metamaterials for high mechanical efficiency," *EPL (Europhysics Letters)*, vol. 84, p. 14001, Oct. 2008.

[79] D. Rayneau-Kirkhope, R. S. Farr, and Y. Mao, "Fractal-like dependence in the designs of efficient pressure-bearing structures," *EPL (Europhysics Letters)*, vol. 93, p. 34002, Feb. 2011.

[80] L. R. Meza, S. Das, and J. R. Greer, "Strong, lightweight, and recoverable three-dimensional ceramic nanolattices," *Science*, vol. 345, pp. 1322–1326, Sept. 2014.

[81] L. Newton, "The power of origami," p. 11.

[82] J. J. Park, P. Won, and S. H. Ko, "A Review on Hierarchical Origami and Kirigami Structure for Engineering Applications," *International Journal of Precision Engineering and Manufacturing-Green Technology*, vol. 6, pp. 147–161, Jan. 2019.

[83] Z. Zhai, L. Wu, and H. Jiang, "Mechanical metamaterials based on origami and kirigami," *Applied Physics Reviews*, vol. 8, p. 041319, Dec. 2021.

[84] J. L. Silverberg, A. A. Evans, L. McLeod, R. C. Hayward, T. Hull, C. D. Santangelo, and I. Cohen, "Using origami design principles to fold reprogrammable mechanical metamaterials," *Science*, vol. 345, pp. 647–650, Aug. 2014.

[85] C. D. Santangelo, "Theory and practice of origami in science," *Soft Matter*, vol. 16, no. 1, pp. 94–101, 2020.

[86] E. D. Demaine, J. S. Ku, and M. Yoder, "Folding Triangular and Hexagonal Mazes," p. 6.

[87] K. Miura, “Proposition of Pseudo-Cylindrical Concave Polyhedral Shells,” Nov. 1969.

[88] M. Schenk and S. D. Guest, “Geometry of Miura-folded metamaterials,” *Proceedings of the National Academy of Sciences*, vol. 110, pp. 3276–3281, Feb. 2013.

[89] B. Zhang, J. Hendrickson, N. Nader, H.-T. Chen, and J. Guo, “Metasurface optical antireflection coating,” *Applied Physics Letters*, vol. 105, p. 241113, Dec. 2014.

[90] R. J. Lang, *Origami 4*. CRC Press, Aug. 2009. Google-Books-ID: kOPqBgAAQBAJ.

[91] G. P. T. Choi, L. H. Dudte, and L. Mahadevan, “Compact reconfigurable kirigami,” *Physical Review Research*, vol. 3, p. 043030, Oct. 2021.

[92] Y.-C. Cheng, H.-C. Lu, X. Lee, H. Zeng, and A. Priimagi, “Kirigami-Based Light-Induced Shape-Morphing and Locomotion,” *Advanced Materials*, vol. 32, no. 7, p. 1906233, 2020. _eprint: https://onlinelibrary.wiley.com/doi/pdf/10.1002/adma.201906233.

[93] X. Guo, X. Ni, J. Li, H. Zhang, F. Zhang, H. Yu, J. Wu, Y. Bai, H. Lei, Y. Huang, J. A. Rogers, and Y. Zhang, “Designing Mechanical Metamaterials with Kirigami-Inspired, Hierarchical Constructions for Giant Positive and Negative Thermal Expansion,” *Advanced Materials*, vol. 33, no. 3, p. 2004919, 2021. _eprint: https://onlinelibrary.wiley.com/doi/pdf/10.1002/adma.202004919.

[94] Z. Chen, Y. Li, and Q. Li, “Hydrogel-driven origami metamaterials for tunable swelling behavior,” *Materials & Design*, vol. 207, p. 109819, Sept. 2021.

[95] N. Z. Nkomo, “A Review of 4D Printing Technology and Future Trends,” p. 11, 2018.

[96] J. T. B. Overvelde, S. Shan, and K. Bertoldi, “Compaction Through Buckling in 2D Periodic, Soft and Porous Structures: Effect of Pore Shape,” *Advanced Materials*, vol. 24, pp. 2337–2342, May 2012.

[97] Y. Forterre, J. M. Skotheim, J. Dumais, and L. Mahadevan, “How the Venus flytrap snaps,” *Nature*, vol. 433, pp. 421–425, Jan. 2005.

[98] O. Al-Ketan and R. K. Abu Al-Rub, “Multifunctional Mechanical Metamaterials Based on Triply Periodic Minimal Surface Lattices,” *Advanced Engineering Materials*, vol. 21, p. 1900524, Oct. 2019.

[99] T. Mullin, S. Deschanel, K. Bertoldi, and M. C. Boyce, “Pattern Transformation Triggered by Deformation,” *Physical Review Letters*, vol. 99, p. 084301, Aug. 2007.

[100] L. J. Gibson and M. F. Ashby, *Cellular solids : structure and properties*. Cambridge solid state science series, Cambridge ;: Cambridge University Press, 2nd ed. ed., 1997. Section: xviii, 510 pages : illustrations ; 26 cm.

[101] K. Bertoldi, M. Boyce, S. Deschanel, S. Prange, and T. Mullin, “Mechanics of deformation-triggered pattern transformations and superelastic behavior in periodic elastomeric structures,” *Journal of the Mechanics and Physics of Solids*, vol. 56, pp. 2642–2668, Aug. 2008.

[102] R. Lakes, “Foam Structures with a Negative Poisson’s Ratio,” *Science*, vol. 235, pp. 1038–1040, Feb. 1987.

[103] C. Smith, J. Grima, and K. Evans, “A novel mechanism for generating auxetic behaviour in reticulated foams: missing rib foam model,” *Acta Materialia*, vol. 48, pp. 4349–4356, Nov. 2000.

[104] K. K. Saxena, R. Das, and E. P. Calius, “Three Decades of Auxetics Research – Materials with Negative Poisson’s Ratio,” *Advanced Engineering Materials*, vol. 18, pp. 1847–1870, Nov. 2016.

[105] S. C. Han, D. S. Kang, and K. Kang, “Two nature-mimicking auxetic materials with potential for high energy absorption,” *Materials Today*, vol. 26, pp. 30–39, June 2019.

[106] C. Coulais, C. Kettenis, and M. van Hecke, “A characteristic length scale causes anomalous size effects and boundary programmability in mechanical metamaterials,” *Nature Physics*, vol. 14, pp. 40–44, Jan. 2018.

[107] G. Chirima, N. Ravirala, A. Rawal, V. R. Simkins, A. Alderson, and K. L. Alderson, “The effect of processing parameters on the fabrication of auxetic extruded polypropylene films,” *physica status solidi (b)*, vol. 245, pp. 2383–2390, Nov. 2008.

[108] A. P. Pickles, R. S. Webber, K. L. Alderson, P. J. Neale, and K. E. Evans, “The effect of the processing parameters on the fabrication of auxetic polyethylene: Part I The effect of compaction conditions,” *Journal of Materials Science*, vol. 30, pp. 4059–4068, Aug. 1995.

[109] K. L. Alderson, A. P. Kettle, P. J. Neale, A. P. Pickles, and K. E. Evans, "The effect of the processing parameters on the fabrication of auxetic polyethylene: Part II The effect of sintering temperature and time," *Journal of Materials Science*, vol. 30, pp. 4069–4075, Aug. 1995.

[110] P. J. Neale, A. P. Pickles, K. L. Alderson, and K. E. Evans, "The effect of the processing parameters on the fabrication of auxetic polyethylene: Part III The effect of extrusion conditions," *Journal of Materials Science*, vol. 30, pp. 4087–4094, Aug. 1995.

[111] N. Chan and K. E. Evans, "Fabrication methods for auxetic foams," p. 9.

[112] R. Lakes, "Advances in negative Poisson's ratio materials," *Advanced Materials*, vol. 5, pp. 293–296, Apr. 1993.

[113] A. Joseph, V. Mahesh, and D. Harursampath, "On the application of additive manufacturing methods for auxetic structures: a review," *Advances in Manufacturing*, vol. 9, pp. 342–368, Sept. 2021.

[114] K. Bertoldi, P. M. Reis, S. Willshaw, and T. Mullin, "Negative Poisson's Ratio Behavior Induced by an Elastic Instability," *Advanced Materials*, vol. 22, pp. 361–366, Jan. 2010.

[115] L. Mizzi, E. Mahdi, K. Titov, R. Gatt, D. Attard, K. E. Evans, J. N. Grima, and J.-C. Tan, "Mechanical metamaterials with star-shaped pores exhibiting negative and zero Poisson's ratio," *Materials & Design*, vol. 146, pp. 28–37, May 2018.

[116] X. Ren, R. Das, P. Tran, T. D. Ngo, and Y. M. Xie, "Auxetic metamaterials and structures: a review," *Smart Materials and Structures*, vol. 27, p. 023001, Feb. 2018.

[117] P. J. Gandy, S. Bardhan, A. L. Mackay, and J. Klinowski, "Nodal surface approximations to the P,G,D and I-WP triply periodic minimal surfaces," *Chemical Physics Letters*, vol. 336, pp. 187–195, Mar. 2001.

[118] X. Zheng, X. Guo, and I. Watanabe, "A mathematically defined 3D auxetic metamaterial with tunable mechanical and conduction properties," *Materials & Design*, vol. 198, p. 109313, Jan. 2021.

[119] K. Grosse-Brauckmann, "Triply periodic minimal and constant mean curvature surfaces," *Interface Focus*, vol. 2, pp. 582–588, Oct. 2012.

[120] Y. Jung and S. Torquato, "Fluid permeabilities of triply periodic minimal surfaces," *Physical Review E*, vol. 72, p. 056319, Nov. 2005.

[121] K. Tapp, *Differential Geometry of Curves and Surfaces*. Undergraduate Texts in Mathematics, Cham: Springer International Publishing, 2016.

[122] M. Beeson, "Notes on Minimal Surfaces," Sept. 2007.

[123] H. Schwarz, *Gesammelte mathematische Abhandlungen von H.A. Schwarz Bd. 1, 2.* Berlin: Springer, 1890. Section: 2 dln in 1 band.

[124] A. H. Schoen, "Infinite periodice minimal surfaces without self-intersections," May 1970.

[125] E. A. Lord and A. L. Mackay, "Periodic minimal surfaces of cubic symmetry," *CURRENT SCIENCE*, vol. 85, no. 3, p. 19, 2003.

[126] D. Cvijović and J. Klinowski, "The computation of the triply periodic I-WP minimal surface," *Chemical Physics Letters*, vol. 226, pp. 93–99, Aug. 1994.

[127] O. Al-Ketan, R. Rowshan, and R. K. Abu Al-Rub, "Topology-mechanical property relationship of 3D printed strut, skeletal, and sheet based periodic metallic cellular materials," *Additive Manufacturing*, vol. 19, pp. 167–183, Jan. 2018.

[128] S. Rajagopalan and R. A. Robb, "Schwarz Meets Schwann: Design and Fabrication of Biomorphic Tissue Engineering Scaffolds," in *Medical Image Computing and Computer-Assisted Intervention – MICCAI 2005* (D. Hutchison, T. Kanade, J. Kittler, J. M. Kleinberg, F. Mattern, J. C. Mitchell, M. Naor, O. Nierstrasz, C. Pandu Rangan, B. Steffen, M. Sudan, D. Terzopoulos, D. Tygar, M. Y. Vardi, G. Weikum, J. S. Duncan, and G. Gerig, eds.), vol. 3749, pp. 794–801, Berlin, Heidelberg: Springer Berlin Heidelberg, 2005. Series Title: Lecture Notes in Computer Science.

[129] S. C. Kapfer, S. T. Hyde, K. Mecke, C. H. Arns, and G. E. Schröder-Turk, “Minimal surface scaffold designs for tissue engineering,” *Biomaterials*, vol. 32, pp. 6875–6882, Oct. 2011.

[130] S. C. Han, J. M. Choi, G. Liu, and K. Kang, “A Microscopic Shell Structure with Schwarz’s D-Surface,” *Scientific Reports*, vol. 7, p. 13405, Dec. 2017.

[131] J. W. Hutchinson and J. M. T. Thompson, “Imperfections and energy barriers in shell buckling,” *International Journal of Solids and Structures*, vol. 148-149, pp. 157–168, Sept. 2018.

[132] C. Wang, Z. Vangelatos, C. P. Grigoropoulos, and Z. Ma, “Micro-engineered architected metamaterials for cell and tissue engineering,” *Materials Today Advances*, vol. 13, p. 100206, Mar. 2022.

[133] L. Zheng, S. Kumar, and D. M. Kochmann, “Data-driven topology optimization of spinodoid metamaterials with seamlessly tunable anisotropy,” *Computer Methods in Applied Mechanics and Engineering*, vol. 383, p. 113894, Sept. 2021.

[134] M.-T. Hsieh, B. Endo, Y. Zhang, J. Bauer, and L. Valdevit, “The mechanical response of cellular materials with spinodal topologies,” *Journal of the Mechanics and Physics of Solids*, vol. 125, pp. 401–419, Apr. 2019.

[135] D. A. Porter and K. E. Easterling, *Phase transformations in metals and alloys*. Boca Raton, Fla.: CRC Press, 3., rev. ed. ed., 2008. Section: 616 Seiten : Illustrationen, Diagramme.

[136] J. W. Cahn and J. E. Hilliard, “Free Energy of a Nonuniform System. I. Interfacial Free Energy,” p. 11.

[137] J. W. Cahn, “Phase Separation by Spinodal Decomposition in Isotropic Systems,” *The Journal of Chemical Physics*, vol. 42, pp. 93–99, Jan. 1965.

[138] Institute of Physical Chemistry, NCSR ”Demokritos”, 153 10 Ag.Paraskevi, Attikis,Grecce, E. Favvas, A. C. Mitropoulos, and Department of Petroleum Technology, Kavala Institute of Technology, 65 404 St.Lucas, Kavala, Greece., “What is spinodal decomposition?,” *Journal of Engineering Science and Technology Review*, vol. 1, pp. 25–27, June 2008.

[139] J. W. Cahn, “On spinodal decomposition,” *Acta Metallurgica*, vol. 9, no. 9, pp. 795–801, 1961. 795.

[140] H. Jinnai, T. Koga, Y. Nishikawa, T. Hashimoto, and S. T. Hyde, “Curvature Determination of Spinodal Interface in a Condensed Matter System,” *Physical Review Letters*, vol. 78, pp. 2248–2251, Mar. 1997.

[141] Y. Kwon, K. Thornton, and P. Voorhees, “Morphology and topology in coarsening of domains via non-conserved and conserved dynamics,” *Philosophical Magazine*, vol. 90, pp. 317–335, Jan. 2010.

[142] X.-Y. Sun, G.-K. Xu, X. Li, X.-Q. Feng, and H. Gao, “Mechanical properties and scaling laws of nanoporous gold,” *Journal of Applied Physics*, vol. 113, p. 023505, Jan. 2013.

[143] T. Nagaya and J.-M. Gilli, “Experimental Study of Spinodal Decomposition in a 1D Conserved Order Parameter System,” *Physical Review Letters*, vol. 92, p. 145504, Apr. 2004.

[144] V. Sofonea and K. Mecke, “Morphological characterization of spinodal decomposition kinetics,” *The European Physical Journal B*, vol. 8, pp. 99–112, Mar. 1999.

[145] A. Vidyasagar, S. Krödel, and D. M. Kochmann, “Microstructural patterns with tunable mechanical anisotropy obtained by simulating anisotropic spinodal decomposition,” *Proceedings of the Royal Society A: Mathematical, Physical and Engineering Sciences*, vol. 474, p. 20180535, Oct. 2018.

[146] G. Wulff, “XXY. Zur Frage der Geschwindigkeit des Wachs- thums und der Auflösung der Krystallflächen.,” p. 82.

[147] C. Herring, “Some Theorems on the Free Energies of Crystal Surfaces,” *Physical Review*, vol. 82, pp. 87–93, Apr. 1951.

[148] N. Cabrera, “The equilibrium of crystal surfaces,” *Surface Science*, vol. 2, pp. 320–345, Jan. 1964.

[149] C. M. Portela, A. Vidyasagar, S. Krödel, T. Weissenbach, D. W. Yee, J. R. Greer, and D. M. Kochmann, “Extreme mechanical resilience of self-assembled nanolabyrinthine materials,” *Proceedings of the National Academy of Sciences*, vol. 117, pp. 5686–5693, Mar. 2020.

[150] T. Philippe, H. Henry, and M. Plapp, "Nucleation of crystal surfaces with corner energy regularization," *Journal of Crystal Growth*, vol. 503, pp. 20–27, Dec. 2018.

[151] J. Stewart and N. Goldenfeld, "Spinodal decomposition of a crystal surface," *Physical Review A*, vol. 46, pp. 6505–6512, Nov. 1992.

[152] F. Liu and H. Metiu, "Dynamics of phase separation of crystal surfaces," *Physical Review B*, vol. 48, pp. 5808–5817, Sept. 1993.

[153] S. Torabi, J. Lowengrub, A. Voigt, and S. Wise, "A new phase-field model for strongly anisotropic systems," *Proceedings of the Royal Society A: Mathematical, Physical and Engineering Sciences*, vol. 465, pp. 1337–1359, May 2009.

[154] M. Salvalaglio, R. Backofen, R. Bergamaschini, F. Montalenti, and A. Voigt, "Faceting of Equilibrium and Metastable Nanostructures: A Phase-Field Model of Surface Diffusion Tackling Realistic Shapes," *Crystal Growth & Design*, vol. 15, pp. 2787–2794, June 2015.

[155] C. Soyarslan, S. Bargmann, M. Pradas, and J. Weissmüller, "3D stochastic bicontinuous microstructures: Generation, topology and elasticity," *Acta Materialia*, vol. 149, pp. 326–340, May 2018.

[156] S. Kumar and D. M. Kochmann, "What machine learning can do for computational solid mechanics," *arXiv:2109.08419 [cs]*, Sept. 2021. arXiv: 2109.08419.

[157] J. Martínez, J. Dumas, and S. Lefebvre, "Procedural voronoi foams for additive manufacturing," *ACM Transactions on Graphics*, vol. 35, pp. 1–12, July 2016.

[158] J. Martínez, S. Hornus, H. Song, and S. Lefebvre, "Polyhedral voronoi diagrams for additive manufacturing," *ACM Transactions on Graphics*, vol. 37, pp. 1–15, Aug. 2018.

[159] J. Martínez, M. Skouras, C. Schumacher, S. Hornus, S. Lefebvre, and B. Thomaszewski, "Star-shaped metrics for mechanical metamaterial design," *ACM Transactions on Graphics*, vol. 38, pp. 1–13, Aug. 2019.

[160] C. Icking and L. Ma, "A Tight Bound for the Complexity of Voronoi Diagrams under Polyhedral Convex Distance Functions in 3D," p. 6.

[161] D. Cifuentes, K. Ranestad, B. Sturmfels, and M. Weinstein, "Voronoi cells of varieties," *Journal of Symbolic Computation*, vol. 109, pp. 351–366, Mar. 2022.

[162] C. Schumacher, S. Marschner, M. Gross, and B. Thomaszewski, "Mechanical characterization of structured sheet materials," *ACM Transactions on Graphics*, vol. 37, pp. 1–15, Aug. 2018.

[163] S. Forte and M. Vianello, "Symmetry classes for elasticity tensors," *Journal of Elasticity*, vol. 43, pp. 81–108, May 1996.

[164] F. Aurenhammer, "Voronoi diagrams—a survey of a fundamental geometric data structure," *ACM Computing Surveys*, vol. 23, pp. 345–405, Sept. 1991.

[165] R. Zayer, D. Mlakar, M. Steinberger, and H.-P. Seidel, "Layered Fields for Natural Tessellations on Surfaces," *arXiv:1804.09152 [cs]*, Apr. 2018. arXiv: 1804.09152.

[166] T. Iwtitute, "The anisotropic behavior of Poisson's ratio, Young's modulus, and shear modulus in hexagonal materials," p. 5.

[167] T. Bohlke and C. Bruggemann, "Graphical Representation of the Generalized Hooke's Law," p. 15.

[168] S. Yalameha, Z. Nourbakhsh, and D. Vashaee, "ElTools: A tool for analyzing anisotropic elastic properties of the 2D and 3D materials," *Computer Physics Communications*, vol. 271, p. 108195, Feb. 2022.

[169] S. Brisard, "Janus," 2019.

[170] H. Moulinec and P. Suquet, "A numerical method for computing the overall response of nonlinear composites with complex microstructure," *Computer Methods in Applied Mechanics and Engineering*, vol. 157, pp. 69–94, Apr. 1998.

[171] C. M. Bishop, *Pattern recognition and machine learning*. Information science and statistics, New York: Springer, 2006.

[172] C. F. Jekel, K. E. Swartz, D. A. White, D. A. Tortorelli, and S. E. Watts, “Neural Network Layers for Prediction of Positive Definite Elastic Stiffness Tensors,” *arXiv:2203.13938 [cs]*, Mar. 2022. arXiv: 2203.13938.

[173] N. Srivastava, G. Hinton, A. Krizhevsky, I. Sutskever, and R. Salakhutdinov, “Dropout: A Simple Way to Prevent Neural Networks from overfitting,” p. 30.

[174] M. W. Wong, *Discrete Fourier Analysis*. Basel: Springer Basel, 2011.

A Stiffness component correlations

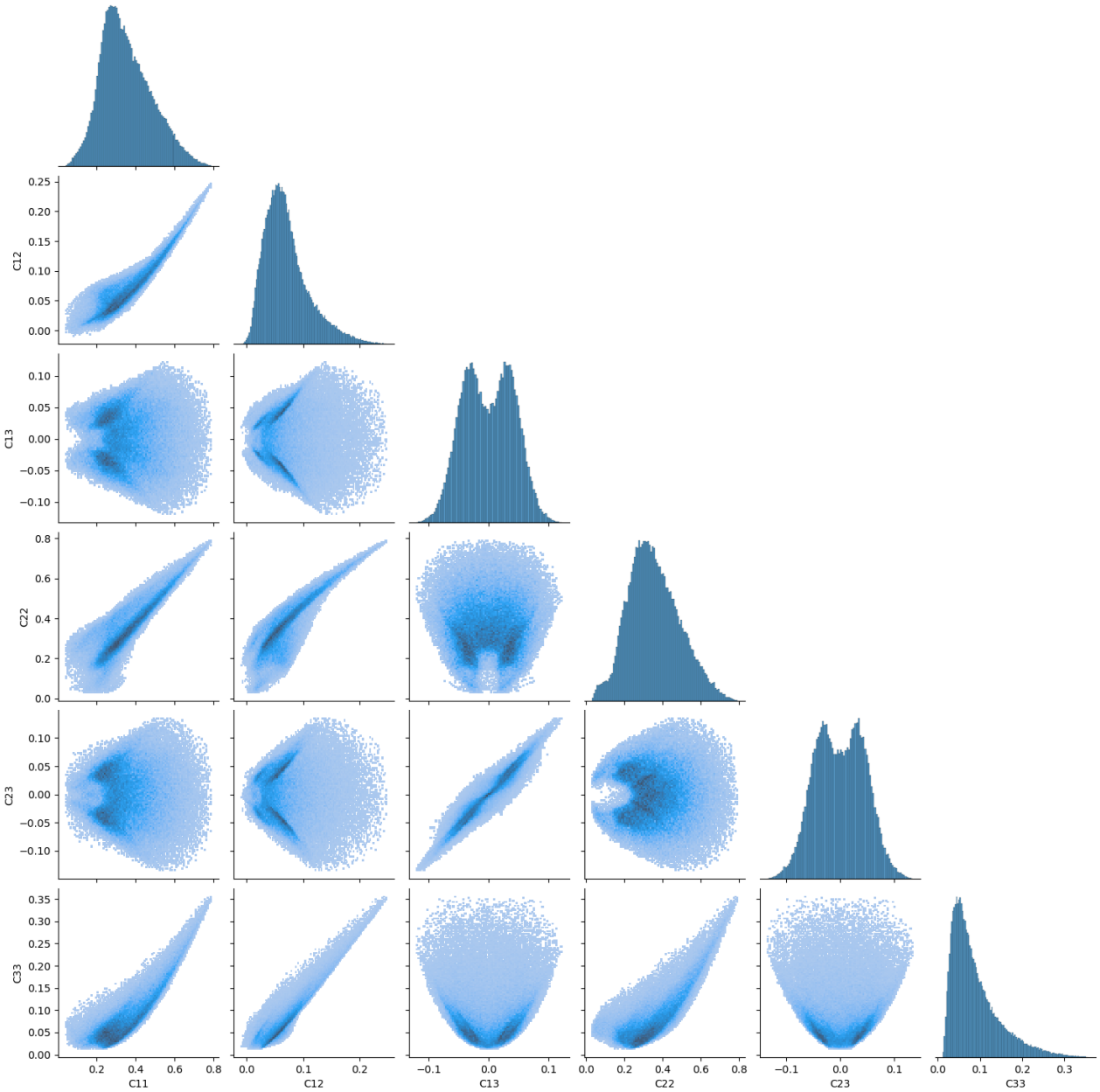

Figure A.1: Stiffness component correlation for 3 spans.

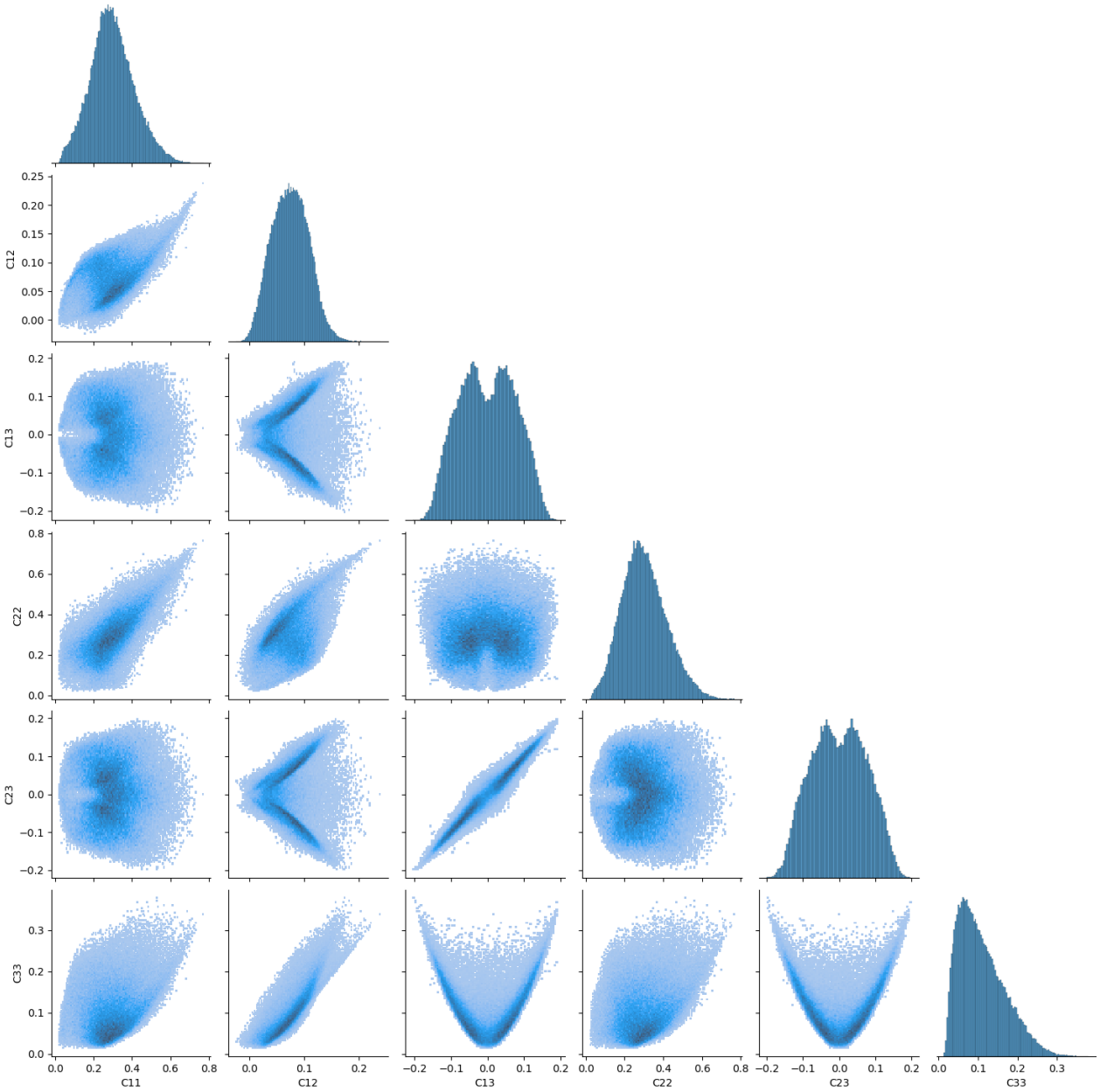

Figure A.2: Stiffness component correlation for 5 spans.

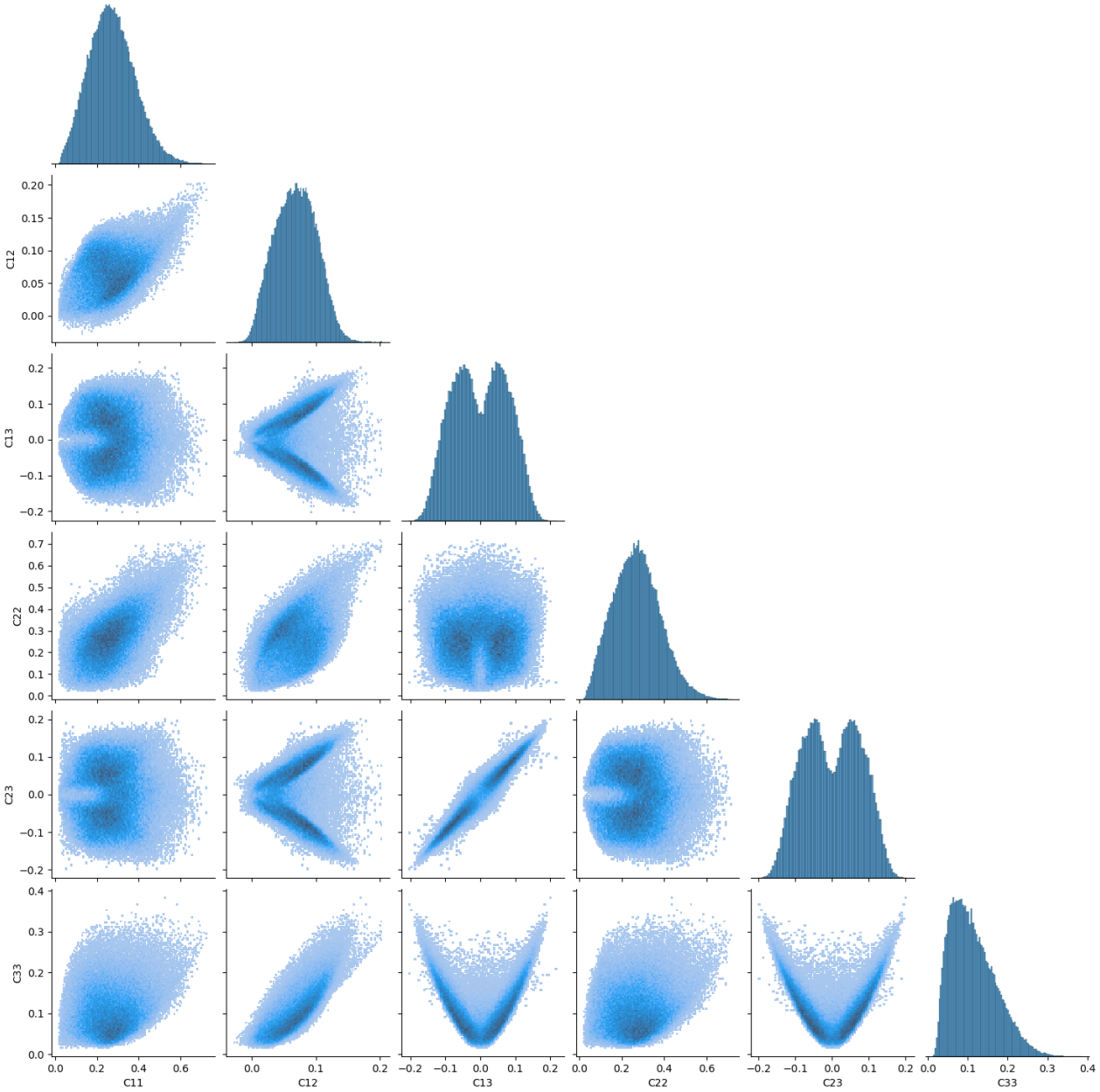

Figure A.3: Stiffness component correlation for 7 spans.

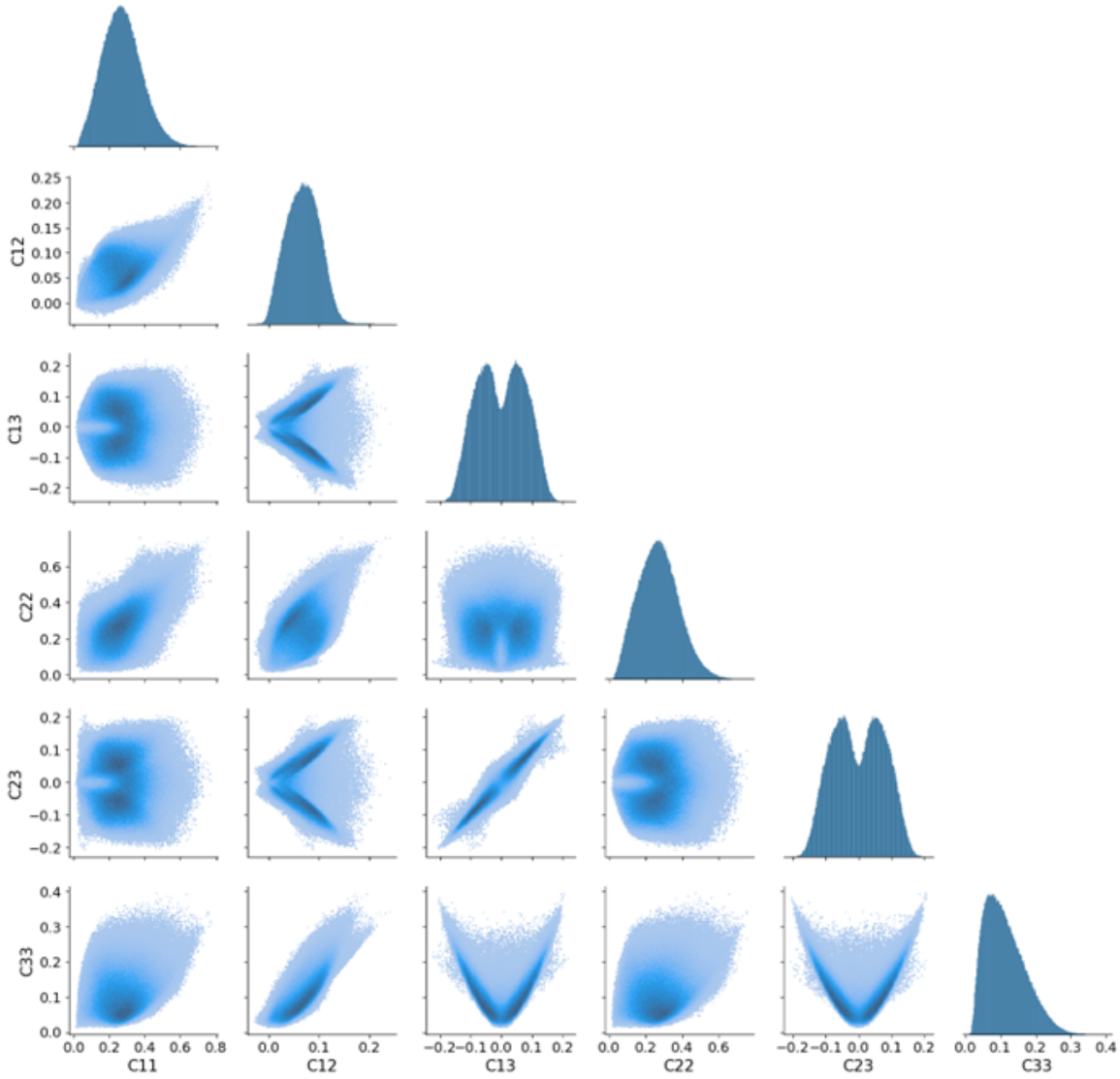

Figure A.4: Stiffness component correlation for 7 spans and 1M samples.

B Validation of f-NN and i-NN

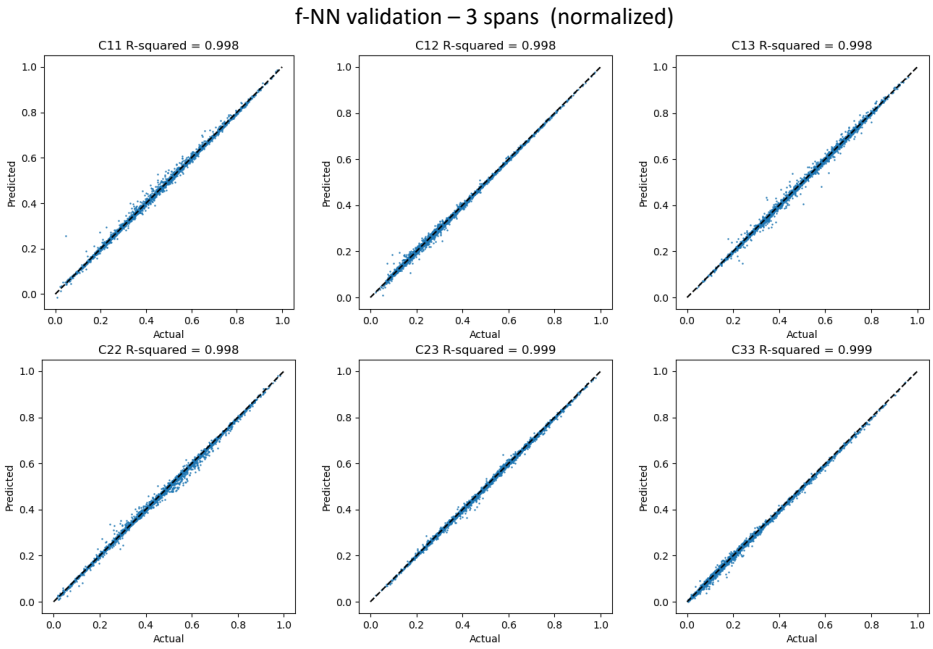

Figure B.1: Prediction errors of f-NN for all stiffness components using 3 spans.

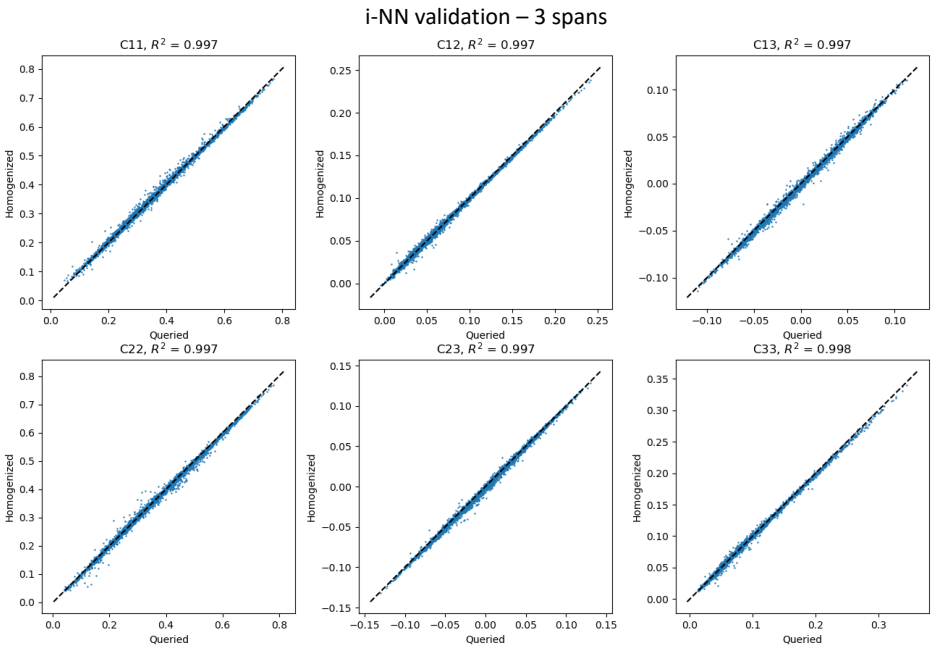

Figure B.2: Prediction errors of i-NN for all stiffness components using 3 spans.

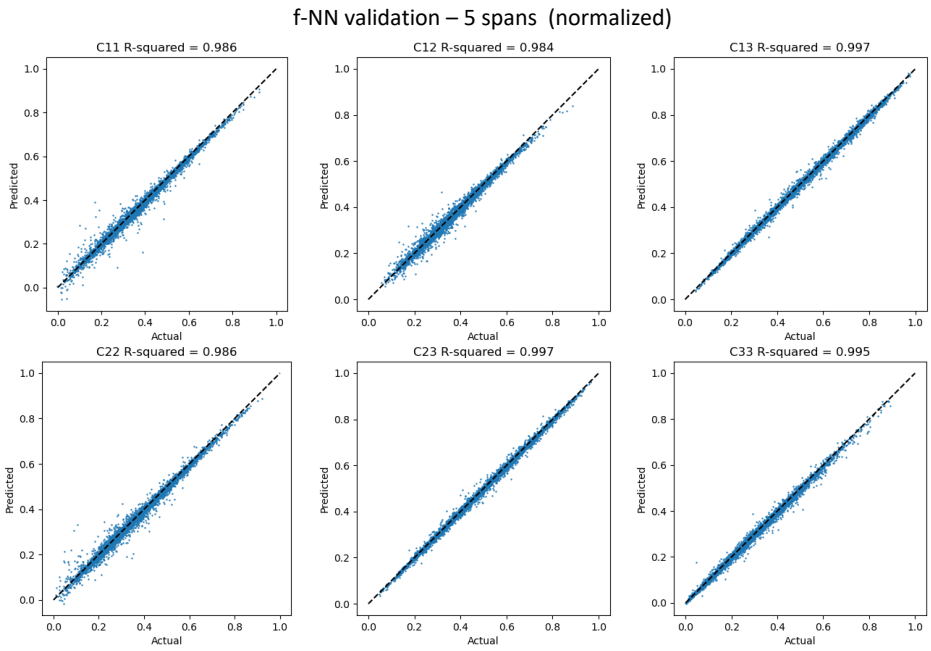

Figure B.3: Prediction errors of f-NN for all stiffness components using 5 spans.

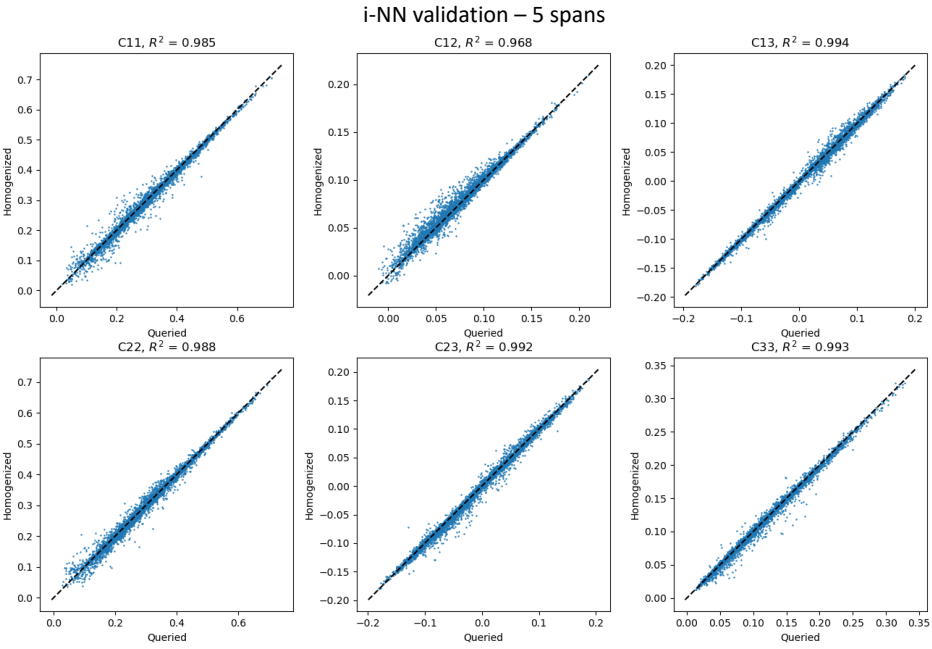

Figure B.4: Prediction errors of i-NN for all stiffness components using 5 spans.

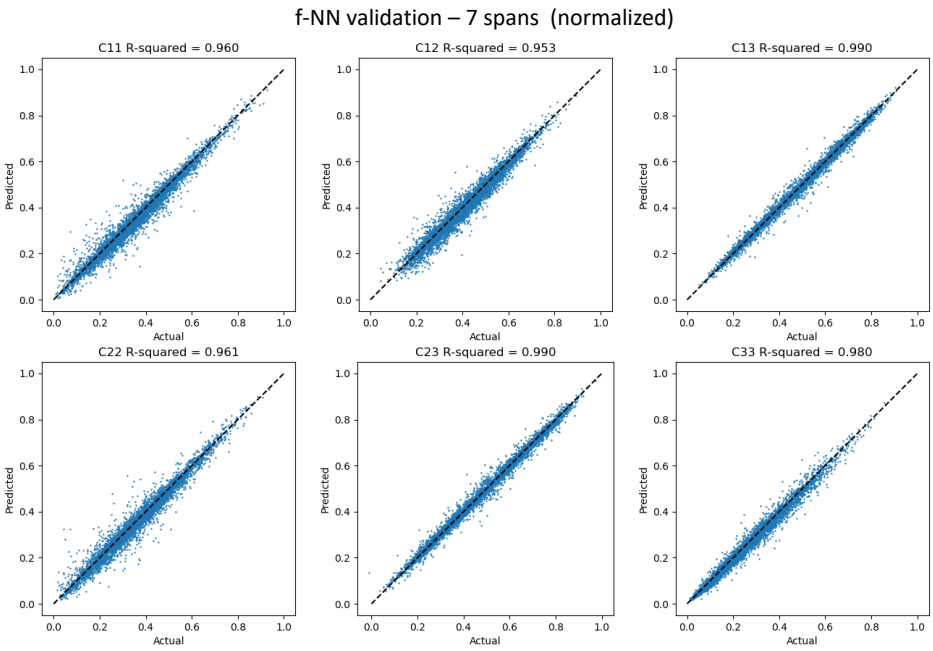

Figure B.5: Prediction errors of f-NN for all stiffness components using 7 spans.

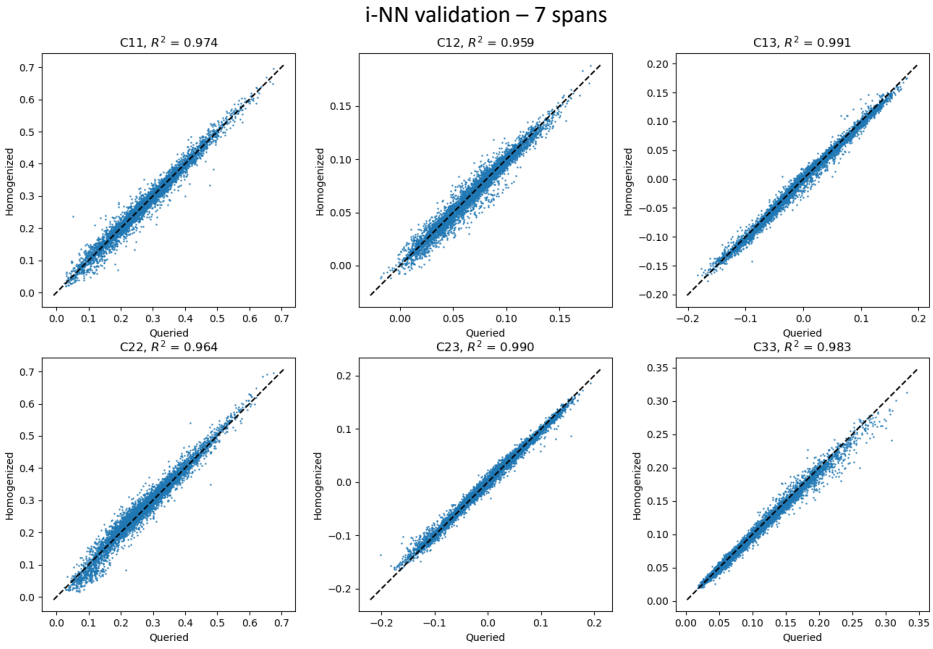

Figure B.6: Prediction errors of i-NN for all stiffness components using 7 spans.

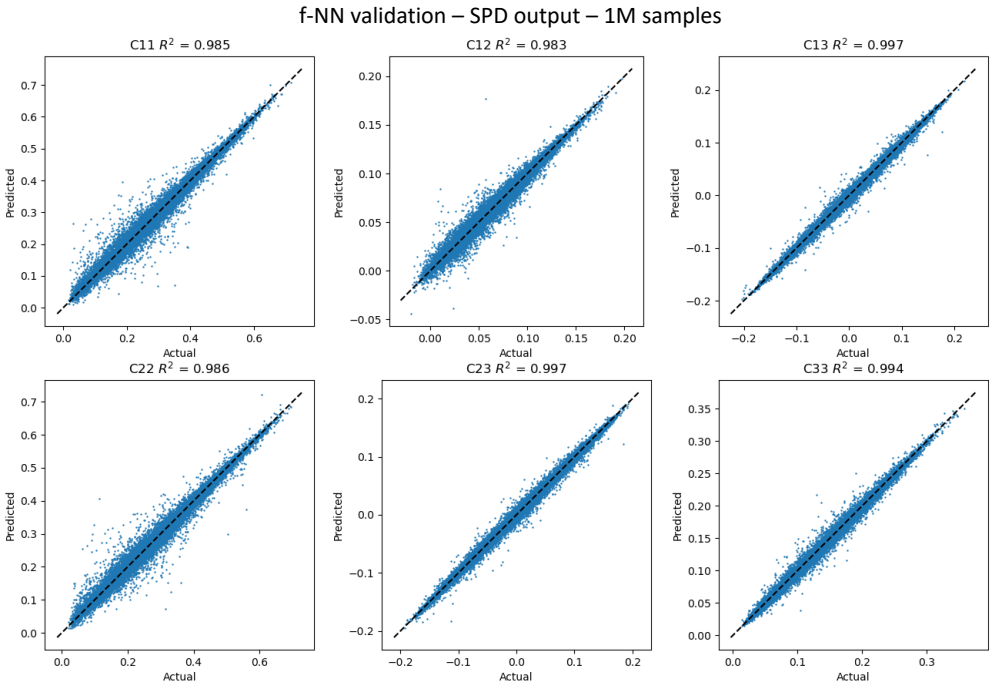

Figure B.7: Prediction error of f-NN for all stiffness components using 1M samples and SPD output.

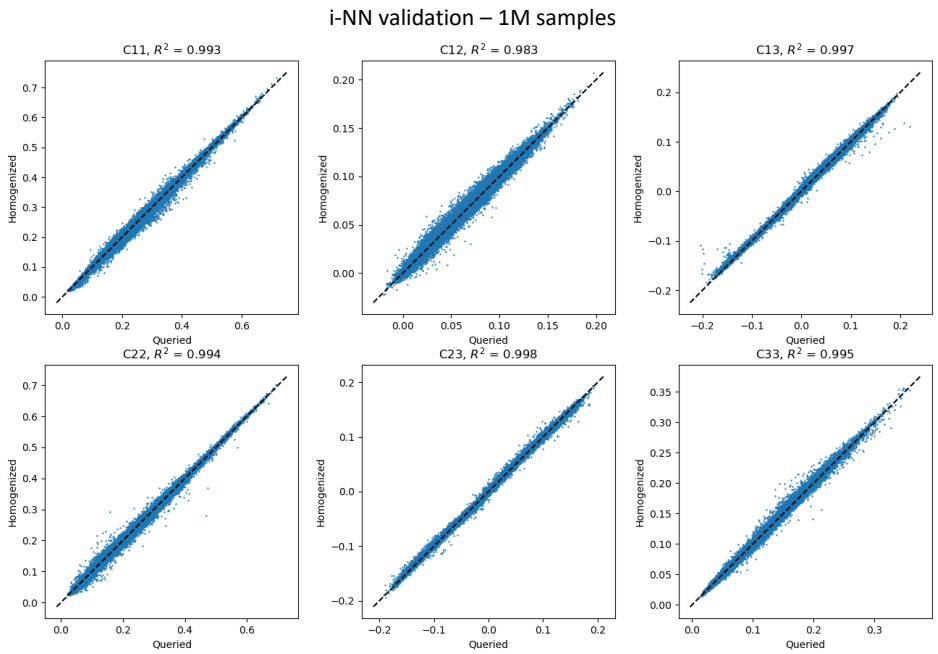

Figure B.8: Prediction error of i-NN for all stiffness components using 1M samples and a f-NN with SPD output.